EXPERIMENTAL CHARACTERIZATION OF UNDERWATER VISIBLE LIGHT COMMUNICATIONS

A Dissertation

by

Samet Yildiz

Submitted to the
Graduate School of Sciences and Engineering
In Partial Fulfillment of the Requirements for
the Degree of

Doctor of Philosophy

in the
Department of Electrical and Electronics Engineering

Özyeğin University
December 2022

EXPERIMENTAL CHARACTERIZATION OF UNDERWATER VISIBLE LIGHT COMMUNICATIONS

Approved by:

Professor Murat Uysal, Advisor
Department of Electrical and Electronics Engineering
Özyeğin University

Assistant Professor Kadir Durak
Department of Electrical and Electronics Engineering
Özyeğin University

Professor Serhan Yarkan
Department of Electrical and Electronics Engineering
Istanbul Ticaret University

Associate Professor Cenk Demiroğlu
Department of Electrical and Electronics Engineering
Özyeğin University

Date Approved: 22 December 2022

Associate Professor Sultan Aldırmaz Çolak
Department of Electrical and Electronics Engineering
Kocaeli University

To my beloved wife...

ABSTRACT

As human activities such as collecting scientific data, monitoring the environment, exploring offshore oilfields, archaeology, harbor security, and surveillance increase, the demand for underwater communication systems has also increased. Wire-line systems underwater can provide real-time communication in numerous ways. Wire-line systems, however, are limited by their inflexibility, high costs, and operational disadvantages to being used underwater in most real-life situations. Thus, underwater wireless communication has attracted an inevitable amount of attention from researchers. Underwater wireless transmission is typically performed using acoustic signaling due to its capability to support distances of up to tens of kilometers. However, due to its low data rate (in tens of Kilobits Per Second (Kb/s)), it is unsuitable for high-bandwidth underwater applications such as image or real-time video transmission. Therefore, optical communication offers a high-capacity alternative to low-capacity acoustic communication.

With the transparency of water to blue and green light (450 nm – 550 nm), Laser Diodes (LDs) or Light Emitting Diodes (LEDs) can potentially serve as underwater wireless transmitters with data rates up to tens of Gigabits Per Second (Gb/s) per wavelength. Any technology must undergo experimental validation and investigation for the theoretical studies to be validated. However, there still needs to be more experimental verification for Underwater Visible Light Communication (UVLC) systems. In addition, path loss, a bottleneck caused by massive attenuation in underwater environments, must be addressed. Therefore, experimental verification is needed for semi-collimated optical signals propagating underwater. Based on the experimentally verified attenuation model, a UVLC with a semi-collimated source is to be investigated to achieve the performance constraints of

UVLC, how further to improve the received optical signal via a reflector, and how to optimize the system performance in the presence of solar noise.

Motivated by these, we target experimentally validating a collimated and semi-collimated UVLC attenuation model. For this reason, we first confirm the accuracy of the collimated measurements after measuring the extinction coefficient of the water experimentally. Then, after generating a semi-collimated Gaussian beam using various optical lenses, we measure the beam divergence angle. Afterward, considering different water types in an indoor aquarium at OKATEM Research center and both collimated and semi-collimated laser sources with Gaussian beam shapes, we perform measurements to determine the UVLC path loss channel coefficient. Finally, we confirm experimentally the theoretically proposed aggregate channel model that incorporates both attenuation and geometric loss.

Having enough confidence in the conventional UVLC semi-collimated channels, which are already verified experimentally, we then investigate the performance constraints of UVLC system in the absence of turbulence and pointing errors. For a targeted Bit Error Rate (BER) performance, we derive closed-form expressions for the maximum achievable link distance, maximum acceptable beam divergence angle, minimum acceptable receiver aperture diameter, and maximum acceptable water turbidity. Using these expressions, we investigate each system parameter's performance in the simulation environment in the pure sea, clear ocean, and coastal water to meet the desired BER performance with the use of desired system performance of a M-ary Unipolar Pulse-Amplitude Modulation (PAM) (M-UPAM) UVLC systems.

After confirming the aggregate path loss channel coefficient for Line of Sight (LOS) links, we observe that the scattered rays would support the channel gain with a reflector by reflecting them to the photodetector. In the literature, the reflector-aided transmission technique is only explored after receiving both direct and scattered rays for higher received signal strength. Therefore, we propose a closed-form expression for the underwater path loss assuming Non-Line-of-Sight (NLOS) transmission through the water surface and man-made reflector (e.g., mirror) in addition to the LOS link. First, utilizing the derived expression, we quantify the achievable NLOS gain defined as the ratio between the maximum achievable channel coefficient from reflection and the overall channel coefficient. Then, we validate our findings experimentally by utilizing the water surface and the mirror as the reflecting surfaces in an aquarium. Our results reveal that achievable gains up to around 3 dB can be observed due to reflections.

In the last part of this dissertation, we examine the impact of solar energy on the performance of vertical UVLC links in an underwater communication deployment scenario, which we analyze analytically and experimentally. In our study, we show that solar energy has a destructive impact on communication quality according to its position during the time of the day, day of the year, and location on the earth based on the visible light spectrum. Furthermore, to optimize the operation of this UVLC system, we propose optimization algorithms to achieve maximum Signal-to-Noise Ratio (SNR) to optimize the system parameters.

ÖZETÇE

Bilimsel veri toplama, çevreyi izleme, açık deniz petrol sahalarını keşfetme, arkeoloji, liman güvenliği ve gözetleme gibi insan faaliyetleri arttıkça, su altı iletişim sistemlerine olan talep de artmıştır. Su altındaki kablolu sistemler, çeşitli şekillerde gerçek zamanlı iletişim sağlayabilir. Bununla birlikte, kablolu sistemler, fiziksel olarak sabit yapıları, yüksek maliyetleri ve gerçek hayattaki çoğu durumda su altında kullanılmaya yönelik operasyonel dezavantajları ile sınırlıdır. Bu nedenle, su altı kablosuz iletişimi, araştırmacıların kaçınılmaz bir şekilde ilgisini çekmiştir. Su altı kablosuz veri iletimi, onlarca kilometreye kadar olan mesafeleri destekleme kapasitesi nedeniyle tipik olarak akustik sinyal kullanılarak gerçekleştirilir. Ancak, düşük veri hızı nedeniyle (onlarca Kilobit/Saniye (Kb/s) olarak), görüntü veya gerçek zamanlı video iletimi gibi yüksek bant genişliğine sahip su altı uygulamaları için uygun değildir. Bu nedenle, optik iletişim, düşük kapasiteli akustik iletişime yüksek kapasiteli bir alternatif sunar.

Suyun mavi ve yeşil ışığa karşı şeffaflığı sayesinde (450 nm – 550 nm), Lazer Diyotlar (LD) veya Işık Yayan Diyotlar (LED), potansiyel olarak onlarca Gigabit/Saniye (Gb/s) veri hızına sahip su altı kablosuz vericileri olarak hizmet verebilir. Teorik çalışmaların doğrulanması için herhangi bir teknolojinin deneysel doğrulama ve araştırmadan geçmesi gerekir. Bununla birlikte, Sualtı Görünür Işık İletimi (UVLC) sistemleri için daha fazla deneysel doğrulamaya ihtiyaç vardır. Spesifik olarak, su altı ortamlarında büyük zayıflama nedeniyle bir kaçınılmaz olan yol kaybının ele alınması gerekir. Yarı koşutlanmış optik sinyallerin sualtı yayılımı bu nedenle deneysel olarak doğrulanmalıdır. Deneysel olarak doğrulanmış zayıflatma modeline dayalı olarak, UVLC'nin performans kısıtlamalarını elde etmek için yarı paralelleştirilmiş kaynağa sahip bir UVLC sistemi daha fazla araştırılmalıdır. Dahası, su altında doğrusal yoldan alınan bir optik sinyalin, bir reflektör

yoluyla da aynı anda alındığında, toplamda alınmış optik sinyalin nasıl daha fazla geliştirileceğinin incelenmesinin gerektiği gibi, güneş enerjisinin sebep olduğu ısıl gürültünün, UVLC sistem performansını nasıl etkilediği ve bundan ötürü geliştirilebilecek iyileştirme çalışmalarına ihtiyaç vardır.

Bunlardan motive olarak, paralelleştirilmiş ve yarı paralelleştirilmiş bir UVLC zayıflama modelini deneysel olarak doğrulamayı hedefliyoruz. Bu nedenle, suyun sönümleme katsayısını ölçtükten sonra, paralel ölçümlerin doğruluğunu deneysel olarak doğrulayacağız. Ardından, çeşitli optik lensler kullanarak yarı koşutlanmış bir Gauss ışını oluşturduktan sonra, ışın sapma açısını ölçeceğiz. Daha sonra OKATEM Araştırma merkezindeki bir kapalı akvaryumdaki farklı su türlerini ve Gauss ışını şekillerine sahip paralelleştirilmiş ve yarı paralelleştirilmiş lazer kaynaklarını göz önünde bulundurarak UVLC yol kaybı kanal katsayısını belirlemek için ölçümler yapacağız. Son olarak, hem zayıflamayı hem de geometrik kaybı içeren teorik olarak önerilen kanal modelini deneysel olarak doğrulayacağız.

Ardından, halihazırda deneysel olarak doğruladığımız geleneksel UVLC yarı paralelleştirilmiş kanallara yeterince güvenerek, türbülans ve işaretleme hataları gözardı edilerek, UVLC sisteminin performans kısıtlamalarını araştıracağız. Hedeflenen bir Bit Hata Oranı (BER) performansı için, elde edilebilecek maksimum bağlantı mesafesi, kabul edilebilir maksimum ışın sapma açısı, kabul edilebilir minimum alıcı açıklık çapı ve kabul edilebilir maksimum su bulanıklığı için kapalı biçimli ifadeler türeteceğiz. Bu ifadeleri kullanarak, istenen BER performansını karşılamak için her sistem parametresinin saf deniz, berrak okyanus ve kıyı suyundaki simülasyon ortamındaki performansını M-li Tek Kutuplu Darbe Genlik Modülasyonu (M-UPAM) UVLC sistemleri için araştıracağız.

Görüş Hattı (LOS) bağlantıları için toplam yol kaybı kanal katsayısını doğruladıktan sonra, saçılan ışınların bir reflektörle kanal kazancını fotodetektöre yansıtarak destekleyeceğini gözlemleyeceğiz. Literatürde, reflektör destekli iletim tekniği, yalnızca daha yüksek alınan sinyal gücü için hem doğrudan hem de dağınık ışınlar alındıktan sonra elde edilir. Bu nedenle, LOS bağlantısına ek olarak su yüzeyinden ve insan yapımı reflektörden, yansımadan elde edilebilir maksimum kanal katsayısı ile genel kanal katsayısı arasındaki oran olarak tanımlanan ulaşılabilir Görüş Hattı Dışı (NLOS) kazancını inceleyeceğiz. Ardından, bir akvaryumda yansıtıcı yüzeyler olarak su yüzeyini ve aynayı kullanarak bulgularımızı deneysel olarak doğrulayacağız. Sonuçlarımız, yansımalar nedeniyle yaklaşık 3 dB'ye kadar elde edilebilir kazançların gözlemlenebileceğini ortaya koymaktadır.

Bu tezin son bölümünde, analitik ve deneysel olarak analiz ettiğimiz bir su altı iletişim konuşlandırma senaryosunda güneş enerjisinin, dikey UVLC bağlantılarının performansı üzerindeki etkisini inceleyeceğiz. Çalışmamızda, güneş enerjisinin günün saatindeki konumuna, yılın gününe ve görünür ışık spektrumuna dayalı olarak dünyadaki konumuna göre iletişim kalitesi üzerinde yıkıcı bir etkisi olduğunu göstereceğiz. Ayrıca, bu UVLC sisteminin çalışmasını optimize etmek için, sistem parametrelerini optimize etmek amacıyla maksimum Sinyal Gürültü Oranı (SNR) elde etmek için optimizasyon algoritmaları önereceğiz.

ACKNOWLEDGEMENTS

I want to express my great appreciation to my advisor, Prof. Murat Uysal, for his wisdom, encouragement, and invaluable insights and suggestions during this experience as a Ph.D. student. The work of this dissertation is only possible with his consistent support and guidance. I also had an excellent opportunity to work with him.

It is my pleasure to convey my gratitude to the members of my dissertation committee, Asst. Prof. Kadir Durak, Prof. Serhan Yarkan, Assoc. Prof. Sultan Aldırmaz Çolak and Assoc. Prof. Cenk Demiroğlu for their valuable time serving on my committee and carefully reviewing my dissertation.

My deepest gratitude is undoubtedly to Dr. Mohammed Elamassie for his enlightenment and guidance and for sharing his valuable time throughout my Ph.D. studies. Besides his technical guidance, his friendship is an invaluable asset to me. I will never forget his support and guidance for providing me with numerous opportunities to learn and develop. Moreover, I would like to thank İbrahim Bağlıca for being a good finisher in implementing the optical test systems and executing experiments together. We had very joyful times, especially inside the aquarium while conducting the experiments.

I would like to thank Burak Kebapçı and Anılcan Tosun for being good friends and being involved in most of the experiments. I would also like to thank all people both in OKATEM and CT&T research group for having fruitful discussions and having valuable time together. Besides, I want to thank all my colleagues in Airties Wireless Networks who have directly or indirectly worked with me and given their support.

My warmest gratitude goes to my parents, Yıldız and Kütükçü family, for their unconditional support and patience in my studies. I would like to lovingly thank my wife, Hande, for her unconditional love, unrestricted kindness, and unlimited patience. It would never be possible without her support on my studies.

ACRONYMS

AWGN	Additive White Gaussian Noise
BER	Bit Error Rate
Gb/s	Gigabits Per Second
GHz	Giga Hertz
Hz	Hertz
Kb/s	Kilobits Per Second
LD	Laser Diode
LED	Light Emitting Diode
LOS	Line of Sight
Mb/s	Megabits Per Second
MIMO	Multiple-Input Multiple-Output
MSE	Mean Squared Error
M-UPAM	M-ary Unipolar PAM
NLOS	Non-Line-of-Sight
OFDM	Orthogonal Frequency Division Multiplexing
PAM	Pulse-Amplitude Modulation
PD	Photo-Diode
RF	Radio Frequency
SNR	Signal-to-Noise Ratio
UOWC	Underwater Optical Wireless Communication
UVLC	Underwater Visible Light Communication
VLC	Visible Light Communication

TABLE OF CONTENTS

LIST OF TABLES

LIST OF FIGURES

LIST OF ALGORITHMS

CHAPTER I

INTRODUCTION

1.1 Motivation

Due to the continuous and unstoppable increase in human activities such as collecting underwater scientific data, monitoring the marine environment, exploring oil, archaeology, port security, and tactical surveillance, underwater communication systems are in constant demand [1]. A wire-line system (particularly a fiber optic system) can be utilized for real-time underwater communication. However, due to its high cost, lack of flexibility, and operational disadvantages, it is unsuitable for most practical applications. In response, underwater wireless communication has become increasingly popular.

Technologies such as Radio Frequency (RF), acoustic, and optical signaling are considered possible connectivity solutions. There is no doubt that RF is capable of short-range communications with data rates up to 100 Megabits Per Second (Mb/s), yet it is not always the best choice due to cost and size limitations, which are especially problematic for underwater communications. On the other hand, acoustic technology was looked upon as a viable long-distance communication technique. Although this technology has a lot of promise, its lack of data rate poses a significant challenge. To address these challenges, the Underwater Optical Wireless Communication (UOWC) concept has recently been proposed as a means of addressing them at data rates of up to tens of Mb/s . There is no doubt that most terrestrial devices these days are utilizing wireless communications in some form or another. A wide range of wireless communication applications in the underwater environment is of great interest to the military, the commercial market, and the scientific community [2, 3]. The ability to communicate underwater is essential for numerous applications that are considered contemporary applications for the 21st century. Examples of applications include mining natural minerals from the ocean, monitoring the marine ecosystem, and detecting rocks and objects inside the water for navigational purposes.

Light propagates through water by first absorbing ultraviolet and infrared signals, leaving visible light, mainly in the blue-green range, as the best wavelength for underwater transmission [4, 5]. Compared to the open ocean, there is a lower attenuation for the blue part of the spectrum in coastal waters, but a higher attenuation for the green part of the visible light spectrum in open waters [6]. Therefore, the blue-green region of the spectrum has been the focus of increasing research on UVLC [7–19]. This requires an in-depth study of UVLC systems' performance limits based on accurate optical channel gain models without turbulence, which can be viewed as an ideal benchmark.

As part of the design process for UVLC systems, one of the critical metrics is the channel model's accuracy. Thus, several theoretical UVLC channel models were developed as a result of conducting this research [20–24]. According to the mathematical derivations conducted in these studies, it is challenging to verify them experimentally. Therefore, for the experimental validation of these models, there is a need for a specific underwater test environment that can measure the properties of the water and the optical gadgets.

1.2 Overview of Underwater Wireless Communication

In the past few decades, acoustic systems have achieved excellent success underwater owing to their ability to communicate over a vast distance over many kilometers, which has led to a great deal of research in this area intending to improve this technology further. Acoustic communication channels have undergone extensive research to improve their performance [25–27]. However, its performance is dependent on the physical properties of the network, which are based on the fact that the bandwidth is limited, latency is high, transmission losses are high, multipath propagation is time-varying, and the Doppler spread is variable from one point to another [28–30]. The development of complementary technology that enables broadband underwater communication is therefore crucial. Real-time video transmissions, such as the operation of underwater vehicles and the monitoring of underwater stations, are becoming increasingly crucial in underwater applications [31–33]. Various communication methods are used on terrestrial earth, and RF waves are one of the most commonly used and diffused. However, even RF waves are unsuitable for underwater communications because they are heavily attenuated [34]. Aside from that, standard acoustic underwater communication is especially vulnerable to malicious attacks due to its low bandwidth, significant and variable propagation delays, and poor performance features, such as a high bit error rate and a significant and variable propagation delay.

Considering the extremely low scattering and absorption coefficients of fiber optic systems and their ability to operate in the near-infrared range of the spectrum, fiber optic systems are the best connectivity solution underwater for high data bandwidth and long distances. Nevertheless, this technology has an obvious disadvantage: It requires a physical connection between the transmitter and receiver to work. Consequently, it is not suitable for underwater communication systems for the practical deployments. In addition, wireless communication systems are required because of the difficulty of maintaining them and their high cost. Wireless communications in an underwater environment present a new set of challenges compared to wireless communications in an atmosphere. Several challenges are inherent to this environment: There is a need for sophisticated communication devices to achieve relatively low transmission rates, even at relatively short distances, due to the specific requirements of this environment [35]. Nevertheless, it is possible to achieve wireless communication under the ocean by using acoustics, RF, and optics as communication techniques. Below are some of the advantages and disadvantages associated with each:

- **Acoustic communications:** Underwater communication is most commonly reached by using acoustic waves as the primary wireless communication medium. In terms of range, acoustic waves offer the most extended range among the three technologies, with a reach of tens of kilometers. However, while underwater acoustic wireless technology has many advantages, it also presents many disadvantages, including very low propagation speeds, data rates, and multiple paths for the signal to propagate. Due to this, its popularity among underwater applications has declined over the past few years.

It is widely accepted that acoustic waves are one of the most effective forms of wireless communication in the underwater environment due to their relatively low absorption rate and broad coverage range. Acoustic waves are the most frequently used of the three types of wireless communication mentioned above. Consequently, a poor-quality signal is received, and as a result, the ability of human ears and brains to detect and process the speech being distorted through the distorted voice and [36] will be compromised. Over the past few decades, numerous researchers have developed sophisticated methods for channel estimation and algorithms for enhancing underwater acoustic communications so that it can provide a more effective service [37–40]. A considerable amount of effort has also been put into developing Orthogonal Frequency Division Multiplexing (OFDM) to achieve high data rates without needing complex equalizers to accomplish underwater acoustic communication [41–43] as well.

- **RF communications:** Acoustic signaling in water leads to poor performance and the extermination of marine life because it damages their environment. To achieve faster wireless transmissions an alternative communication method that can be used is RF signaling, which can be taken advantage of to achieve faster wireless transmissions. RF signaling does not suffer from temperature or depth effects like acoustic signaling, and it has two main advantages. First, a significant benefit of air/water molecules interacting with each other is that one can unify underwater and terrestrial communication through the easy and smooth penetration of RF waves. Furthermore, it has been demonstrated that RF as a communication medium can also tolerate turbulence and turbidity under hostile conditions. However, since RF communication suffers from a high degree of attenuation in underwater environments, it also requires a large antenna to prevent signal degradation due to attenuation in water. Thus, underwater communication with RF modules is limited to a short range and only suitable for short-range applications.

Underwater wireless communications have been explored as a means of improving data rates for further improvement by using RF waves because RF waves have a higher bandwidth and a faster velocity when they are used in acoustic environments. In addition to providing increased bandwidth and data rate, it also offers improved performance. According to the design and architecture of the system, it should be noted that RF waves can have frequencies ranging from a few tens of Hertz (Hz) to several Giga Hertz (GHz). A high-frequency electromagnetic wave is often used to establish communication paths between terrestrial and underwater bodies or communication routes between terrestrial and aquatic bodies. It is widely used for establishing communication paths between 30 - 300 Hz and is often used for extremely low-frequency electromagnetic waves. Due to this, they are being used for long-distance communication to serve submarines. Hence, there has been considerable success in communicating over long distances with submarines through these systems.

- **Optical communications:** When we compare UOWC with the methods above used for underwater wireless communication, we will find specific characteristics that make UOWC particularly exceptional. The most outstanding features of this technology include lower delay, increased security, higher data rate, and lower implementation costs. In real-time underwater image and video transmission applications, such as the transmission of underwater images and videos, UOWC is the most attractive underwater transmission method because of its high data rate. In addition, a UOWC system typically employs LOS configurations to execute the communications, offering a higher level of security than other methodologies used in other systems.

As for energy efficiency and cost-effectiveness, UOWC provides the most significant benefit in terms of energy efficiency and cost-effectiveness. Since RF signals are not efficient in freshwater, and they suffer from extreme attenuation in seawater, optical signals are an obvious choice for underwater communication due to their ability to support high data rates without sacrificing the size of the receiving antenna because they require enormous antennas and power to operate. Furthermore, since the optical carrier used in UOWC works at a high frequency, it can provide a data rate exceeding Gb/s even from a distance of several hundred meters due to its ability to operate at high frequencies. Despite the extreme challenges associated with optical signals in underwater environments, including water absorption or scattering caused by suspended particles and strong solar disturbances, many cases remain of optical links underwater over moderate distances. Multiple theoretical and experimental studies have been conducted to observe optical beam behavior underwater, including [44–46]. According to the literature reviewed in this dissertation, underwater wireless optical transmission over moderate distances can offer remarkably high data rates due to high-capacity optical systems.

Even though UOWC is a valuable system with many advantages, it is also a system with particular challenges. First, it is well known that optical photons are severely absorbed and scattered underwater, which is a significant problem. The transceiver configuration must be perfectly aligned with the transceiver configuration for optical links configured with LOS. Finally, it must be noted that the physical characteristics of water, including temperature and salinity, have a profound effect on its performance.

1.3 Underwater Optical Wireless Communication

Optical wireless communication has emerged as a new form of high-capacity communication to compete with its acoustic and RF counterparts. Water tends to be transparent to blue or green light with wavelengths between 450 nm and 550 nm, so LDs or LEDs can be used as underwater wireless transmitters with data rates of up to tens of Mb/s.

Table 1: Comparison of experimental UVLC systems in the literature.

Reference No	Transmitter Wavelength (nm)	Transmitter Type	Receiver Type	Data Rate (Mbps)	Link Distance (m)
[4]	520	LD	SiPM	100	24
[47]	450	LED	PIN	2340	1.2
[48]	450	LD	APD	4500	55
[49]	450 to 660	LED	PIN	14810	1.2
[50]	450	LD	APD	2500	60
[51]	457	LED	PIN	1690	1.2
[52]	450	LD	PIN	16160	5
[53]	532	LD	PD	200	1.6
[54]	450	LED	PIN	1179	1.2
[55]	450	LED	PIN	2925	1.2
[56]	520	LD	PD	100	10
[57]	450	LED	PIN	1740	1.2
[58]	532	LED	APD	10	6.5
[59]	457	LED	PIN	1220	1.2
[60]	470	LED	PMT	0.5	50
[61]	448	LED	APD	25	50
[62]	450	LD	APD	4800	5.4
[63]	450	LD	PIN	12400	1.7
[64]	488	LD	PIN	16000	10
[65]	450	LD	PIN	16600	55
[66]	680	VCSEL	PD	25000	5
[67]	450	LD	APD	1500	20
[68]	450	LD	SPAD	0.0005	144
[69]	680	VCSEL	APD	10000	6
[70]	450	LED	PIN	3075	1.2

In controlled lab environments, there have been numerous experimental demonstrations of UVLC systems by covering both high-speed and long-distance achievements [4,47–70]. In Table 1, a list of the experimentally achieved data rates and distances is presented, including wavelengths, transmitters, and receivers. These works focus on the maximum achievable data rate or distances with limited information given in the evaluation of the UVLC channel model. Many studies have been conducted to provide experimental verification and evaluation of UVLC channel models. The statistical distribution of the UVLC channel has been also evaluated by [71–78]. In Table 2, the statistical distributions of UVLC channels are surveyed based on experimental evaluations.

Table 2: List of experimental UVLC channel models in the literature.

Distribution Name	**Reference Number**
Simple Gamma Distribution	[71]
Weibull Distribution	[71], [75], [77]
Generalized Gamma Distribution	[71], [77]
Log-normal Distribution	[72], [74], [77]
Thermohaline Distribution	[73]
Gaussian Distribution	[74]
Exponential Distribution	[74]
Exponential Generalized Gamma Distribution	[75], [78]
Exponential Gamma Distribution	[76], [78]
Exponential Log-Normal Distribution	[76], [78]
Gamma-Gamma Distribution	[77]
Exponential Weibull Distribution	[77]

For the design and verification of a realistic UOWC system, it is essential to have an accurate underwater optical channel model. Experimental studies either examined the attenuation of UVLC channels as a function of collimated LOS or experimented with UVLC turbulence models as shown in Table 2. Within these empirical works, there was no particular study of semi-collimated beams in an experimental setup. As part of this dissertation, verifying both collimated and semi-collimated attenuation models for UVLC channels are delivered with a series of experiments.

1.4 Underwater Visible Light Channel Modeling

Optical signal losses in UVLC systems are due to geometric and attenuation losses. The geometrical loss results from the beam spreading beyond the aperture of the receiver due to the beam spreading to a larger size. Using the Beer-Lambert formula, an attenuation loss can be calculated under the assumption of a LOS link between the transmitter and receiver, and all scattered photons are lost [79]. This assumption is only valid when the turbidity of the water is low, such as in pure sea water [80]. There is a well-established tendency of the Beer-Lambert formula to overestimate the attenuation loss when the effects of turbidity are more severe (e.g., coastal water, harbor water). A modified version of the Beer-Lambert formula was proposed to accommodate such cases in [20].

The experimental UVLC channel models displayed in Table 2 are supplemented by additional experiments and verifications in further research as described in [81–84]. Using an empirical approach, [81] investigates the characteristics of a turbid water channel in terms of propagation in a multiple-scattering environment. An experimental study in [82] examines the effects of turbulence-induced scattering on the propagation of coherent and non-coherent light underwater. Microalgae have been examined in a series of experiments regarding their effects on UVLC applications [83]. These studies did not use the semi-collimated beam shape to characterize UVLC channels. In addition, a model of transmission based on different degrees of attenuation is presented in [84] based on measured channel measurements in the ocean. In [20], several closed-form expressions are presented. Therefore, the equations are predominantly based on curve fitting rather than system parameters. When the system parameters are changed, the channel model cannot be generalized since there is only one curve-fitting parameter. So, in order to design a practical UVLC system, experimental validation and verification of a semi-collimated UVLC channel model are particularly crucial.

1.5 Dissertation Outline

There are four main components to the dissertation, which can be summarized as follows:

1. In the first part of this dissertation, we will explain how the UVLC channel model is validated. We will first measure the extinction coefficient of the system, then introduce the test system in which we measure collimated beams. Following that, we will perform path loss verification tests in our test measurement system. As the next step, we will show how we generate Gaussian semi-collimated beams in our experimental design, again using Gaussian LD and various optical elements. Next, we will introduce the test system in which we take the channel measurements in detail. With this test system, we will verify the path loss and then show the verification of our semi-collimated measurements.

2. In the second part of this dissertation, we reveal a system model to demonstrate the operation of the semi-collimated UVLC system. Then, using the experimentally verified channel model presented in the previous section, we develop closed-form expressions for the maximum achievable link distance between the transmitter and receiver, maximum acceptable beam divergence angle, minimum acceptable receiver aperture diameter, and the maximum acceptable water turbidity limit. Lastly, we use these closed-form expressions to evaluate the constraint of a semi-collimated UVLC system by performing a series of simulations that analyze the system constraints.

3. In the third part of this dissertation, we propose a closed-form expression for the underwater path loss that incorporates the NLOS reflections (e.g., mirrors) and the LOS link. To compute reflected power, we use a hypothetical photodetector that enables

us to factor in the orientation of light propagation into the calculation, effectively allowing us to incorporate the geometry of light propagation into the calculations. Furthermore, we use the same expression for quantifying the overall NLOS gain derived from the maximum achievable channel coefficient from reflection, commonly referred to as the ratio between the overall channel coefficient and the maximum achievable channel coefficient. As a result of the proposed experimental setup, several implementation challenges will be discussed. Finally, an aquarium experiment was conducted to confirm our findings.

4. In part four of this dissertation, we discuss how to achieve optimum performance within the deteriorating effects of solar energy on underwater optical communication systems. Our assumptions in this chapter are that the receiver lens is a motorized energy harvesting panel that can detect optical signals for communication purposes. We first reveal the system model to calculate the maximum SNR. Then, based on different wavelengths and water concentrations, we develop an analytical model of the water extinction coefficient. Next, concerning different latitudes, the time of day, and the day of the year, we demonstrate the mathematical modeling of solar noise based on depth, water extinction coefficient, and tilt angles. Finally, we present optimization algorithms to maximize the SNR ratio of the system after bringing all system parameters together.

1.6 Organization

The organization of this dissertation is as follows. The purpose of Chapter 2 is to demonstrate the path loss verification of both collimated and semi-collimated UVLC signals by introducing experimental test systems used to validate UVLC channel measurements. Using the experimentally verified channel model, Chapter 3 demonstrates the maximum achievable link distance, maximum acceptable beam divergence angle, minimum acceptable receiver aperture diameter and maximum acceptable water turbidity in closed-form representations. Then, as a result of adding a reflector to support semi-collimated LOS transmission, in Chapter 4, we will show mathematically and experimentally how much signal gain a reflector may provide to the existing measurement of channel coefficients on account of the NLOS measurements. In Chapter 5, we will mathematically demonstrate how the UVLC system's SNR can be calculated at various depths and water concentrations, considering how solar energy debilitates the optical signal transmission underwater based on the time of the day and day of the year in a relevant latitude. With the help of this mathematical model, we intend to introduce scenarios where the system will reach its maximum SNR in case the several optimum system parameters in the UVLC communication systems. More explicitly, these chapters are organized as follows:

- The Chapter 2 is divided into two sections. The purpose of Section 2.2 is to examine the collimated measurement system. We will first demonstrate how we can measure the extinction coefficient to accomplish this. Following this, we will measure the collimated LOS optical channel power and verify the path loss values based on the extinction coefficient acquired in our test bed. Next, in Section 2.3, we will initially measure the extinction coefficient of two types of water and validate the extinction coefficient values via collimated measurements. Then, we will explain how to develop a Gaussian beam shape by measuring the beam divergence angle. Following that, we will present our experimental test setup for measuring the semi-collimated signal within our aquarium to conduct our experimental testing. Following this, we will compare the experimentally obtained semi-collimated path loss values and their theoretical equivalents in two types of water by considering the geometrical loss of the semi-collimated signals.

- There are three sections in Chapter 3. First, we will present the UVLC performance measurement system model in Section 3.2. In Section 3.3, we will calculate closed form analytical modeling of the system and measurement parameters to obtain the desired system performance. This system and its measurement parameters include the maximum achievable distance (Section 3.3.1), the maximum acceptable beam divergence angle (Section 3.3.2), the minimum acceptable receiver aperture diameter (Section 3.3.3), and the maximum acceptable water turbidity that the system can operate (Section 3.3.4). Afterward, we will display the numerical values of these mathematical outputs to compare their performance in Section 3.4.

- Chapter 4 is organized as follow. In Section 4.2, we will introduce the system model. The next step will be to mathematically demonstrate the proposed NLOS channel model in Section 4.3. Then, in Section 4.4, using both a mirror and the signal gain from the surface of the water, we will validate the proposed theoretical gain with the experimental measurements. Eventually, we will discuss some of the practical aspects we have observed in our NLOS UVLC channel measurement studies in Section 4.5.

- Chapter 5 is composed of four sections. The Section 5.2 reveals the system model for delivering the underwater link that can be affected by the sun and the relevant extinction coefficients. Then, solar noise is calculated in Section 5.3 based on the different tilt angles. The SNR is calculated by bringing all system parameters together in Section 5.4. Finally, in Section 5.5, we propose optimization algorithms for the system to maximize the SNR values depending on several locations and days to optimize both the tilt angle and the wavelength concerning the hour of the day.

CHAPTER II

EXPERIMENTAL UVLC CHANNEL MODELING

2.1 Introduction

This chapter aims to demonstrate our experimental test system for measuring UVLC channel coefficients to design an accurate UVLC transceiver for practical applications. In several experimental studies, an accurate UVLC channel model was developed to understand the accuracy of collimated signals. However, no comprehensive validation study was conducted for the semi-collimated UVLC channel model, which should have considered both the attenuation loss and the geometric loss.

Therefore, the following is a breakdown of the chapter's structure. Section 2.2 is to examine the collimated measurement system. We will first demonstrate how we can measure the extinction coefficient to accomplish this. Following this, we measure the path loss values based on the extinction coefficient acquired in our test bed. Then, we will validate the collimated system path loss measurements with the theoretical values. In Section 2.3, we will cover the experimental measurements of the semi-collimated UVLC channel model. First, we will verify the path loss measurements of two types of water that we conduct semi-collimated measurements. Next, we will reveal how we measure the beam divergence angle of the semi-collimated Gaussian beam shape. Following that, we will present our experimental test setup for measuring the semi-collimated optical power within our aquarium to conduct our experimental testing. Later on, we will verify the experimentally obtained semi-collimated UVLC path loss values and their theoretical equivalents in two types of water by considering the attenuation loss and the geometrical loss of the semi-collimated signals.

2.2 Collimated Measurements

In this section, we will show how to measure the extinction coefficient of the water medium to be used in the collimated measurements. We consider a communication link illustrated in Figure 1. The source and detector are submerged in water, creating a horizontal link with a distance of d. Since the collimated optical signal is considered to follow the Beer-Lambert law (i.e., $(h = \exp(-cd))$, we first need to measure the extinction coefficient, then verify the channel coefficient experimentally. We placed both LD and Photo-Diode (PD) sensors inside a separate cuvette.

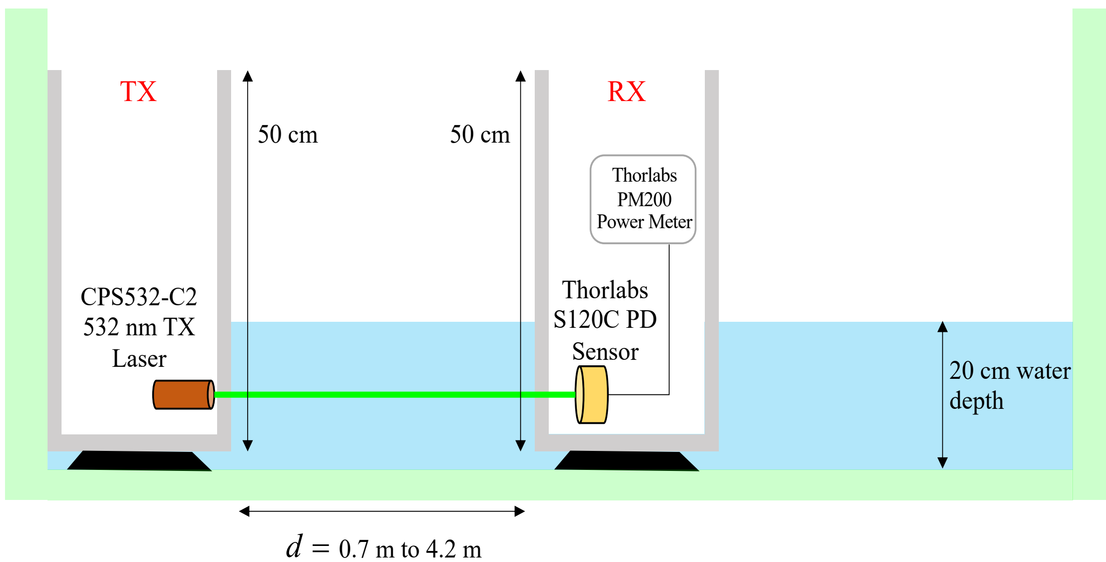

Figure 1: Extinction coefficient measurements test system.

These cuvettes are used to place the LD (Thorlabs CPS532-C2 532 nm laser) and PD (Thorlabs S120C) inside the inner cuvettes (having 11 % loss) because the loss occurring due to the outer aquarium glass was measured to be 20 %, which would undermine the measurements' accuracy. Therefore, due to the lower loss in the inner cuvettes that can be seen in Figure 2 on the next page, we have placed both cuvettes with rails placed at the bottom inside the aquarium with the dimensions of $1\text{m} \times 1\text{m} \times 8\text{m}$.

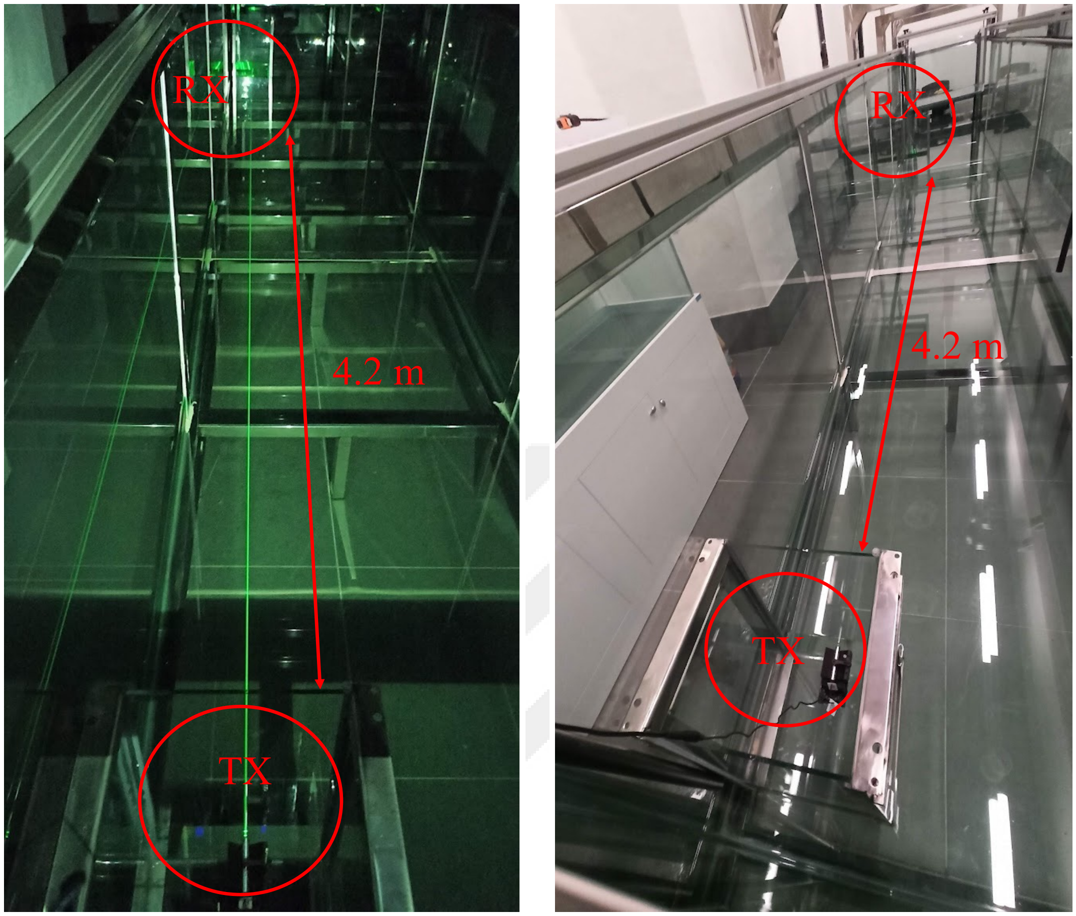

(a) (b)

Figure 2: Collimated measurements in $1\,\text{m} \times 1\,\text{m} \times 8\,\text{m}$ aquarium (a) background lights off and (b) background lights on.

2.2.1 Extinction Coefficient Measurement

Various sophisticated measurement devices are available to measure absorption coefficients and turbidities. A spectrophotometer was initially used to measure the absorption coefficient to extract the extinction coefficient value of the water sample in which we performed our experiments. Nevertheless, a significant obstacle led us to establish our measurement methodology to determine the absorption coefficient first and then calculate the extinction coefficient accordingly. Our spectrophotometer measurement device gave us a relative absorption coefficient instead of an aggregate extinction coefficient. So, we decided to use our test bed for extinction coefficients within the same test date we conducted. To build such a system to measure the extinction coefficient, the power output of the Thorlabs CPS532-C2 532 nm green LD was measured in an aquarium with dimensions of $1\,\text{m} \times 1\,\text{m} \times 8\,\text{m}$ by using a Thorlabs PM200 power meter, as shown in Figure 1 on page 15.

2.2.2 Path Loss Verifications

Using a Thorlabs PM200 power meter, as shown in Figure 3, the power output of the Thorlabs CPS532-C2 532 nm green LD was used to measure the optical power between two cuvettes. Let P_i represent the power at a given moment, and P_o represent the power when the measurement was taken. It is possible to determine the extinction coefficient using Equation (2.1) as

$$c_i = \frac{-\ln\left(\frac{P_i}{P_o}\right)}{(d_i - d_o)}, \tag{2.1}$$

where d_i and d_o represent the distance between the laser source and detector at an instant and the distance at the beginning.

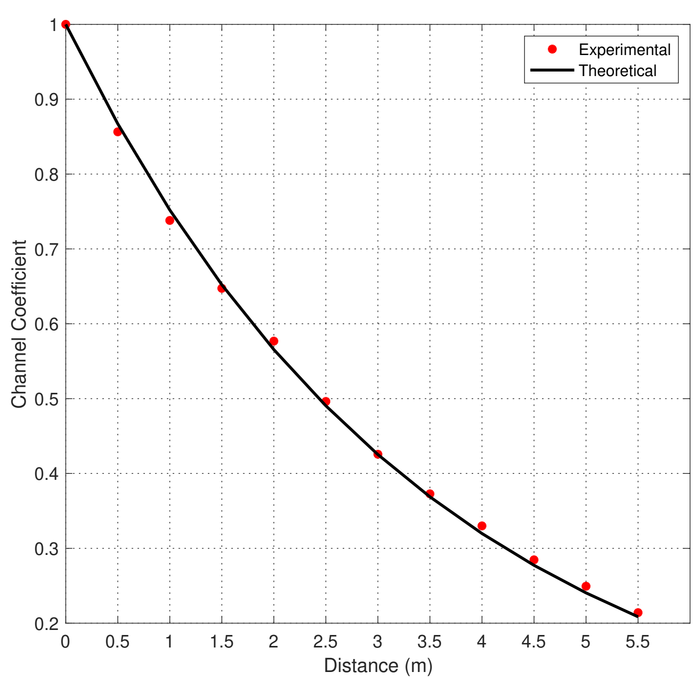

Figure 3: Path loss verification of the collimated UVLC measurement system.

The average extinction coefficient can be calculated based on the recorded power values difference between the distances Equation (2.1) on the previous page. When calculating the extinction coefficients based on the measurements, the calculated extinction coefficient is $c = 0.28\,\mathrm{m}^{-1}$. When we compare the Beer-lambert formula by using the calculated extinction coefficient value with the LOS measurements in our experiments, the normalized channel coefficient values are within ± 0.015. Figure 3 on the preceding page demonstrates both the theoretical Beer-Lambert formula and the normalized channel coefficient values together.

2.3 *Semi-Collimated Measurements*

The purpose of Section 2.2 is to demonstrate how to measure the extinction coefficient by validating the path loss of the collimated measurements. Our method involves the use of the extinction coefficient as a way of validating the collimated measurements, which includes the loss of the test system. Therefore, this section will demonstrate the path loss verification of the desired test system before moving on to the semi-collimated measurements. Next, we show how to identify a semi-collimated UVLC beam divergence angle of the optical beam. Afterward, we will indicate our entire test equipment in our test bed. Finally, we will measure the semi-collimated UVLC signals by comparing theoretical and experimental values achieved within this test system.

2.3.1 Path Loss Verifications

Before moving on to semi-collimated measurements, we first performed extinction coefficient measurements on both series. Using a Thorlabs PM200 power meter, as shown in Figure 4 on the next page, the power output of the Thorlabs CPS532-C2 532 nm green LD was measured in an aquarium with dimensions of $1\,\mathrm{m} \times 1\,\mathrm{m} \times 8\,\mathrm{m}$ to determine the extinction coefficient. In both transmitter and receiver cuvettes, there is an approximate $11\,\%$ loss in optical signal due to reflections from the glasses.

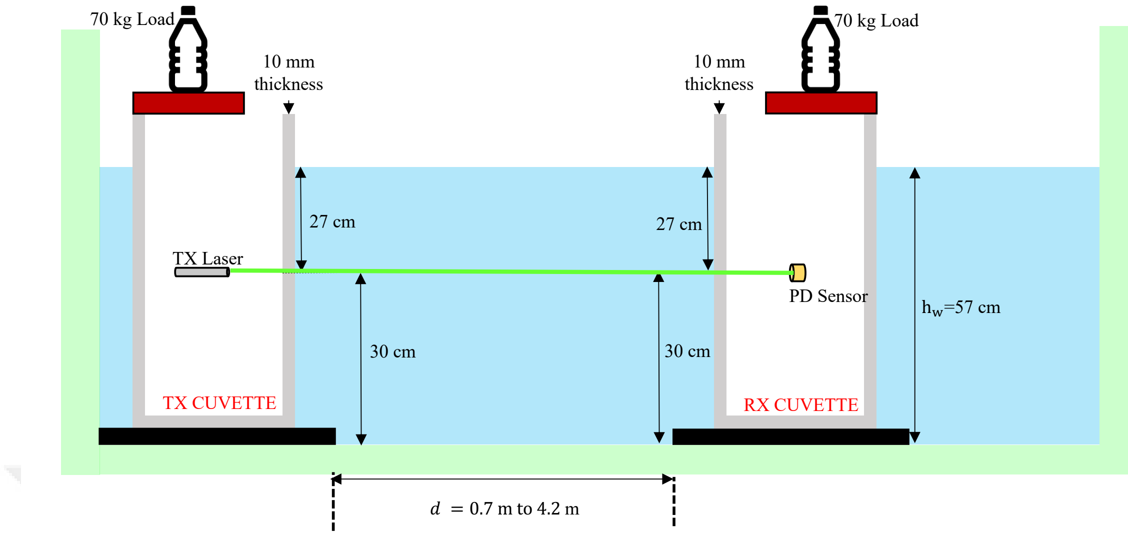

Figure 4: Extinction coefficient measurements test system for semi-collimated signals.

Therefore, we measured the extinction coefficients of clean and coastal water at intervals of 50 cm between both LD and PD cuvettes. After recording the power values, we calculate the extinction coefficient by taking the first measured power values (i.e., $d = 0.7$m). Then, as shown in the Section 2.2, we calculate the extinction coefficients of the water on two different days and different conditions as calculated by Equation (2.1) on page 17.

Table 3: Extinction coefficient measurements

	Coastal Water		**Clean Water**	
Distance (m)	**Measured Power (mW)**	c	**Measured Power (mW)**	c
0.7	1.945	N/A	3.42	N/A
1.2	1.180	1.000	3.070	0.216
1.7	0.723	0.990	2.720	0.229
2.2	0.425	1.014	2.430	0.228
2.7	0.275	0.978	2.140	0.234
3.2	0.153	1.017	1.850	0.246
3.7	0.095	1.006	1.630	0.247
4.2	0.058	1.004	1.450	0.245

The data given in Table 3 on the previous page indicate the power measurements for all calculated extinction coefficients. Based on the average of all extinction coefficients from every measurement of both water types, the extinction coefficient for clean water is $\left(c = 0.239\,\mathrm{m}^{-1}\right)$, while for coastal water, it is $\left(c = 1.001\,\mathrm{m}^{-1}\right)$. Here in Table 3 on the preceding page, c is considered the calculated extinction coefficient. The calculated extinction coefficients provided a series of measurements on a particular day with both water types. According to Figure 5, to provide a collimated measurement test system, the LD and PD are placed inside inner cuvettes of 10 mm glass thickness, with 11 % losses. Since the glass of these cuvettes has a higher permeability than the external aquarium, we have placed both transmitters and receivers inside them.

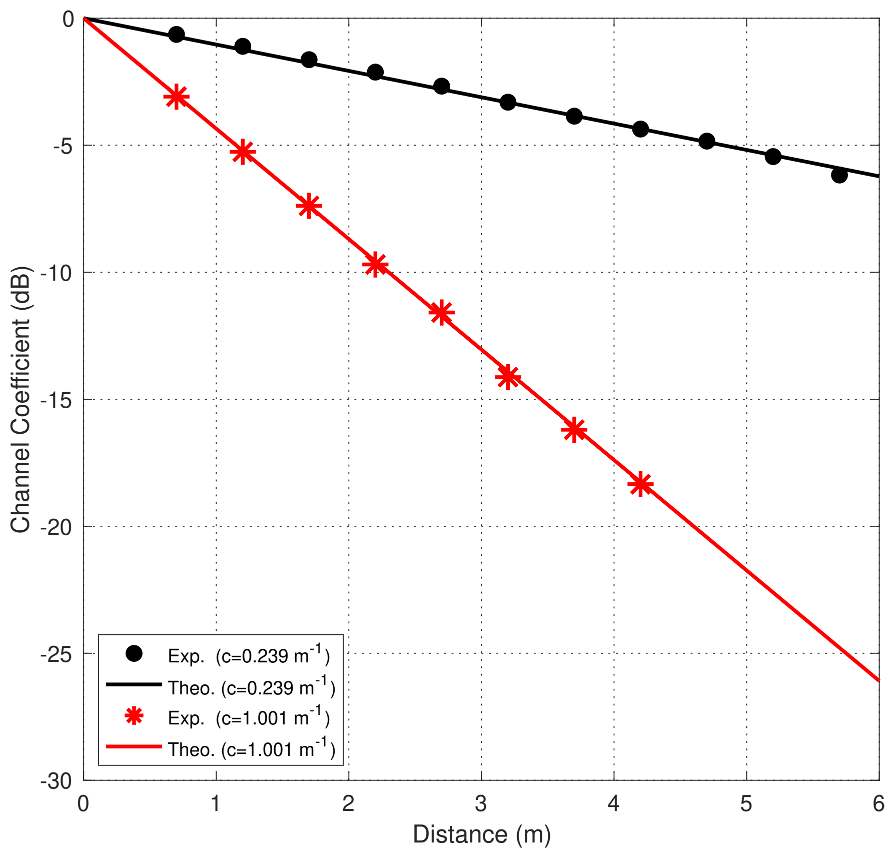

Figure 5: Collimated measurements verification.

The measurements of the received power within this test system will be accounted for by

$$P_R = P_T h \Omega, \tag{2.2}$$

where P_R represents the received power, P_T represents the transmitted power, and Ω represents the total system loss. In Ω, two inner glass losses of the LD and PD cuvettes are accounted for, where the total loss is calculated as 79.2 % due to reflections on the glass. 5 mW of output power is available from the Thorlabs CPS532-C2 green LD at 532 nm. So, h can be written in logarithmic scale by

$$h_{\mathrm{dB}} = P_{\mathrm{R,dBm}} - P_{\mathrm{T,dBm}} + 1.012\,\mathrm{dB}. \tag{2.3}$$

Based on the received power values at each distance, we get a good match for both clean-water $\left(c = 0.239\,\mathrm{m}^{-1}\right)$ and for coastal-water $\left(c = 1.001\,\mathrm{m}^{-1}\right)$ as seen in Figure 5 on the preceding page.

2.3.2 Construction of Semi-Collimated Gaussian Beamshape

Our approach was to place a Plano-Concave Lens by Thorlabs LC1715-A N-BK7 with a focal length of $f = -50\,\mathrm{mm}$ to create a semi-collimated signal obtained from the Thorlabs LC1715-A N-BK7.

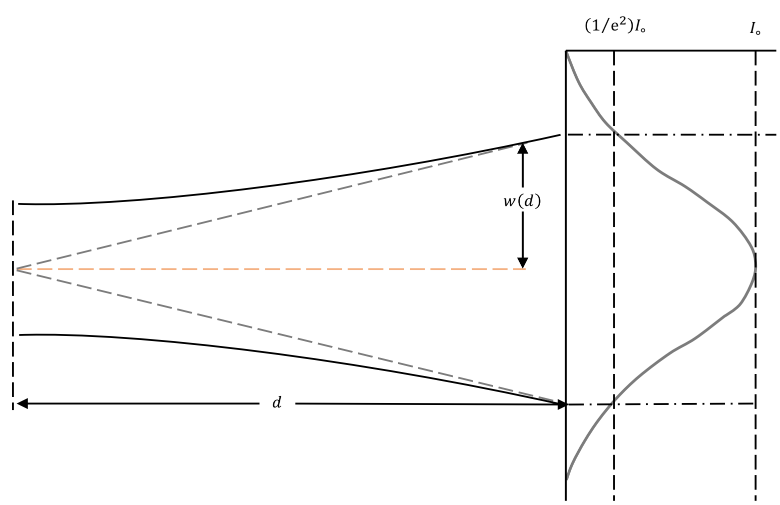

Figure 6: Gaussian laser source.

The first step we took was to verify the distribution property of the semi-collimated optical signal to compare the measured values with the theoretical values based on these assumptions before moving on to the calculations. Based on the results presented in [85], the waist of the beam at a closer distance is equal to $w(d)$, where $1/e^2$ is calculated to be the adequate peak power at that distance. According to Figure 6 on the previous page, the half-width of a Gaussian beam ($w(d) = d\tan(\theta/2)$) can be defined at a distance d from the laser source as $w(d) = d\tan(\theta/2)$, and $\theta_{1/2} = \theta/2$ can be defined as the divergence angle for the half-width beam. As seen in Figure 7, we can see that the semi-collimated optical signal follows a Gaussian distribution with $R^2 \geq 0.99$. This indicates that the effective beam divergence angle is calculated based on the transmitter configuration, which is $\theta = 3.68°$.

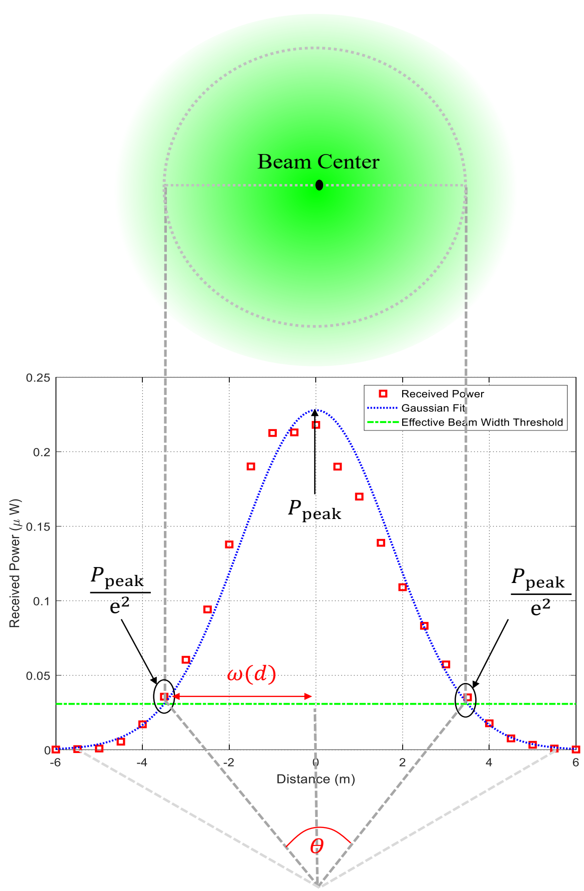

Figure 7: Semi-collimated beam shape distribution verification.

2.3.3 Experimental Test Setup

Before we move on to semi-collimated measurements, the experimental test system shall be carefully designed. This section reveals the experimental system components for an end-to-end semi-collimated UVLC channel measurement system.

2.3.3.1 Transmitter

The semi-collimated optical signal is driven by the Thorlabs CPS532-C2 532 nm LD as shown in Figure 8. We use Thorlabs LC1716-A N-BK7 Plano-Concave Lens to obtain a semi-collimated signal, as indicated in Section 2.3.2. The transmitter unit will then be placed inside a cuvette, allowing the semi-collimated optical signal to be transmitted like that described in Figure 9 on the following page.

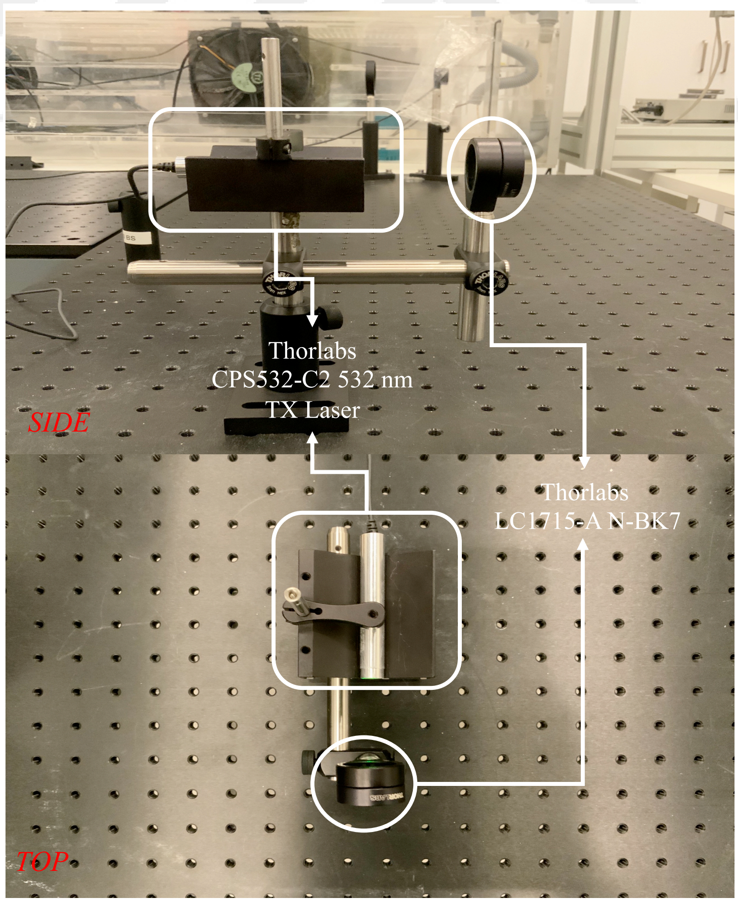

Figure 8: Semi-collimated UVLC transmitter blocks.

As shown in Figure 9(a), the cuvette to be placed inside the aquarium will have dimensions of $0.3 \times 0.3 \times 0.5$ m. Figure 9(b) illustrates the transmission of a semi-collimated signal over a distance of 4.05 m while the cuvette operates. The semi-collimated beam extends into a diameter of 42.5 cm when fully extended. However, this beam shape is a Gaussian beam shape and has $\theta = 3.68°$.

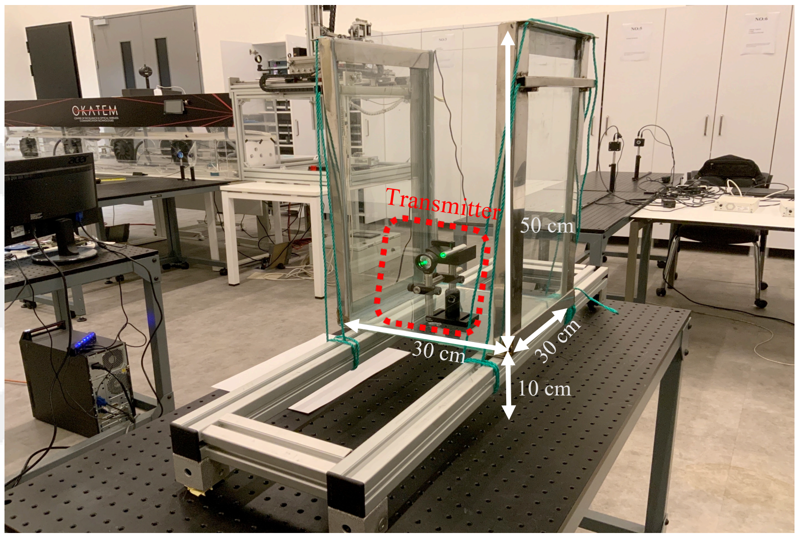

(a)

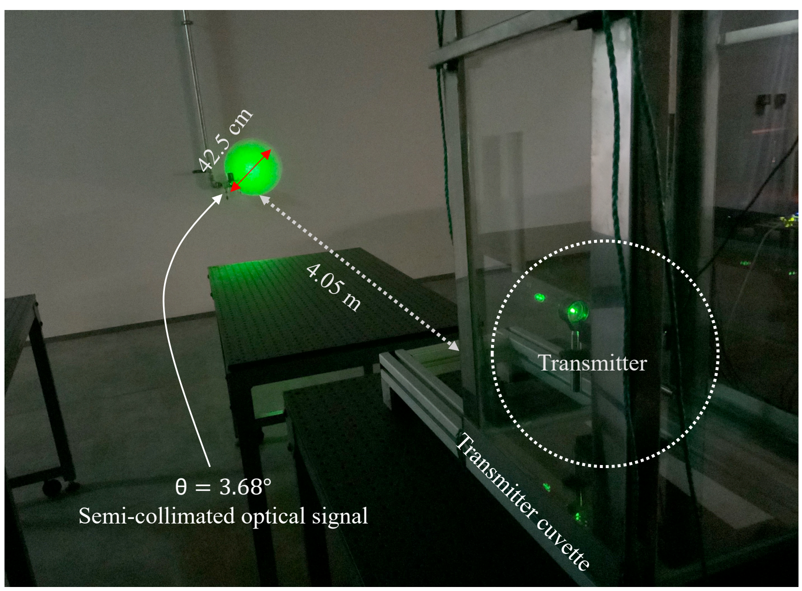

(b)

Figure 9: Semi-collimated UVLC transmitter test bed (a) inside a cuvette with dimensions and (b) optical signal transmission up to 4 m.

2.3.3.2 *Receiver*

We have selected a lens in our lab as the receiver unit, as it is readily available in our laboratory. It has been determined that the Thorlabs LB-1309-B receive lens will have a focal length of $f = 75$ mm, which provides a receiver aperture diameter of 50.4 mm.

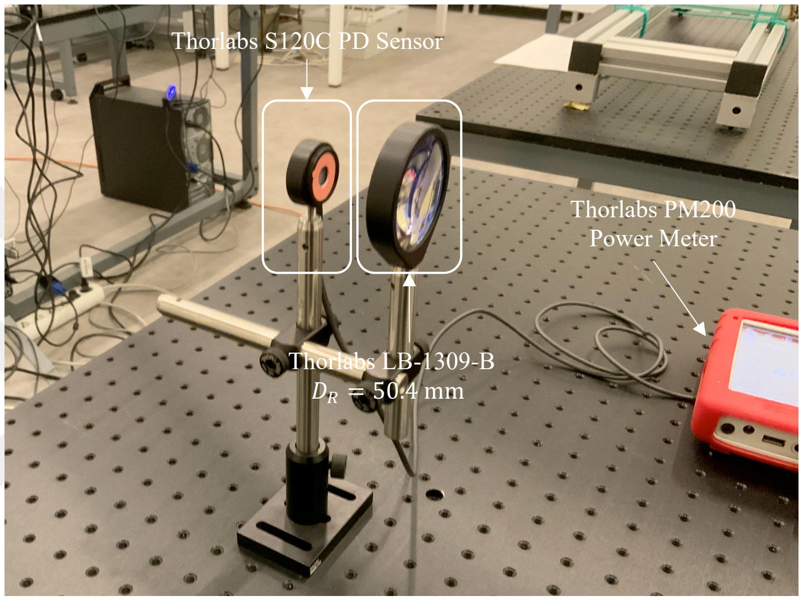

(a)

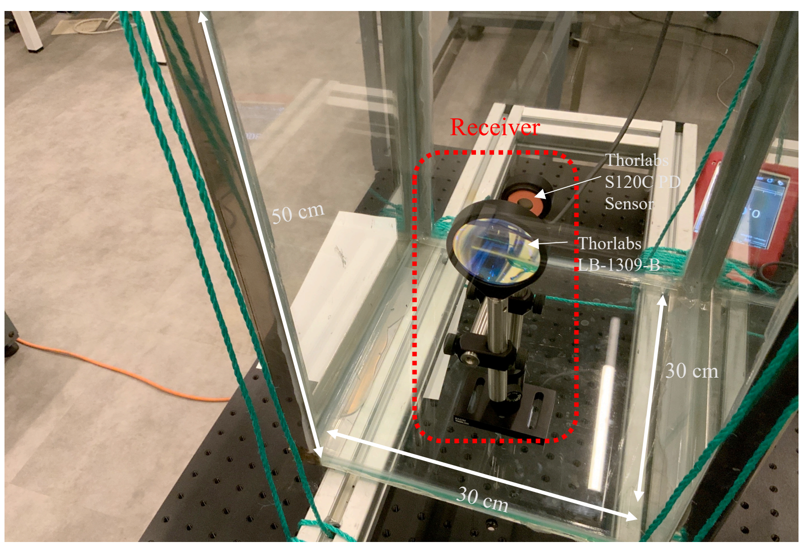

(b)

Figure 10: Semi-collimated UVLC receiver in (a) receiver unit and (b) receiver unit test bed.

As shown in the Figure 10(a) on the previous page section, the optical signal is focused and maximized at the Thorlabs S120C PD sensor connected to a Thorlabs PM200 power meter, as shown in Figure 10(b) on the preceding page. Therefore, although the Thorlabs LB-1309-B lens has a coated AB coating, it can still enable the system to capture the optical signal in the visible spectrum with a loss of 11% based on the datasheet of the lens provided by Thorlabs [86].

2.3.3.3 Experimental Test Bed

A transmitter cuvette is designated in Section 2.3.3.1 on page 23, and a receiver cuvette is denoted in Section 2.3.3.2 on the preceding page. When putting the transmitter and receiver cuvettes into the aquarium according to the table in Figure 11, the cuvettes are then placed inside the aquarium. Water buoyancy against the cuvette bottom area was one of the biggest obstacles encountered during the testing. This created a significant challenge in stabilizing the test cuvettes while submerged in water. However, since the diameter of the Gaussian beam reaches a maximum of 50 cm at a distance of $(d \geq 5\,\text{m})$, we have filled the water level h_w at the top of the cuvette up to $h_w = 57$ cm without exceeding the height of the cuvette.

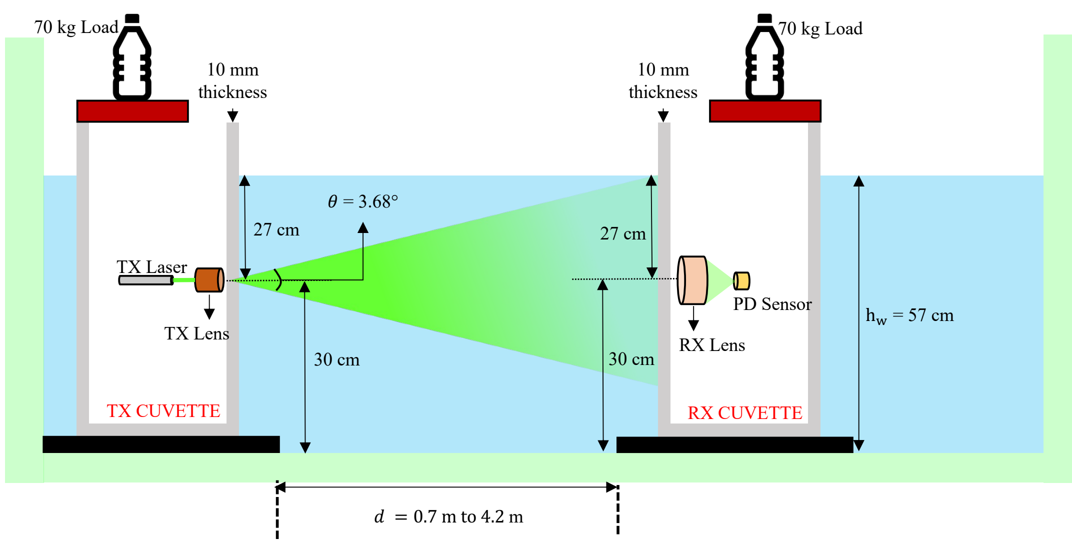

Figure 11: UVLC experimental measurement test system layout.

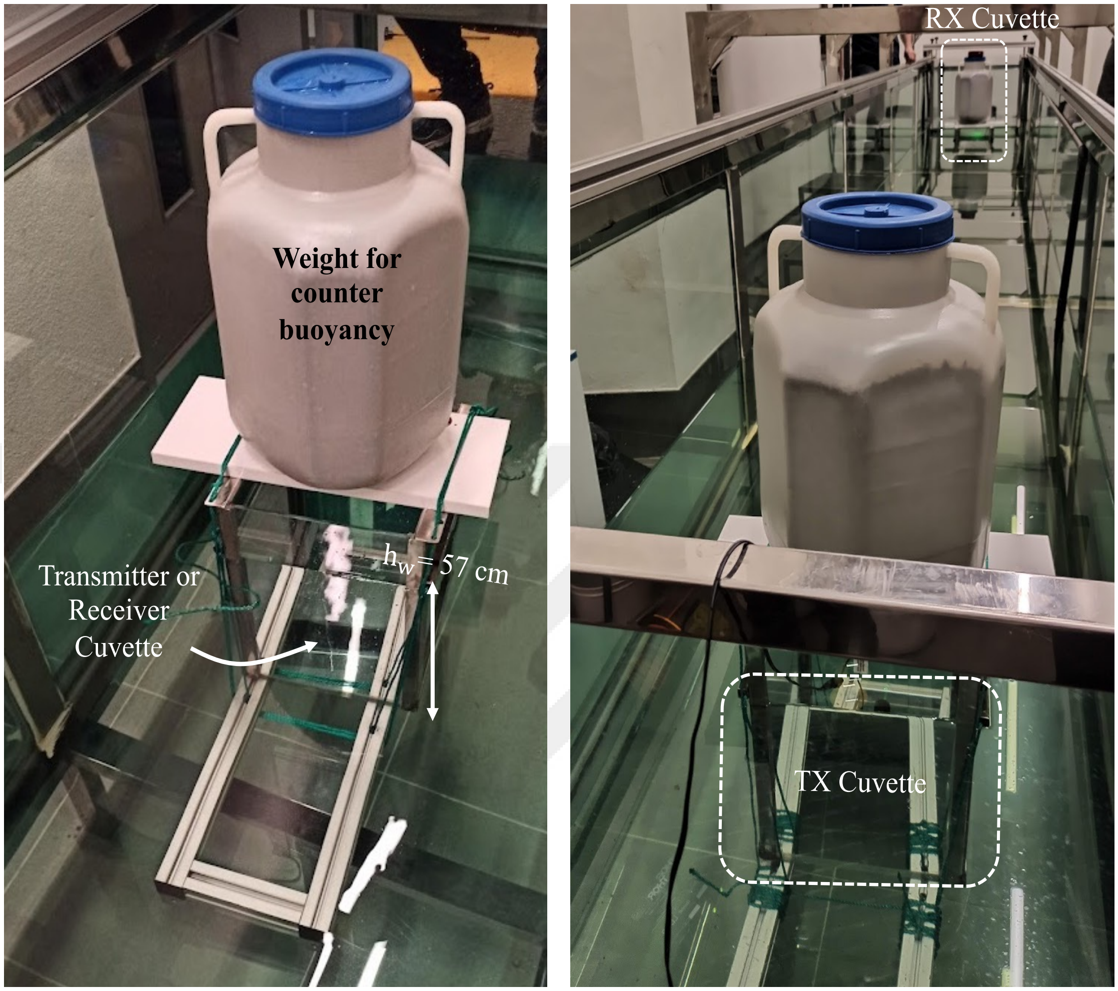

(a) (b)

Figure 12: UVLC experimental measurement test cuvettes (a) single test bed and (b) complete experimental test system with cuvettes.

Since the water in the aquarium is filtered for a while, it is best to fill it first and then put the cuvettes inside the water afterward, as filling up the water may introduce some contaminants due to municipal water systems. This is why we filled the water up to $h_w = 57$ cm at the beginning. In the next step, the extinction coefficient of the water was measured. As shown in Figure 11 on the preceding page, the semi-collimated measurements are followed by the extinction coefficient measurement. In addition, the cuvettes can be maintained in their original position and alignment by installing a rail at their bottom. The optical power measurements will then be able to be carried out at the desired measurement intervals in a consistent manner. In Figure 12 on the previous page, it is possible to see how the experimental test system is assembled and the components that make it up. When placing each cuvette in an aquarium filled with water, each must be aligned accurately to get reliable measurements of its power. Changing the distance (d) between the transmitter and receiver cuvettes has allowed us to ensure that the optical path will follow an exact horizontal alignment as we have moved the receiver cuvette to the correct position on the optical path. Our transmitter and optical receiver circuitry were always realigned every time the receiver cuvette was moved, regardless of where the receiver cuvette was placed. To obtain maximum power measurements with the receiver lens, the optical signal must be focused on the center spot of the PD sensor to ensure that the optical power is located at the epicenter of the Gaussian beam at all times.

2.3.4 Semi-Collimated UVLC Measurements

Under the assumption of non-turbid water, underwater path loss can be approximated as [80, 87]

$$h \approx \left[1 - \exp\left(-2\frac{(D/2)^2}{w^2(d)}\right)\right] \exp(-cd), \tag{2.4}$$

where $w(d) = d\tan(\theta/2)$ represents the Gaussian beam half-width at a distance d from the laser source with the half-width beam divergence angle $\theta_{1/2} = \theta/2$, and c is the extinction coefficient as denoted in Section 2.3.2. In addition, D is the receiver aperture diameter of the optical receiver unit.

To build an experimental test system for measuring the semi-collimated optical signal channel coefficient, we realize the test system inside the same aquarium and inner cuvettes as shown in Figure 13 on the following page. In the experiments, we use the LD setup to generate the semi-collimated signal with $\theta = 3.68°$.

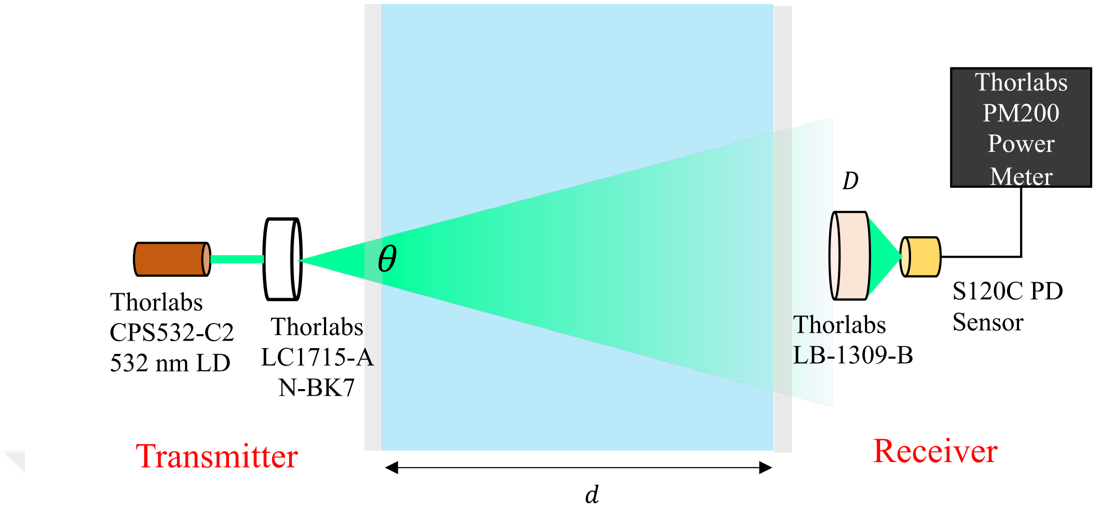

Figure 13: Semi-collimated UVLC experimental measurement test system.

At the receiver side, we have used a $D = 50.4$ mm Thorlabs LB-1309-B with the focal length of $f = 75$ mm. Two aspects need to be considered for the validity of the semi-collimated power measurements. First, transmitter and receiver nodes shall be kept in perfect alignment. Since we use an experimentally validated Gaussian beam as given in Section 2.3.2 on page 21, the most accurate channel coefficient can be acquired when the detector measures the center of the beam. Keeping the inner cuvettes with 0.3×0.3 m bottom area and 50 cm height steady inside the water was a great challenge during the experiments due to the buoyancy of the water on cuvettes. We placed heavy weights to ensure both cuvettes are steady and not leaving the LOS path as given in Figure 12(a) on page 27 and Figure 12(b) on page 27.

Furthermore, our system will employ the power measurements given in Equation (2.2) on page 21. The test system includes a coated AB lens with 11 % loss in 532 nm, so we need to include the loss of the lens into the overall system loss to accurately compare the experimental channel coefficient measurements and the theoretical measurements. So, the experimental channel coefficient measurements are given as

$$h_{\mathrm{dB}} = P_{R,\mathrm{dBm}} - P_{T,\mathrm{dBm}} + 1.518\,\mathrm{dB}. \tag{2.5}$$

Here, we have recorded the transmitted and received power values for two different water types where the extinction coefficient measurements are already provided in the Section 2.3.2, namely for the clean water $\left(c = 0.239\,\mathrm{m}^{-1}\right)$ and for the coastal water $\left(c = 1.001\,\mathrm{m}^{-1}\right)$. The cuvettes that carry the laser source and the power meter are the same ones used for collimated measurements. Experimental measurements are provided when there is a 70 cm difference between the initial locations of the cuvettes as seen in Figure 11 on page 26. Then, the power is recorded every 50 cm intervals. Our semi-collimated optical power can reach up to 5.7 m for clean water and 4.2 m for dirty water. From the experimental channel coefficients, we achieve a very close match with the theoretical formula given in Equation (2.4) on page 28 as shown in Figure 14.

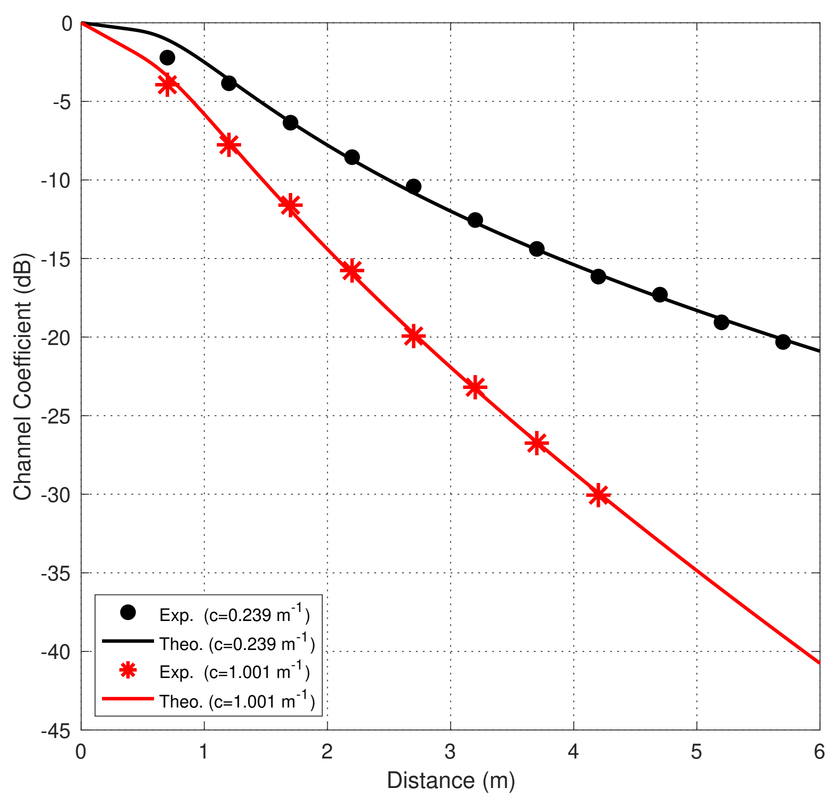

Figure 14: Semi-collimated UVLC channel coefficient verifications.

In this chapter, we conducted experimental validation studies to understand the propagation of collimated and semi-collimated optical signals underwater. For short-range UVLC measurement systems, the conventional Beer-Lambert formula provides sufficient accuracy, considering the Geometric loss during experimental studies. We will propose several closed-form expressions using this conventional channel model to reveal the performance limits of semi-collimated UVLC test systems.

CHAPTER III

PERFORMANCE LIMITS OF UVLC SEMI-COLLIMATED SYSTEMS

3.1 Introduction

In the Chapter 2 of this dissertation, we revealed how we performed channel coefficient measurements of semi-collimated UVLC systems in an aquarium that has an 8 m length in total. These measurements showed us that the conventional Beer-Lambert formula is an accurate approximation at short distances for both collimated and semi-collimated measurements with geometric loss. Furthermore, when we create a semi-collimated UVLC communication link scenario based on this channel model that has been verified experimentally, knowing the system's performance constraints is quintessential for every single parameter inside the system. Therefore, in this chapter, we will derive each system parameter in closed-form expressions depending on the desired BER performance of an M-UPAM UVLC system with this channel model.

The construction of this chapter is given as follows. There are three sections in Chapter 3. First, we will present the UVLC performance measurement system model in Section 3.2. Then, in Section 3.3, we will calculate closed-form analytical modeling of the system and measurement parameters to obtain the desired system performance. This system and its measurement parameters include the maximum achievable distance (Section 3.3.1), the maximum acceptable beam divergence angle (Section 3.3.2), and the minimum acceptable receiver aperture diameter (Section 3.3.3), and the maximum acceptable water turbidity limit that the system can operate (Section 3.3.4). Afterward, we will display the numerical values of these mathematical outputs to compare their performance in Section 3.4.

3.2 System Model

We consider a communication link illustrated in Figure 15. The source and detector are submerged in water, creating a horizontal link with a distance of d. Link distance for a given system setup and water type can not exceed a maximum achievable distance of d_{max} for complying with the required system performance. The source is equipped with a semi-collimated LD with a tunable beam divergence angle (i.e., θ) and directed toward the single PD with the receiver aperture diameter D. Both LD and PD are equipped with various optical circuitries in practical implementation, as we discussed one example of a semi-collimated UVLC experimental design in the previous chapter. So, optical lenses and other components providing the desired beam divergence angle and the receiver aperture diameter within the system model in Figure 15 are omitted.

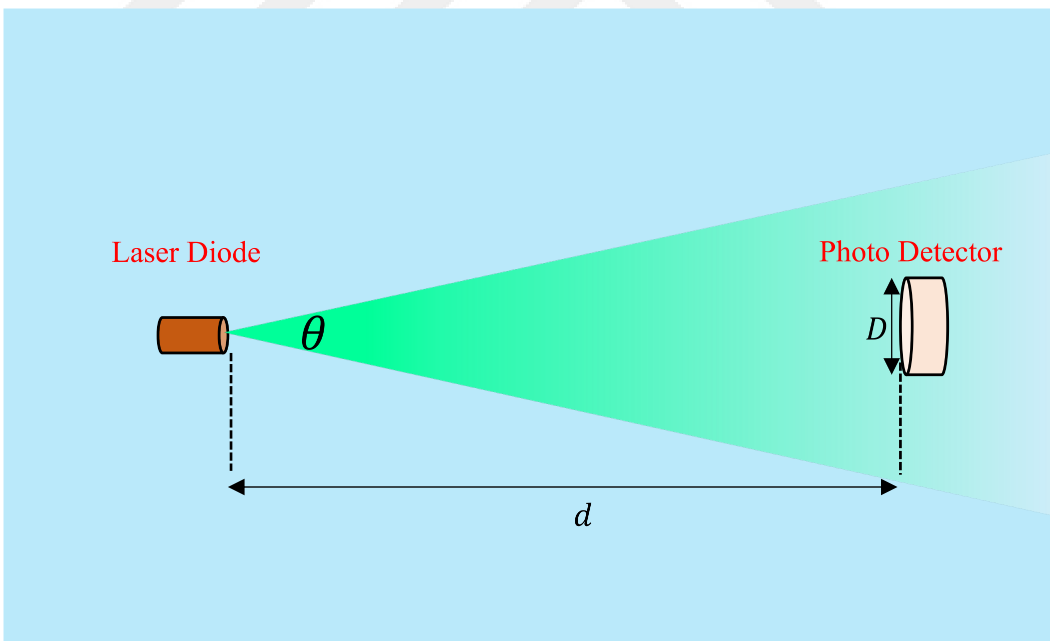

Figure 15: Semi-collimated UVLC system model.

To build the desired UVLC system, we employ an M-UPAM. The detected signal can be expressed as

$$y = \sqrt{P_{\text{te}}}\, \eta\, r\, h\, x + w, \tag{3.1}$$

where x is the M-UPAM modulation signal, η is the LD 's electro-optical coefficient, and r is the PD 's opto-electrical coefficient, P_{te} is the average electrical transmit power, h is the optical channel coefficient due to path loss, and w is the additive white noise and is modeled as $w \sim \mathcal{N}\left(0, \sigma_n^2\right)$. In other words, w follows a Gaussian distribution with zero mean and variance of σ_n^2. The path loss (h) in Equation (3.1) on the preceding page is subject to attenuation and geometric loss [20, 88]. Under the assumption of non-turbid water, underwater path loss can be approximated as

$$h \approx \underbrace{\left[1 - \exp\left(-2\frac{(D/2\,)^2}{\omega^2\,(d)}\right)\right]}_{h_G} \underbrace{\exp\,(-cd)}_{h_P}, \tag{3.2}$$

where $w\,(d) = d\,\tan\,(\theta/2)$ is the Gaussian beam half-width at a distance d from the laser source (see Figure 6 on page 21) with $\theta_{1/2} = \theta/2$ denoting half-width beam divergence angle, c is the extinction coefficient, h_G is the channel coefficient due to the geometric loss, and h_P is the channel coefficient due to the attenuation loss.

3.3 *Performance Limits*

The previous section presented an expression of the underwater path loss in a closed form that was validated experimentally. The purpose of this section is to derive the system constraints for achieving a specified maximum acceptable level of BER ($P_{\mathrm{e,T}}$) based on this validated expression.

Consider the case where the SNR for γ_{req} is required to make it possible to obtain $P_{\mathrm{e,T}}$. The relationship between $P_{\mathrm{e,T}}$ and γ_{req} depends on the particular system and modulation type being taken into account. Based on M-UPAM, the relationship between BER (P_{e}) and SNR (γ) can be expressed as followed by [89]

$$P_e = F\ \mathrm{erfc}\left(\sqrt{C\gamma}\right), \tag{3.3}$$

where $F = (M-1)/(M\log_2(M))$ and $C = 3/(2(M-1)(2M-1))$. SNR (γ) can be written utilizing Equation (3.1) on page 33 as

$$\gamma = \frac{P_{\mathrm{te}}\,\eta^2\, r^2\, h^2}{\sigma_n^2}. \tag{3.4}$$

Based on Equation (3.3) on the previous page, γ_{req} that satisfies a maximum acceptable probability of $P_{\mathrm{e,T}}$ can be expressed as

$$\gamma_{\mathrm{req}} = C^{-1}\left(\mathrm{erfc}^{-1}\left(P_{\mathrm{e,T}}/F\right)\right)^2. \tag{3.5}$$

As a result of the Equation (3.4) and Equation (3.5), we can determine the required channel coefficient h to achieve $P_{\mathrm{e,T}}$. It is mathematically possible to derive the following

$$\begin{aligned} h_{\mathrm{req}} &= \sqrt{\frac{\gamma_{\mathrm{req}}\sigma_n^2}{P_{\mathrm{te}}\eta^2 r^2}} \\ &= \sqrt{\frac{\sigma_n^2 C^{-1}}{P_{\mathrm{te}}\eta^2 r^2}}\left(\mathrm{erfc}^{-1}\left(P_{\mathrm{e,T}}/F\right)\right). \end{aligned} \tag{3.6}$$

3.3.1 Maximum Achievable Distance

To solve the path loss formula in Equation (3.2) on the preceding page for d, we need to use the approximations of $\tan(x) \approx x,\ x \ll 1$ and $\exp(x) \approx 1 + x,\ x \ll 1$ [90]. First, we can arrange the resultant expression as

$$\frac{h\theta^2}{2D^2} \approx d^{-2}\exp(-cd). \tag{3.7}$$

If we raise both sides of Equation (3.7) to the power of -0.5, we have

$$\sqrt{\frac{D^2 c^2}{2h\theta^2}} \approx 0.5\,cd\exp(0.5\,cd). \tag{3.8}$$

The right-hand side of this expression is in the form of $(x\,e^x)$ whose inverse can be taken by the Lambert-W function, i.e.,$\mathrm{W}(x\,e^x) = x$ [91]. Utilizing this, we can solve the channel coefficient to extract d as

$$d \approx \frac{2}{c}\mathrm{W}\left(\sqrt{\frac{D^2 c^2}{2h\theta^2}}\right). \tag{3.9}$$

Utilizing Equation (3.7) on the preceding page and Equation (3.9) on the previous page, we acquire the maximum achievable distance as

$$d_{\max} \approx \frac{2}{c} \mathrm{W} \left(\sqrt{\frac{\sqrt{P_{\mathrm{te}}} \eta^2 r^2 D^2 c^2}{2\sqrt{\sigma_n^2 C^{-1}} \left(\operatorname{erfc}^{-1} \left(P_{\mathrm{e,T}}/F \right) \right) \theta^2}} \right). \tag{3.10}$$

3.3.2 Maximum Acceptable Beam Divergence Angle

Since the link distance is short, a semi-collimated beam is essential to ensure a large enough receiving beam spot for detecting and tracking the receiving beam signal and facilitating the acquisition and tracking of the signal. To achieve optimal performance, it is, therefore, necessary to have the maximum beam divergence angle possible. Despite this, the larger the beam divergence angle, the greater the geometric loss, leading to a decrease in the SNR. Hence, the first step would be to solve Equation (3.2) on page 34 for θ. Then, using Equation (3.6) on the previous page within this resultant expression, we achieve the $\theta_{\max}$ as

$$\theta_{\max} \approx 2\tan^{-1} \left(d^{-1} \sqrt{\frac{-2(D/2)^2}{\ln \left[1 - \exp(cd) \sqrt{\frac{\sigma_n^2 C^{-1}}{P_{\mathrm{te}} \eta^2 r^2}} \left(\operatorname{erfc}^{-1} \left(P_{\mathrm{e,T}}/F \right) \right) \right]}} \right). \tag{3.11}$$

3.3.3 Minimum Acceptable Aperture Diameter

Based on the limited short link distance in combination with the different water types having a variety of turbidity levels, the performance of the BER system can be tuned based on the receiver aperture diameter selected based on a target BER performance to be achieved. To achieve optimal performance, it becomes critical to choose the optimal receiver lens to collimate the optical signals to achieve optimal results. Hence, the aperture diameter of the receiver can be decreased to achieve the minimum BER values under the same system parameters. Having solved Equation (3.2) on page 34 for D, we are able to find $D_{\min}$ within the resultant expression when we take Equation (3.6) on the previous page as input

$$D_{\min} = 2\sqrt{-\frac{\omega^2(d)}{2}\ln\left(1-\frac{\left(\sqrt{\frac{\sigma_n^2 C^{-1}}{P_{\mathrm{te}}\,\eta^2\,r^2}}\left(\operatorname{erfc}^{-1}\left(P_{\mathrm{e,T}}/F\right)\right)\right)}{\exp\left(-c\,d\right)}\right)}. \tag{3.12}$$

3.3.4 Maximum Acceptable Water Turbidity

Depending on the system parameter configurations, the UVLC system may work if the turbidity of the water is below a given level. Our objective in this sub-section is to derive the maximum acceptable water turbidity in extinction coefficient c, where we can achieve the targeted BER performance. The first step is to solve Equation (3.2) on page 34 for c. As a result of using Equation (3.6) on page 35 within the resultant expression, we will be able to construct

$$c_{\max} = -\frac{1}{d}\ln\left(\frac{\left(\sqrt{\frac{\sigma_n^2 C^{-1}}{P_{\mathrm{te}}\,\eta^2\,r^2}}\left(\operatorname{erfc}^{-1}\left(P_{\mathrm{e,T}}/F\right)\right)\right)}{1-\exp\left(-2\,\frac{(D/2)^2}{\omega^2(d)}\right)}\right). \tag{3.13}$$

3.4 *Numerical Results*

After revealing each system component in a closed-form expression, our objective in this section will be to demonstrate the performance limits a semi-collimated UVLC system can achieve. Specifically, to satisfy the specific error rate performance requirements, we investigate the maximum achievable link distance, maximum acceptable beam divergence angle, minimum acceptable receiver aperture size, and maximum acceptable water turbidity limits. Unless otherwise stated, the assumption is that the aperture diameter of the receiver is $D = 5$ cm, the transmitter beam divergence angle of $\theta = 6^\circ$, the noise power ${\sigma_n}^2 = -100$ dBm, the average electrical transmit power $P_{\mathrm{te}} = 10$ dBm, a distance of $d = 10$ m, $M = 4$ as the modulation order, and the extinction coefficient of 0.056 m^{-1}, 0.150 m^{-1}, and 0.305 m^{-1}, denoting the pure sea, clear ocean, and coastal water respectively [88]. Furthermore, the LD 's electro-optical coefficient, η, is taken as 0.5 W/A, while PD 's opto-electrical coefficient (r) is used as 0.28 A/W.

Firstly, we investigate the maximum possible link distance in different water types for the system configuration. In Figure 16, for different maximum acceptable BER values, we present the achievable distance for pure sea, clear ocean, and coastal water. It is observed from Figure 16 that the maximum link distance is 21.85 m for pure sea at $P_{\mathrm{e,\,T}} = 10^{-6}$. On the other hand, the achievable distance decreases to 14.05 m and 9.48 m, respectively, for the clear ocean and coastal water. This is because the optical beam attenuates more during propagation through the water with a higher extinction coefficient. Additionally, one can notice that the targeted BER influences the maximum possible link distance. For example, assuming pure sea, the maximum possible distance of 21.85 m for $P_{\mathrm{e,\,T}} = 10^{-7}$ drops to 21.24 m, 20.72 m, and 20.28 m, respectively, for targeted BER of $P_{\mathrm{e,\,T}} = 10^{-7}$, $P_{\mathrm{e,\,T}} = 10^{-8}$, and $P_{\mathrm{e,\,T}} = 10^{-9}$.

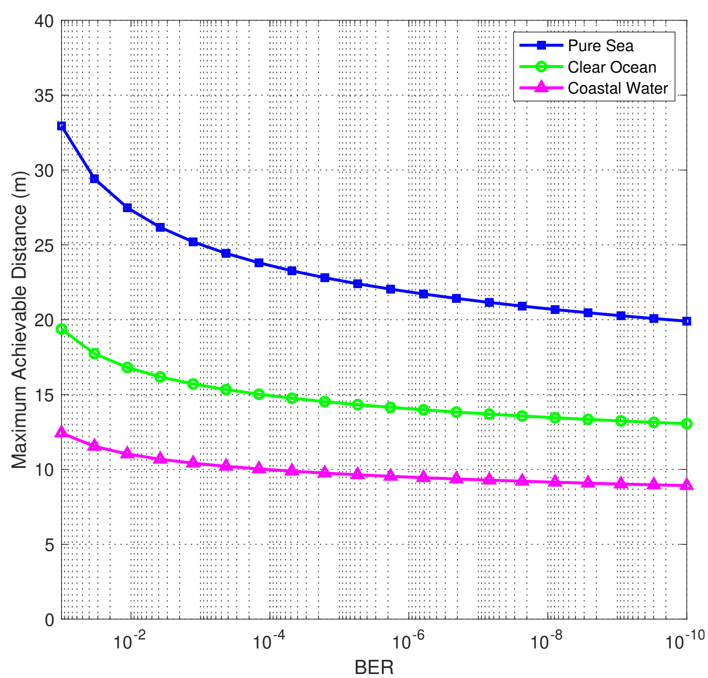

Figure 16: Maximum achievable distance.

Secondly, considering different water types, we investigate the maximum acceptable beam divergence angle to achieve the acceptable BER values. It can be observed from Figure 17 that the maximum acceptable beam divergence angle decreases as the extinction coefficient increases. For example, θ_{max} is 18.12° for pure sea assuming $P_{\text{e,T}} = 10^{-6}$. It decreases to 11.38° and 5.25°, respectively, assuming clear ocean and coastal water. Due to the higher extinction coefficient of water, the optical beam attenuates more during propagation through it. To compensate for the increase in attenuation, focused beams ensure that more power is collected. Here, the considered link distance is used as $d = 10$ m, and the receiver aperture diameter is 5 cm.

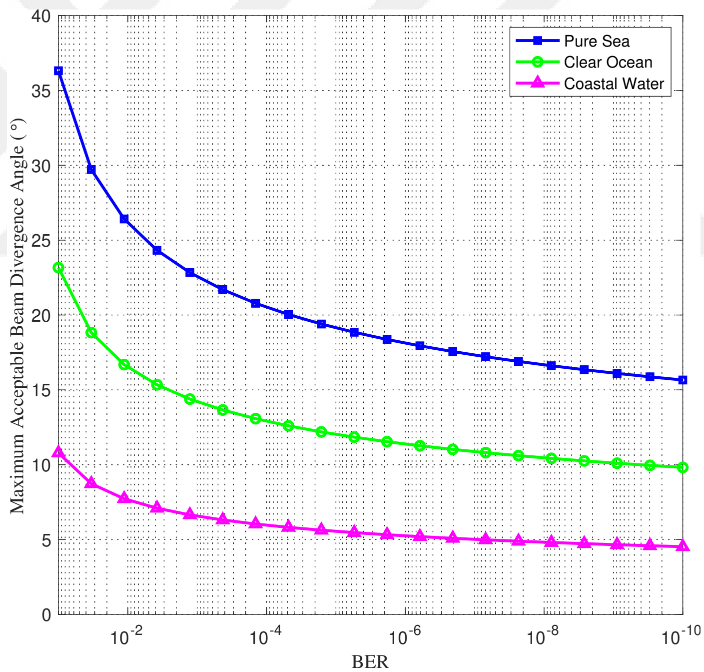

Figure 17: Maximum acceptable beam divergence angle.

Third, we have already investigated the minimum acceptable receiver aperture diameter to achieve the desired BER values based on the different water types used in Figure 16 on the previous page (for maximum achievable distance) and Figure 17 (for maximum acceptable beam divergence angle). Keeping the distance ($d = 10$ m) and the beam divergence angle ($\theta = 6°$), it can be observed from Figure 18 on the next page that the minimum acceptable receiver aperture size is to increase as the extinction coefficient increases to achieve the same system performance at the desired error performance. As an example, assuming $P_{e,T} = 10^{-6}$, the minimum acceptable receiver aperture diameter D_{min} is calculated as 1.64 cm. When we place the system in the clear ocean, and coastal water types, the required receiver lens diameter shall increase to 2.62 cm and 5.71 cm, respectively. The main reason for the increase in the receiver aperture diameter is the need to collect more optical photons in the same water to compensate for the decreased performance due to the increased turbidity.

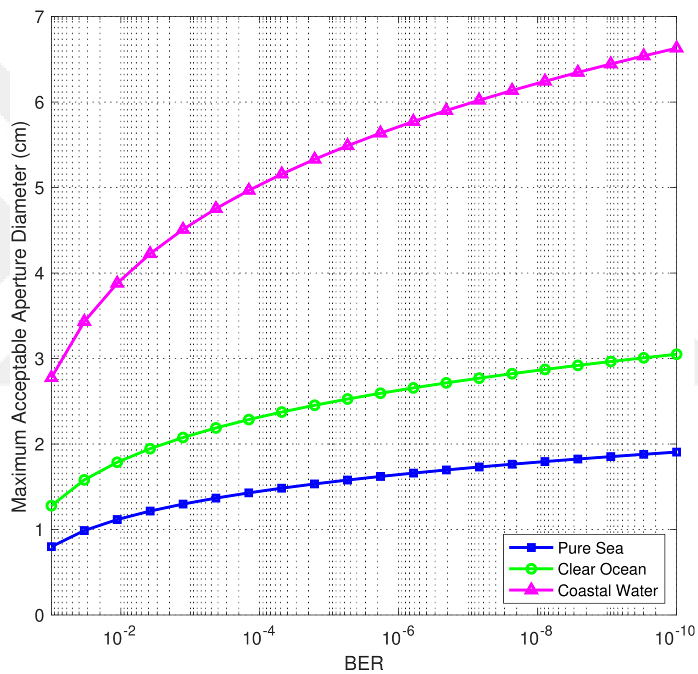

Figure 18: Minimum acceptable receiver aperture diameter.

As a final point, if the water turbidity increases, the system parameters may no longer be able to handle work under the same BER performance. Therefore, we investigate the maximum acceptable water turbidity to make the system work for various parameter and link distance combinations. As seen from the Figure 17 on the preceding page and Figure 18, if the link distance is too short, the required performance is satisfied in the most considered scenarios of beam divergence angle and receive aperture diameter. For example, to achieve $P_{e,T} = 10^{-6}$, the maximum extinction coefficient values of the system that can tolerate can be achieved as $0.33\,m^{-1}$, $0.28\,m^{-1}$, and $0.24\,m^{-1}$, respectively, for the combinations of

($\theta = 6°$, $D = 5$ cm, $d = 9$ m), ($\theta = 6°$, $D = 5$ cm, $d = 10$ m), and ($\theta = 6°$, $D = 5$ cm, $d = 11$ m) as observed in Figure 19. This is because both attenuation and geometric losses increase with propagation distance (see Equation (3.2) on page 34).

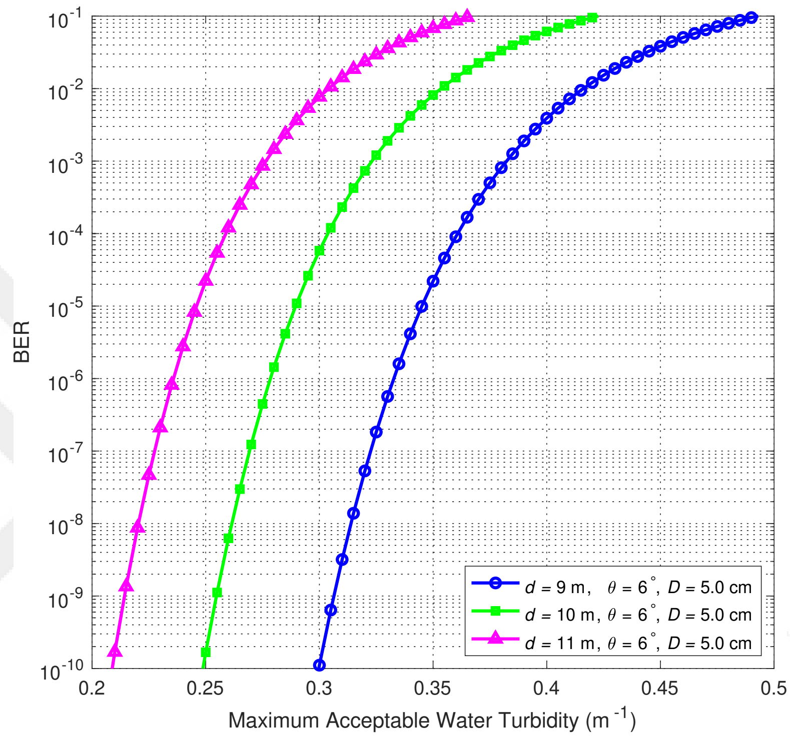

Figure 19: Maximum acceptable water turbidity based on distance (d).

A similar discussion can be considered for the beam divergence angle. A smaller beam divergence angle allows systems to work up to a higher extinction coefficient. For example, as given in Figure 20 on the following page, assuming $d = 10$ m and $D = 5$ cm, the required targeted BER, $P_{e,T} = 10^{-7}$, can be achieved while extinction coefficient is less than $c = 0.41\,m^{-1}$ assuming $\theta = 3°$. For higher beam divergence angles such as $\theta = 6°$ and $\theta = 9°$, the required targeted BER can be achieved while the extinction coefficient is less than $c = 0.27\,m^{-1}$ and $c = 0.19\,m^{-1}$, respectively.

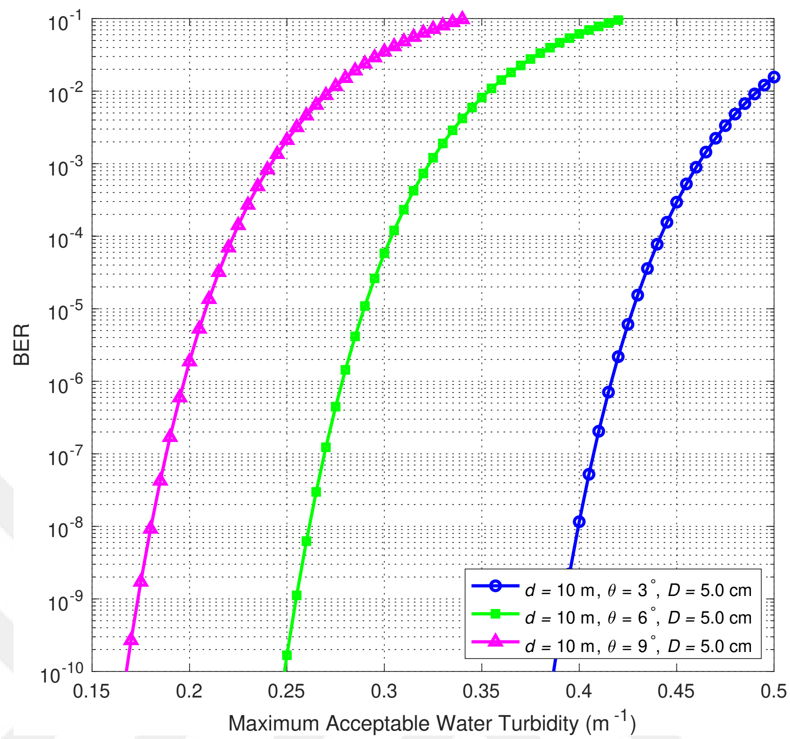

Figure 20: Maximum acceptable water turbidity based on beam divergence angle (θ).

Contrary to the achievable link distance and maximum acceptable beam divergence angle, the decrease in the receiver aperture diameter will decrease the collected optical photons. Hence, as the receiver aperture diameter increases, it is expected that the UVLC system can perform at higher extinction coefficients. The example values can be explicitly observed in Figure 21 on the next page, which considers $d = 10$ m and $\theta = 6°$. Assuming the target BER, $P_{e,T} = 10^{-8}$, for the receiver aperture diameter of $D = 2.5$ cm, the maximum acceptable water extinction coefficient is calculated as $c = 0.12\,\mathrm{m}^{-1}$. When we increase the receiver aperture diameter from $D = 2.5$ cm to $D = 5$ cm and $D = 7.5$ cm, the calculated extinction coefficients that the UVLC system can still work as $c = 0.26\,\mathrm{m}^{-1}$ and $c = 0.34\,\mathrm{m}^{-1}$, respectively. It is readily observed that as the receiver aperture increases, the UVLC system can continue operating with higher extinction coefficients. If we increase the extinction coefficient values more than the maximum limit value, the system will no longer work at the same BER performance.

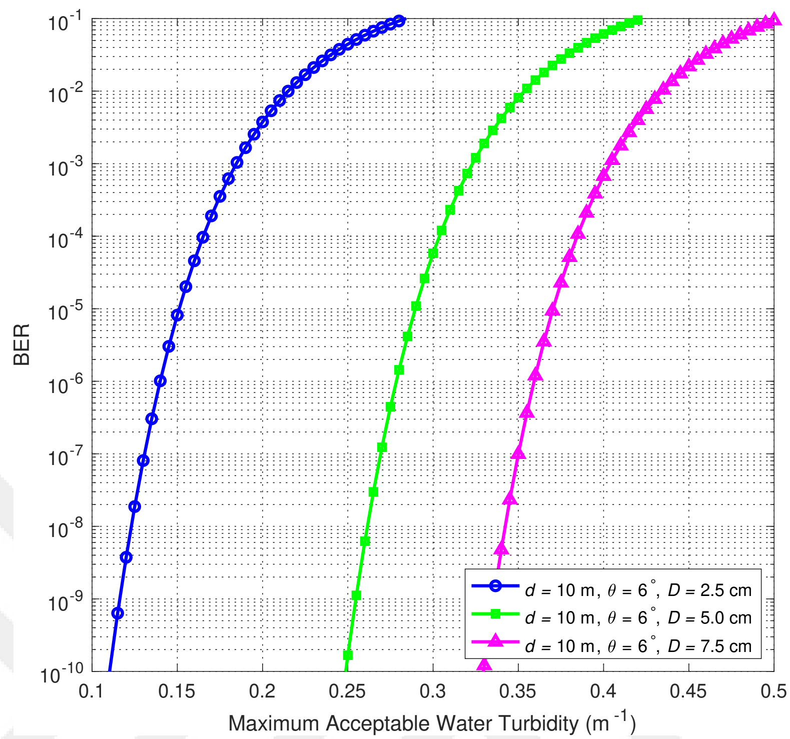

Figure 21: Maximum acceptable water turbidity based on aperture diameter (*D*).

So far, we have only examined semi-collimated UVLC channel models in the LOS direction. First, in Chapter 2, we introduced the experimental system for taking semi-collimated UVLC channel measurements. Then, as discussed in Chapter 3, we analyzed the performance limits of a semi-collimated UVLC channel model, which we experimentally verified. The following chapter aims to demonstrate mathematically and experimentally how much signal gain can be achieved by adding an NLOS path via a reflector.

CHAPTER IV

REFLECTOR-AIDED UVLC TRANSMISSION

4.1 Introduction

In the previous chapters, experimental and analytical studies were carried out with only LOS measurements in mind. However, regarding semi-collimated UVLC systems, NLOS UVLC systems do not have detailed research. Based on this issue, it is crucial to prove the signal gain we can obtain when we add an NLOS path to semi-collimated UVLC systems, both mathematically and experimentally.

Several studies have examined the feasibility of NLOS UVLC [92–96]. Based on ray-tracing simulations, a study in [92] has demonstrated that transmission can occur between two divers despite the absence of a LOS link. Experimental work in [93] and [94] has demonstrated that NLOS transmission can be enabled by energy scattered from suspended particles within the water between the transmitter cone and receiver cone. A simulation study conducted by Tang et al. [95] used the sea surface as a reflector for NLOS communication between two submerged nodes. According to El-Fikky et al. [95], the orientation angle of the transceiver affects the NLOS link gain. Although the above works demonstrate the feasibility of underwater non-line-of-sight transmission through simulations and experimental results, none provide a closed-form expression for path loss. Therefore, the NLOS UVLC path loss model is needed.

While the channel models for the NLOS transmission in the literature demonstrate the feasibility of underwater NLOS transmission through simulations and experimental results [92–96], none of them provides a closed-form expression for the path loss. In this chapter, we propose a closed-form expression for the underwater path loss under the assumption of NLOS transmission through the water surface and a man-made reflector (e.g., mirror) in addition to the LOS link. As a basis for deriving the reflected power, we assume a hypothetical photodetector that allows us to calculate it according to the geometry of light propagation. Afterward, combining the derived expression and the overall channel coefficient, we quantify the achievable NLOS gain. We finally validated the findings of our study through aquarium experiments.

The remainder of this chapter is organized as follows. First, in Section 4.2, we will introduce the system model. The next step will be to mathematically demonstrate the proposed NLOS channel model in Section 4.3. Subsequently, in Section 4.4, using both a mirror and the signal gain from the surface of the water, we will validate the proposed theoretical gain with the experimental measurements. Finally, we will discuss some of the practical aspects we have observed in our NLOS UVLC channel measurement studies in Section 4.5.

4.2 System Model

When light is emitted from its source, it is affected by the attenuation caused by absorption and scattering. Likewise, when the light is close to the surface of the water, as shown in Figure 22 on the following page, the light cannot cross the water/air boundary easily, and a considerable portion of the light will be reflected. Considering the rules denoting that both incident and reflected angles are always the same, an optical photon propagates along the beam divergence angle in a semi-collimated Gaussian UVLC measurement system. A reflecting surface will redirect a semi-collimated optical transmission in the same proportion that the reflecting surface redirects it.

An alternative approach to this problem is to consider it from another angle. In practical laser applications, the collimated output is presumed to propagate with a minimal beam divergence angle. At long distances, this is evident. We comfortably observe the spread of the beam in semi-collimated systems in a controlled manner depending on the optical circuitry we build. As the distance increases, however, the geometric loss in the optical signal will increase in direct proportion to the beam divergence. With the addition of a static reflecting surface, we can recapture the optical photons, which are considered lost if no reflecting surface is used. Under the assumption of a flat water surface, the receive beam includes both the direct and reflected beam, as seen in the Figure 22.

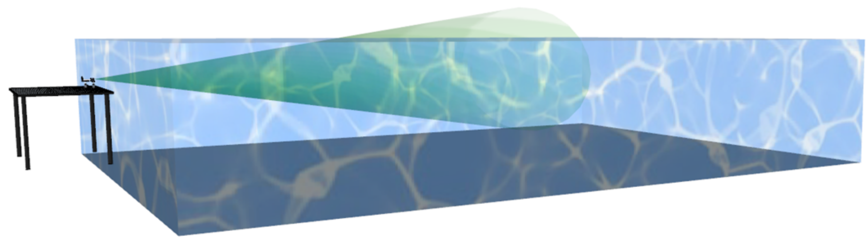

(a)

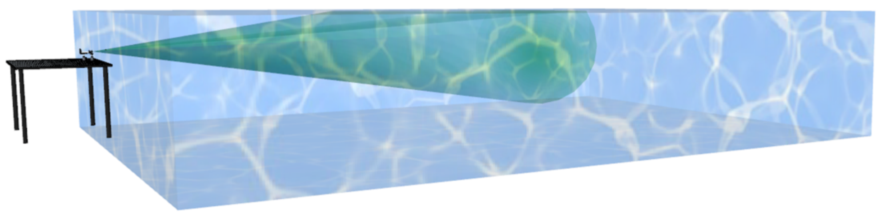

(b)

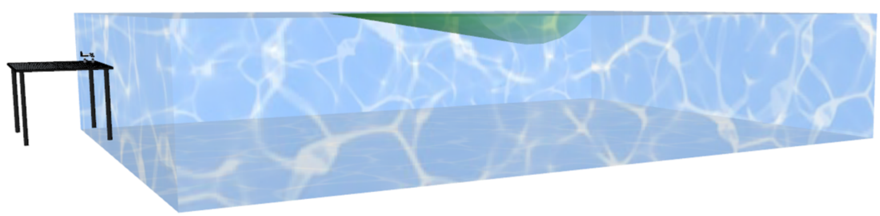

(c)

Figure 22: NLOS signal transmission via water surface(a) propagation of light close to reflecting surface (b) direct beam (c) reflected beam.

The detected beam in Figure 22, which represents the propagation of both LOS and NLOS paths, can be described as a summation of two detected beams Figure 23 on the next page. Here, we assume the exact location of the photodetector to collect the beam subject to geometric and attenuation losses. If we move the location of the photodetector to a place where the optical signal still exists, we will not read zero power. However, it detects less power than the center position. Suppose we assume the location where the optical signal still exists and the position where the photodetector is deployed as the hypothetical place. In that case, we can collect the same power level in the photodetector by reflecting this path.

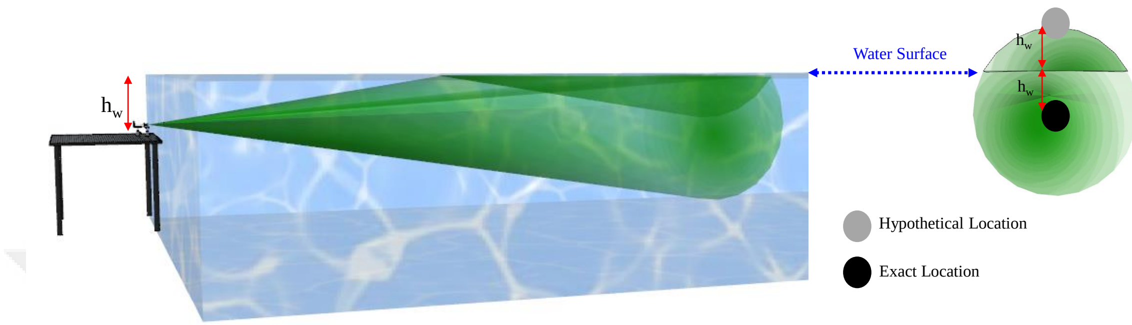

Figure 23: Exact and hypothetical locations of the photodetector.

Following the illustration shown in Figure 24 on the following page, suppose we have an underwater horizontal link that receives the sum of the direct and reflected signals. Mirrors or water surfaces can be used as reflectors to improve reception by using them as mirrors. For example, consider the case of a semi-collimated laser source whose beam shape is Gaussian and is semi-collimated. A lens with a diameter of D collects the optical signal along the LOS path. Attenuation and geometric loss will occur along the path of LOS. A reasonable approximation of the LOS channel coefficient can be found in the following equation, which assumes that the water is non-turbid

$$h_D \approx \underbrace{\left[1 - \exp\left(-2\frac{(D/2)^2}{\omega^2(d)}\right)\right]}_{h_G} \underbrace{\exp(-cd)}_{h_P} \cdot \tag{4.1}$$

Equation (4.1) consists of two terms, namely the channel coefficient due to the geometric loss (h_G) and the channel coefficient due to the path loss (h_P). Here, c is the extinction coefficient. Besides, $\omega(d)$ denotes the Gaussian beam half-width at a distance d from the laser source and is represented by

$$\omega(d) = d\tan(\theta/2) \cdot \tag{4.2}$$

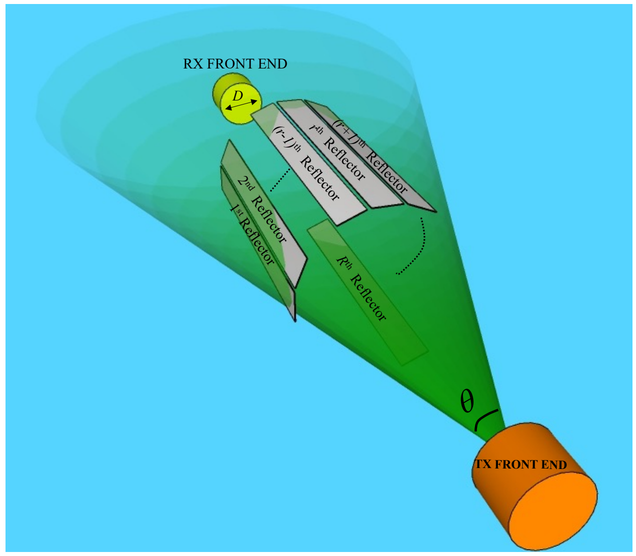

(a)

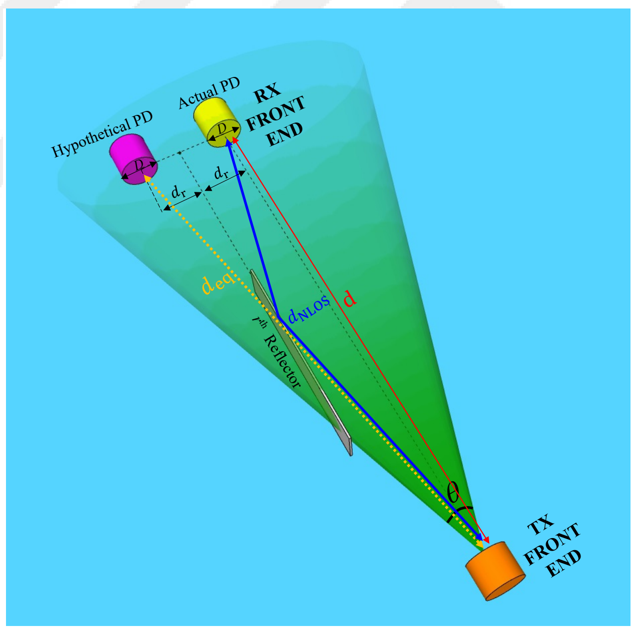

(b)

Figure 24: NLOS UVLC channel modeling (a) with multiple reflectors and (b) side view of the r^{th} reflector with related parameters.

4.3 Proposed NLOS Channel Model

As illustrated in Figure 24(a), we assume that R reflectors are used. In the case of the sea surface as a reflector, the r^{th} reflector in Figure 24 will represent the water surface (i.e., $R = 1$). Let d_r represent the distance between the reflecting surface and the transmitter for the lateral direction. This was accomplished by considering a hypothetical photodetector located at a distance away from the actual photodetector and aimed in the direction of the reflecting surface to model the reflected path. The propagation distance associated with NLOS (shown by d_{NLOS}) can be easily verified as being the same as the distance between the transmitter and hypothetical photodetector (shown by d_{eq}). A photodetector must be held at the center of the beam to detect the signal. Aside from that, it can also measure signals reflected upon a surface away from the center of the beam by measuring the distance $2d_r$ from the center of the beam to the boundary of the surface. Therefore, we can write the NLOS channel coefficient as

$$\begin{aligned} h_r = &\rho_r P_\circ \exp\left(-\frac{2(2d_r)^2}{\omega^2(d)\ \sqrt{\pi}\,\mathrm{erf}(\nu)/(2\nu\exp(-\nu^2))}\right) \\ &\times \exp\left(-c\underbrace{\sqrt{(2d_r)^2+d^2}}_{d_{\text{eq}}}\right), r = 1,2,\cdots,R, \end{aligned} \tag{4.3}$$

where ρ_r is the reflectance of the r^{th} reflecting surface, $\nu = \sqrt{\pi}\,(D/2)\Big/\left(\sqrt{2}\omega\right)$ and the fraction of the collected power for zero displacements of $d_r = 0$ is $P_\circ = [\mathrm{erf}(\nu)]^2$. Here, $\mathrm{erf}(\cdot)$ represents the error function. Utilizing Equation (4.1) on page 47 and Equation (4.3), the overall channel coefficient that incorporates both LOS and reflected paths is obtained as

$$\begin{aligned} h &= h_D + \sum_{r=1}^{R} h_r. \\ &= \left[1-\exp\left(-2\frac{(D/2)^2}{\omega^2(d)}\right)\right]\exp(-cd) \\ &\quad + \sum_{r=1}^{R}\rho_r P_\circ \exp\left(-\frac{8d_r^2}{\omega^2(d)\ \sqrt{\pi}\,\mathrm{erf}(\nu)/(2\nu\exp(-\nu^2))}\right) \\ &\quad \times \exp\left(-c\sqrt{(2d_r)^2+d^2}\right). \end{aligned} \tag{4.4}$$

Special Case 1: As a sanity check, assume that the reflector is placed far away from the detector (i.e., $d_r \to \infty$). Utilizing this within Equation (4.4) on the preceding page, the summation term becomes zero, indicating the reflected channel coefficient equals zero. Therefore, Equation (4.4) on the previous page reduces to Equation (4.1) on page 47, which is the channel coefficient for the case of LOS path.

Special Case 2: We now examine the maximum achievable channel coefficient associated with the reflection. The channel coefficient increases as d_r get smaller. The upper limit of the channel coefficient can be obtained assuming that the hypothetical photodetector is placed at the exact position of the actual photodetector (i.e., $d_r \to 0$). In this case, the first exponential term becomes one while the second exponential term in Equation (4.4) on the previous page reduces to $\exp(-c\,d)$. Therefore, Equation (4.4) on the preceding page takes the form of

$$\begin{aligned} h = & \left[1 - \exp\left(-2\frac{(D/2)^2}{\omega^2(d)}\right)\right]\exp(-cd) \\ & + P_\circ \exp(-c\,d) \sum_{r=1}^{R} \rho_r \cdot \end{aligned} \tag{4.5}$$

If we use the Taylor series expansion of error function around zero [97], we can write $P_\circ$ as

$$P_\circ = \left[\frac{2}{\sqrt{\pi}}\left(v - \frac{v^3}{3} + \frac{v^5}{10} - \frac{v^7}{42} + \cdots\right)\right]^2 \cdot \tag{4.6}$$

It can be readily confirmed from Equation (4.6) that for $v \ll 1$, $P_\circ$ can be approximated as $P_\circ \approx 4v^2/\pi$. If we solve it for v, we can write $v \approx \sqrt{\pi P_\circ}/2$. Equating this with the original definition of v, we can rewrite it as

$$v = \sqrt{\pi}\,(D/2)/\left(\sqrt{2}\,\omega(d)\right) \cdot \tag{4.7}$$

Then, the $\omega^2(d)$ is therefore written as

$$\omega^2(d) \approx D^2/(2P_\circ) \cdot \tag{4.8}$$

If we replace this within the geometric loss expression as shown in Equation (4.1) on page 47, we can write h_G as

$$h_G = 1 - \exp(-P_\circ) \cdot \tag{4.9}$$

Noting that $P_\circ$ is very small (e.g., in terms of milli or microwatt), we can use $\exp(x) \approx 1 + x$ [90] which yields $h_G \approx P_\circ$. Utilizing this, Equation (4.5) on the previous page can be approximated as

$$h \approx h_D \left(1 + \sum_{r=1}^{R} \rho_r\right) \cdot \tag{4.10}$$

As discussed above, the gain due to reflections is maximized as $d_r \to 0$. This implicitly assumes that the LOS link is not blocked. It can be readily checked that, to achieve maximum channel gain without affecting the LOS link, the lateral distance between the reflecting surface and transmitter should not be lower than $d_{r,\min} = D/2$. Let $G_{\max}$ denote the maximum achievable gain due to reflection. It is defined as the ratio between the maximum achievable channel coefficient from reflection ($h_{\max}$) and the overall channel coefficient (h_D). We can obtain $h_{\max}$ by simply replacing $d_{r,\min} = D/2$ in Equation (4.4) on page 49. Using the resulting expression, the maximum achievable gain due to reflection is obtained as

$$G_{\max} \approx 10\log_{10}\left(1 + \exp\left(-\frac{2D^2\left(2\nu\exp\left(-\nu^2\right)\right)}{\omega^2(d)\sqrt{\pi}\mathrm{erf}\left(\nu\right)}\right)\sum_{r=1}^{R}\rho_r\right) \cdot \tag{4.11}$$

For $d \to \infty$, Equation (4.11) reduces to

$$G_{\max} \approx 10\log_{10}\left(1 + \sum_{r=1}^{R} \rho_r\right) \cdot \tag{4.12}$$

If we assume reflectors with 100 % of reflectance, (i.e., $\rho_r = 1, r = 1, 2, \cdots, R$), the Equation (4.12) further simplifies to

$$G_{\max} \approx 10\log_{10}(1 + R) \cdot \tag{4.13}$$

4.4 Experimental Verification

In this section, we verify the proposed model through experimental verification. As seen in Figure 25, we conducted our experiments in an aquarium with $(1\,\text{m} \times 1\,\text{m} \times 8\,\text{m})$ dimensions. The source is placed outside the aquarium while the detector is placed inside an inner cuvette with a size of $(0.3\,\text{m} \times 0.3\,\text{m} \times 0.5\,\text{m})$ where the loss of the exterior glass is 17 % while the glass of the inner cuvette has a 10 % loss. The mirror was placed close to the transmit source.

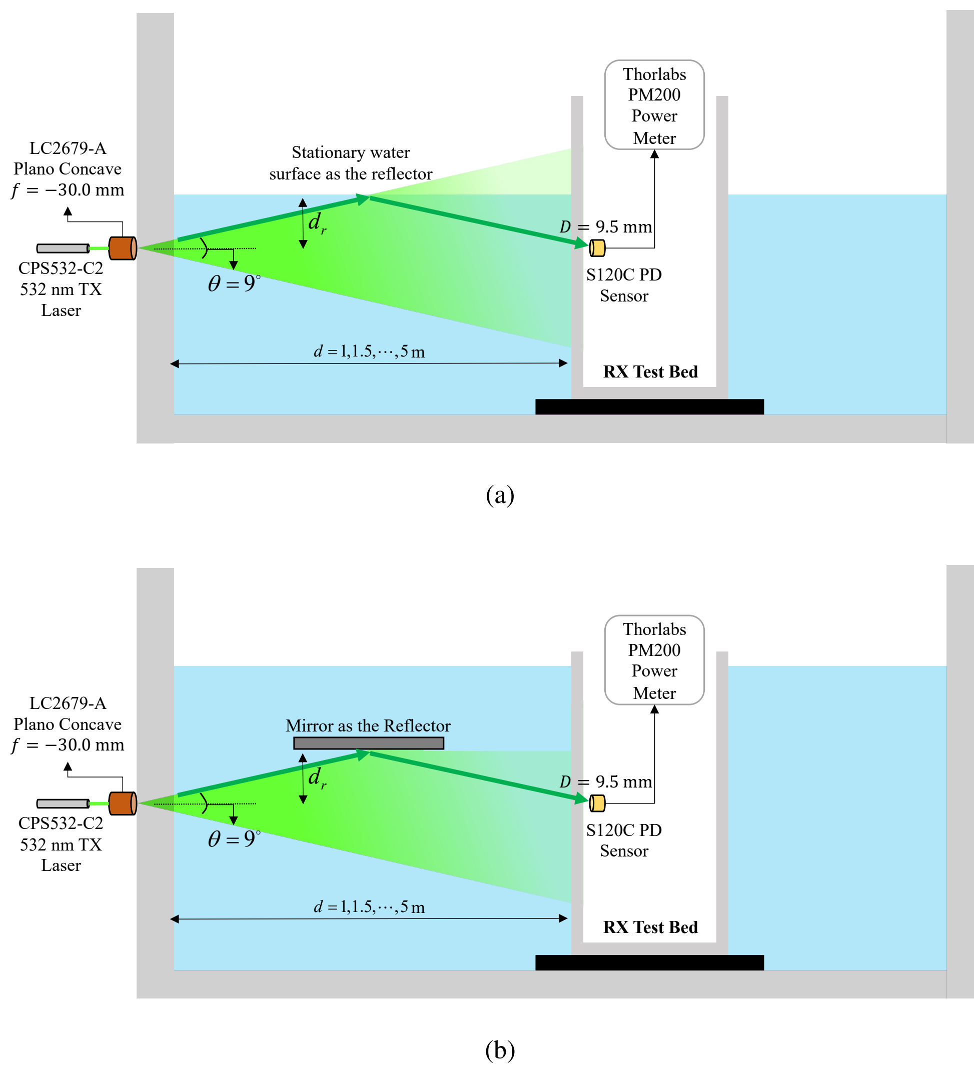

Figure 25: Experimental setup for NLOS reflection gain on the measured power ($R = 1$ is assumed) (a) reflection from the water surface (b) reflection from the mirror.

Hence, the whole beam is reflected from the side of the reflector. A sufficiently large reflector should be chosen based on the transmission distance, and the exact size should be determined accordingly. During the experiments, we used a mirror with the dimension of 0.2×0.7m, which was sufficient for a 5m distance. Unless stated otherwise, we utilized the Thorlabs CPS532-C2 532 nm green laser as the laser diode. To end up with a semi-collimated optical signal with $\theta = 9^{\circ}$, we placed an LC2679-A plano-concave lens with a focal length of $f = -30\,\mathrm{mm}$ in front of the laser source. We measured the received optical signal power with a Thorlabs PM200 power meter with an S120C PD sensor, which has an aperture diameter of 9.5 mm. The extinction coefficient in the aquarium was measured as $0.13\,\mathrm{m}^{-1}$.

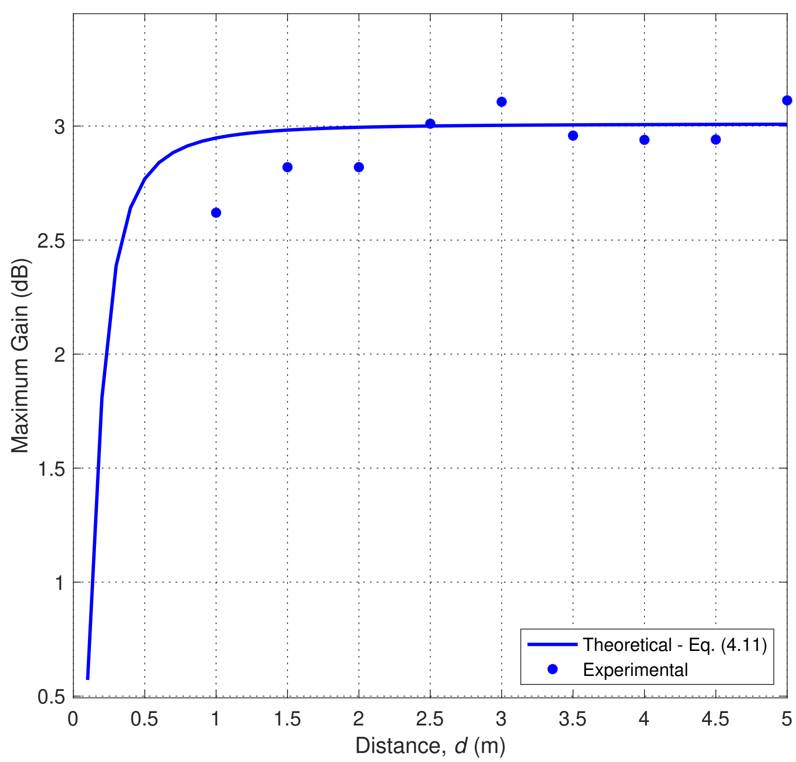

Figure 26: Water surface as the reflecting surface experiments.

Both in Figure 26 and Figure 27 on the next page, we present our experimental results along with the theoretically achievable gain calculated from Equation (4.11) on page 51 and indicated by solid lines. In our experiments, we considered two types of reflectors, namely a water surface (Figure 26 on the previous page) and a mirror (Figure 27). In the first case, the reflector is the whole water surface, and we have no control over its size or orientation, as seen in Figure 26 on the previous page. For the case of the mirror, we placed the mirror perpendicular to the water surface and submerged it inside the waterFigure 27. We then change the orientation angles of the mirror (yaw, pitch, azimuth angles) until we receive the maximum power and record it. We performed our experiments at propagation distances from 1 m to 5 m with a step of 0.5 m.

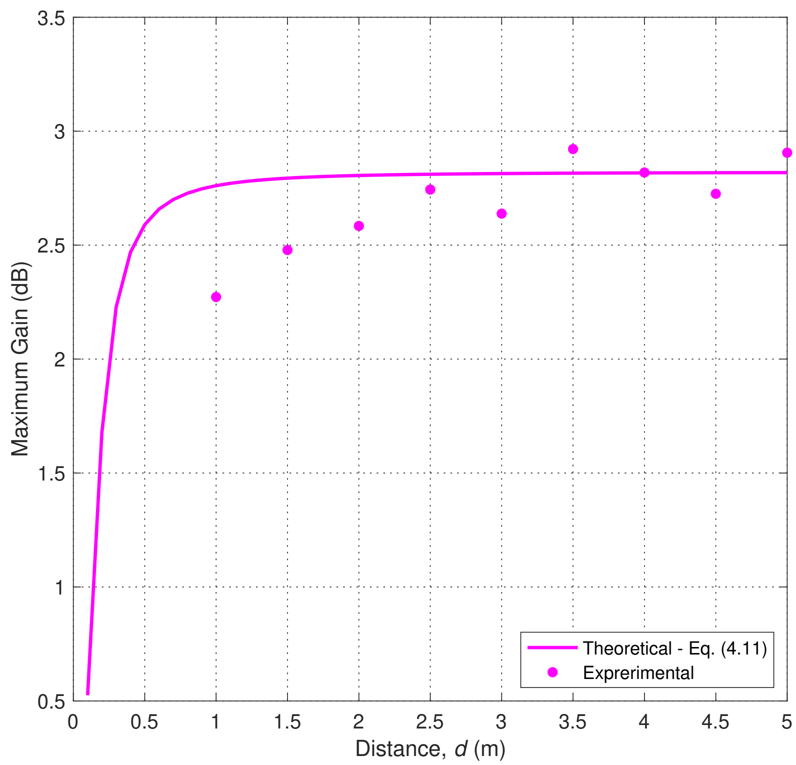

Figure 27: mirror as the reflecting surface experiments.

Comparison of results in Figure 26 on the previous page and Figure 27 reveal that water surface yields better results as a reflector. The reflectance of the mirror used in our experiments was measured as $(\rho_r = 0.917)$. The theoretical calculation was made assuming that reflectance of the water surface is as $(\rho_r = 1)$. It should be noted that when the light falls on the surface of the water at an angle more significant than 90°, so-called total internal reflection occurs where the light that hits the water's surface will be bounced entirely off rather than passing through. Since the link distance is much larger than the lateral shift, the angle is always more prominent than the incident angle. The predicted theoretical gain values for the water surface and the mirror are 2.947 dB and 2.761 dB, respectively, for $d = 1$ m. It is also observed that after a certain distance, the performance is saturated, and the maximum gain converges to $G_{\max}$ =3.007 and 2.818 dB. A gain of 3 dB indicates that the received power is doubled. This is expected since, for a semi-collimated Gaussian beam shape, the beam half-width is much larger than the photodetector radius, and the intensity around the center does not change much. Since the lateral distance d_r is small (See Figure 24(b) on page 48), the reflected signal can be received by the photodetector in almost a similar amount to what the LOS path is received. In particular, it can be checked that the propagation distance in NLOS transmission (d_{NLOS}) and the propagation distance in LOS transmission (d) are almost the same assuming $d_r \ll d$. In summary, under the assumption of ideal reflection and the link distance is large enough (i.e., $d_r \ll d$), the gain reaches around 3 dB.

Both Figure 26 on page 53 and Figure 27 on the previous page further demonstrate that experimental results match analytical results, particularly for distances above 2.5 m. For example, consider $d = 2.5$ m. The LOS power at $d = 2.5$ m (i.e., without any reflector) was measured as 8.4 μW. If the water surface is used as the reflecting surface, the total optical power is increased to 16.8 μW, which indicates a gain of $10\log_{10}(16.8/8.4)$ = 3.01 dB. Similarly, when the mirror is used as the reflector, the total optical power is measured as 15.8 μW, which indicates a gain of $10\log_{10}(15.8/8.4)$ = 2.74 dB. It can be confirmed from Equation (4.11) on page 51 that the estimated theoretical gains from the water surface and the mirrors are 3 dB and 2.81 dB, respectively. The mismatch between analytical and experimental results can be quantified by the Mean Squared Error (MSE). The MSE of the experimental results are calculated as 0.02 for the water surface and 0.05 for the mirror. The MSE drops below 0.05 for $d \geq 2$ m.

In some cases, there are gain values close to or even more than 3 dB in the experiment and simulation, which may mean that the hypothetical PD in Figure 24(a) on page 48 receives more power than the actual PD that is aligned with the beam. However, the intensity can be considered uniform around the photodetector. In our case, since the lateral distance d_r is small (See Figure 24(a) on page 48), the reflected signal can be received by the photodetector in almost a similar amount to what the LOS path is received. In particular, it can be checked that the propagation distance in NLOS transmission ($d_{\text{NLOS}} = d_{\text{eq}}$) and the propagation distance in LOS transmission (i.e., d) are almost the same assuming $d \gg d_r$. In summary, under the assumption of perfect reflection and $d \gg d_r$, the received power is doubled, i.e., the gain reaches up to around $10\log_{10}(2) = 3.01\,\text{dB}$. Of course, due to imperfections and deviations from ideal conditions, there might be fluctuations in the experimental results. Nevertheless, our measurements are within $\pm 0.25\,\text{dB}$ from both LOS and NLOS measurements provided with the water surface and the mirror.

4.5 Experimental Aspects

In the Section 4.3 on page 48, we calculated theoretically the upper bound on the achievable gain. This implicitly assumes that the reflector can be placed at a distance $d_r = 0$ from the source-detector link, which assumes that the source is a point source, the detector is a point detector, and the lenses have zero diameters. Experimentally, this is not achievable. We discuss the experimental limiting factors and experimentally achievable gains as follows.

4.5.1 Aperture Size

To study the most significant channel coefficient due to the use of reflectors in Equation (4.11) on page 51, we consider that the distance of all the reflectors from the center of the beam equals zero (i.e., $d_r \to 0,\ r = 1, 2, \cdots, R$). This neglects that the detector can be blocked (See Figure 24 on page 48). The minimum distance before blocking the detector (i.e., without affecting the main path) can be found as $d_{r,\min} = D/2$ as given in Equation (4.11) on page 51. As d_r gets smaller (i.e., $d_r \to 0$), the amount of gain available from one reflector is maximized. The gain can be maximized by keeping the reflector as close to the source as possible. Hence the expected gain can be maximized. In practice, the reflector may be positioned a few centimeters from the main path of the signal, resulting in a loss of signal during deployment. This should be done to ensure that the reflector(s) are positioned in the system in precise alignment when they are placed there.

4.5.2 Lens Effect

In practice, lenses are used to collimate the beam on the detection area of the photodetector. While the single lens may be suitable for the received rays from a specific direction, there may be better options for focusing the received beam from another direction. The wider the angle of incidence, the greater the distance between the point of focus and the detector. One would expect the problem to occur more often at short distances than long distances. A trade-off between the gains and losses will occur when using several lens combinations to focus direct and reflected beams at different distances. To prevent the loss of reflected optical rays, the PD sensor is primarily used to collect the received power; a lens has been omitted from the detector assembly to prevent any loss of reflected optical rays.

Aside from that, most commercially available PD sensors are not uniformly sensitive across the entire detection range of the sensor. Therefore, it is likely that the reflected rays will not be focused in a way where that can be detected by the PD sensor since the reflected rays will not be focused there. Therefore, to check the receiving lens as one of the experimental aspects to be observed, we have placed a Thorlabs LB-1309-B with $D = 50.4\,\text{mm}$ with the focal length of $f = 75\,\text{mm}$ as the receiving lens at the receiver by using the same transmitter circuitry and the same reflector which have been already used in Section 4.4.

Furthermore, we have placed both transmitter and optical receiver circuitry at the short edges of our aquarium with $(1\,\text{m} \times 1\,\text{m} \times 8\,\text{m})$ dimensions. To determine the effect of the LOS signal at 1 m distance, we measured the signal using the Figure 28(a) as being 0.87 mW. Upon receiving the optical signal, it is essential to note that the receiving lens collimates this signal with the PD sensor in a perfect alignment. We then measured the optical power by collimating both LOS and NLOS optical signals onto the PD sensor as observed in the Figure 28(b) by adding one mirror as the reflector from the side of the beam, which resulted in a value of 1.06 mW.

(a)

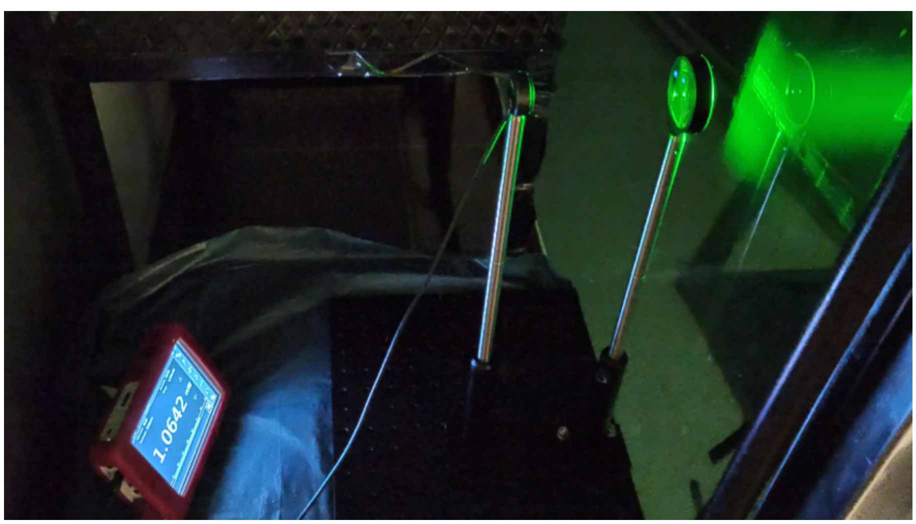

(b)

Figure 28: 1 m NLOS power measurements (a) no mirror and (b) with one mirror.

Our final measurement results showed that through LOS and LOS with NLOS, we achieved $G_{\max} = 10\log_{10}(1.06/0.87) = 0.86$ dB gain thanks to the reflector. Despite this, $G_{\max}$ is the maximum theoretical gain that can be achieved by using the same system parameters shown in Section 4.4 as 1.91 dB based on just a short distance from the system, and this is caused by the fact that all reflections cannot be collimated within such a short amount of time. We observe the deviation of the accuracy of the experimental gain measurements compared to the theoretical value based on Equation (4.11) on page 51.

4.5.3 Reflector Placement

The beam waist of semi-collimated optical signals gets more prominent as the distance increases. Therefore, a reflecting surface can change the beam direction from any side of this beam waist. So, to collect both LOS and NLOS signals together, a reflector placed anywhere on the beam waist can be collected at the PD sensor with a good alignment. So, it is possible to position the reflectors from various orientations using the test setup we have created. An illustration of this can be found in Figure 24(a) on page 48. Besides, reflective surfaces can be constructed between end-to-end optical receivers and optical transmitters at any angle. As shown in Figure 29 on the next page, reflectors can be placed in different positions to contribute to the propagation of semi-collimated optical signals.

The most crucial point here is that the reflected signals can be collected on the receiver after reflecting semi-collimated optical signals with any surface. Therefore, we positioned the reflector in our test setup at different angles to see how it affected the results. We ensured that both LOS signals were collected in the receiving lens and then focused on the PD sensor in each measurement. In addition, we have confirmed that the optical signals from the reflected surface are collected in the receiving lens and collected at a second focal point, again on the PD sensor.

Figure 29: Different reflection locations.

After obtaining the LOS measurement in Figure 30 on the following page, we got the measurements in four other directions. Our ideal scenario is to obtain the same maximum power gain in all four orientations. Despite this, some discrepancies are observed between these measurements. The main reason for this could be attributed to the fact that the optical receiver circuit uses a 50.4 mm lens to focus the photons pointwise, which falls on an area with different sensitivity when it comes to the power detector. Based on these measurements, we obtained the LOS measurement in Figure 30 by positioning the reflector at four locations in four different directions: the right side (Figure 30(a)), the bottom (Figure 30(b)), the top (Figure 30(c)), and diagonally (Figure 30(d)).

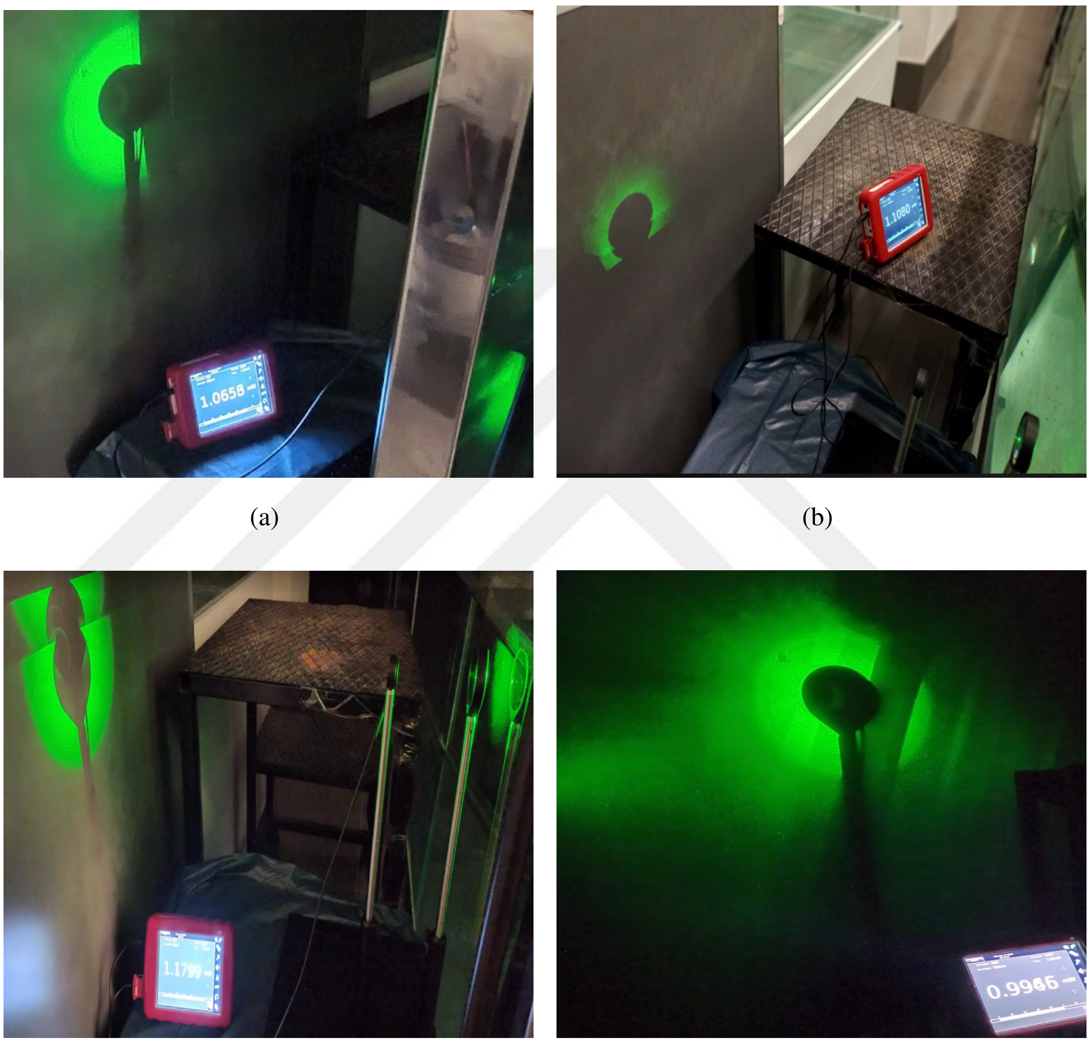

(a) (b) (c) (d)

Figure 30: Reflection measurements from different orientations of a reflector at (a) right side (b) bottom (c) top and (d) diagonal.

To further test the effect of multiple reflectors on power gain, we designed a test setup to observe the effect of multiple reflectors in addition to those already mentioned above. Using the same setup, we placed reflectors on both sides of the optical signal to observe the effect of multiple reflectors on power gain. The maximum measurement of 1.325 mW (meaning $G_{max} = 1.82\,\text{dB}$) was achieved after correctly aligning both reflectors to the PD sensor so that the PD sensor captured the reflected photons from both reflectors. However, the maximum achievable theoretical gain value based on the two reflectors should have been higher than recorded. This is mainly caused by the short distance alignment difficulty and using a lens that collimates both LOS and NLOS beams into the PD sensor.

4.5.4 Reflector Distance

We discussed in detail in Section 4.3 on page 48 that the closer the reflective surface is to the semi-collimated beam, the greater the gain. In addition, we have shown that our measurement accuracy at short distances is not very successful compared to the theoretical gain values due to the difficulty of focusing the reflective surface on the optical sensor in a controlled manner.

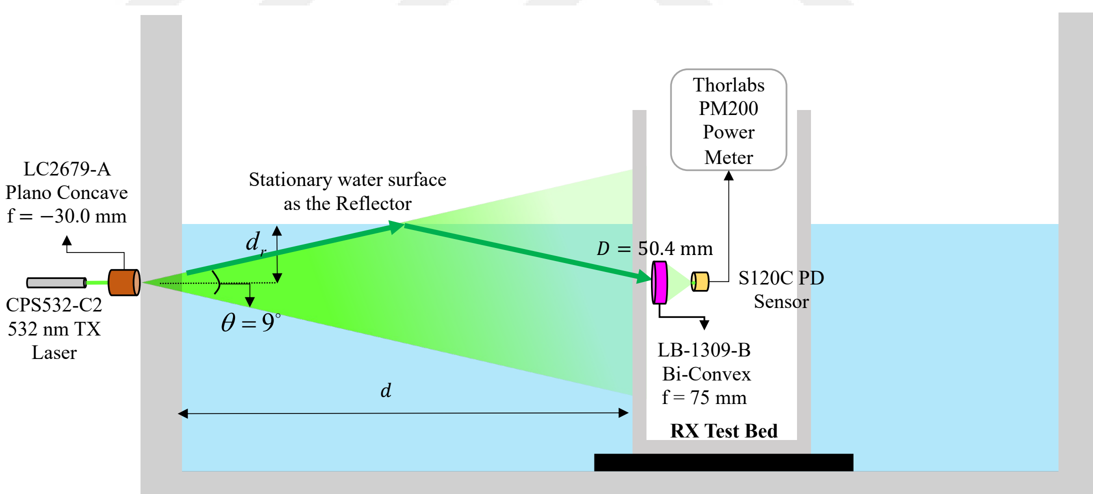

Figure 31: reflection from the water surface experimental setup.

To confirm that the water surface acts as an excellent reflector as the distance increases, we conducted experiments at 2 m and 3 m using the same receiver lens. We encountered an alignment problem when using a man-made reflector, but when the reflective surface was turned into standing water, the alignment problem was resolved. So, we carried out three tests on the same test system for two different days, considering two different conditions on the same test system. This experiment was conducted to shed light on two distinct issues that needed to be addressed. It is first necessary to investigate whether the extinction coefficient impacts the gain value of the measurement as a result of measuring it. Secondly, we are also investigating the effect of the water surface on the maximum gain of transmission over two different transmission distances.

For all these 3 experiments, we have prepared a test system as depicted in Figure 31 on the previous page by increasing the water level 19 cm above the laser and the detector. During these experiments, when starting to decrease the water level starting from the $d_\mathrm{r} = 19 \rightarrow 1\,\mathrm{cm}$, we recorded the measured power at the PD sensor. For the first and the second experiments, we provided them within the same day with the extinction coefficient as $c = 0.41\,\mathrm{m}^{-1}$. The first experiment ($d = 3\,\mathrm{m}, c = 0.41\,\mathrm{m}^{-1}$), the power gain is measured 2.78 dB. For the second experiment ($d = 2\,\mathrm{m}, c = 0.41\,\mathrm{m}^{-1}$), the achieved power gain is recorded as 1.88 dB as given in Figure 32.

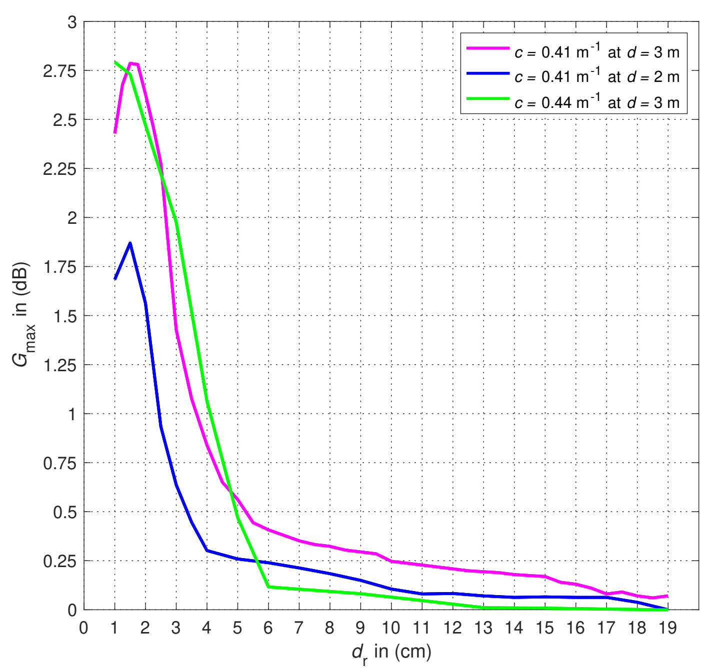

Figure 32: Water surface as the reflector.

Even though a good accuracy has been recorded within the experiment without any receiver lens (See Figure 26 on page 53), the experiments that include the receiving lens to collect the optical photons do not have adequate accuracy alongside the test results. As explained in detail in the Section 4.5.2, using a receiver lens to focus the optical photons onto the PD sensor requires perfect alignment.

In the previous chapters, we examined end-to-end semi-collimated LOS and NLOS systems in theoretical and experimental studies. Within the scope of LOS measurements, we not only achieved sufficient accuracy with the theoretical model by introducing our experimental working environment as demonstrated in Chapter 2 but also analyzed the channel coefficients of both collimated and semi-collimated LOS systems analytically. The experimentally verified UVLC optical channel models were chosen as the baseline channel model for the Chapter 3. In Chapter 3, we examined the maximum acceptable limits of different system parameters of semi-collimated UVLC systems.

Here in this chapter, we experimentally and mathematically proved that by adding an NLOS reflector concept to our experimental environment, we could increase the power of semi-collimated LOS signals in direct proportion to the number of reflectors. Up to this point, we had examined our measurement models, disregarding real-life practical use cases. However, in a real underwater application, how any semi-collimated system will perform in a real underwater environmental scenario depends on external factors (such as solar energy and chlorophyll concentration). Therefore, in the next chapter, we will try to find an optimum solution, considering external factors.

CHAPTER V

OPTIMIZATION OF UVLC SYSTEM PARAMETERS

5.1 Introduction

In Chapter 2, we experimentally examined the LOS semi-collimated UVLC system. Then, in Chapter 3, we demonstrated the performance metrics of a semi-collimated UVLC system in closed form analytical model. Here in this chapter, we will reveal the performance of a semi-collimated UVLC system in the presence of external factors which deteriorates the optical system performance underwater.

After analyzing the end-to-end behavior of semi-collimated UVLC systems in a laboratory environment mathematically and experimentally, we can now review their behavior in an oceanic environment. We assume that there is a vertical communication link under the sea or ocean for this purpose. Our concept is based on the idea that the receiver sensor can function both as an energy-harvesting panel and a lens that can collect optical signals according to this concept. Regarding energy harvesting, this receiver lens will store solar energy during certain hours of the day. Nevertheless, solar energy harvested from the sun will result in degrading the quality of optical communications links. Therefore, keeping the link performance optimal and harvesting energy is an essential function of the proposed system setup. Consequently, we suggest optimization strategies for the system for better performance of the communication link (i.e., SNR).

Following is an outline of the remainder of this chapter. First, the Section 5.2 reveals the system model for delivering the underwater link that can affect by the sun and the relevant extinction coefficients. Then, solar noise is calculated in Section 5.3 based on the different tilt angles. Next, the SNR is calculated by bringing all system parameters together in Section 5.4. Finally, in Section 5.5, we propose optimization algorithms for the considered system to maximize the SNR values depending on several locations and days concerning the hour of the day.

5.2 System Model

This study aims to investigate the sun's influence on the SNR of a Visible Light Communication (VLC) system operating underwater. For example, suppose a vertical UVLC system operates under the ocean or sea. This system model can be seen in Figure 33 as a representation of the system. We can build this model by assuming the following definitions as follows.

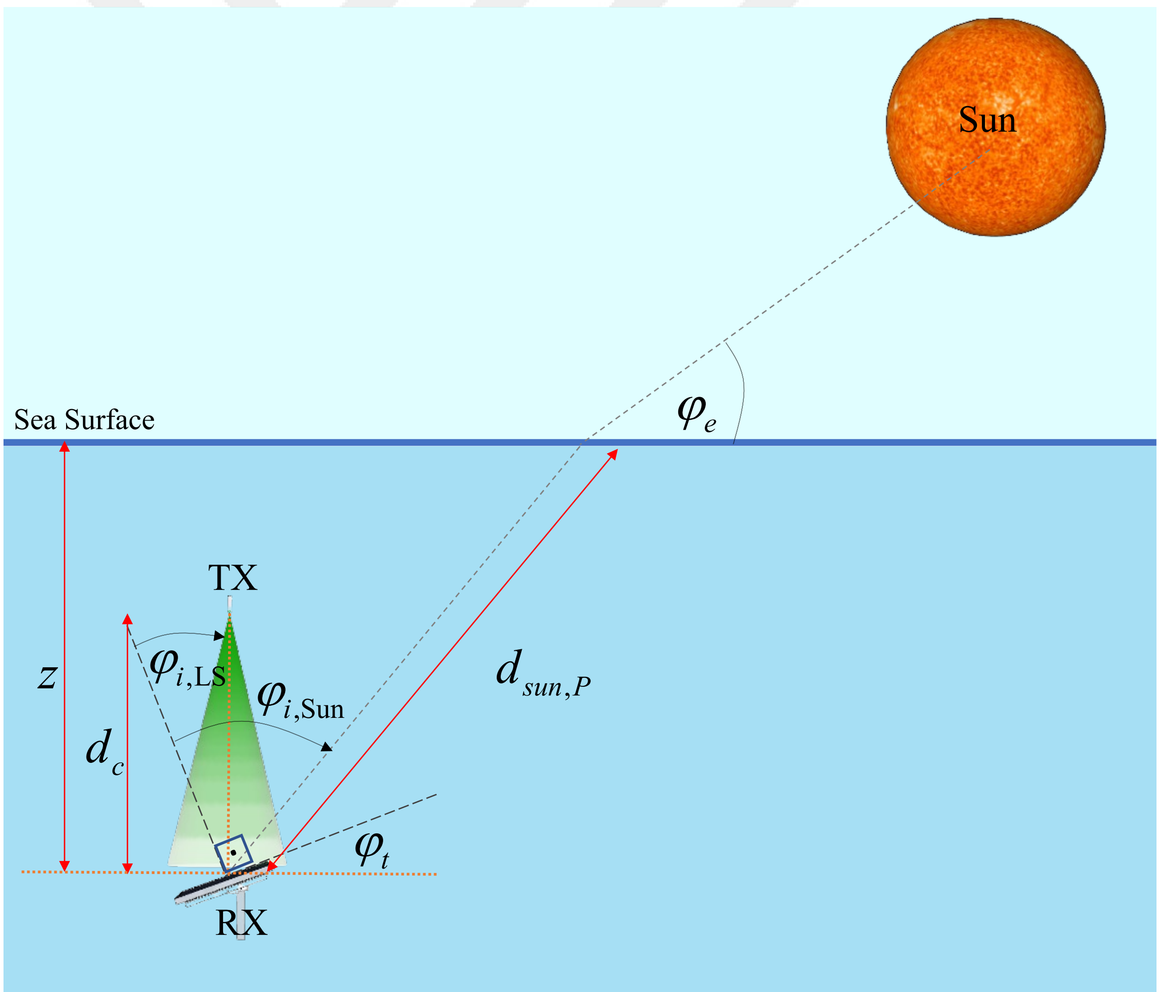

Figure 33: UVLC system model in the presence of the sun.

φ_e represents the sun's elevation angle. Next, $\varphi_{i,\text{sun}}$ represents the sun's incident angle to the detection area of the photodetector. $\varphi_{i,\text{LS}}$ represents the incident angle of the laser source considered, and φ_t represents the tilt angle of the photodetector. $d_{sun,P}$ depicts the propagation distance of the sunlight underwater. d_c is used to reveal the propagation distance for the intended signal (i.e., communication link distance). Also, the transmitter sends a Gaussian semi-collimated signal with θ beam divergence angle. Furthermore, z represents the depth of the photodetector. Following Figure 33 on the previous page, the sun's incident angle is as given by

$$\varphi_{i,\text{Sun}} = \pi/2 - \varphi_e + \varphi_{i,\text{LS}}. \tag{5.1}$$

5.2.1 Received Power from the Laser Source

Assume a photodetector has an area of A_s. This can be approximated as a circular detector with an aperture diameter of $D = 2\sqrt{A_s/\pi}$.

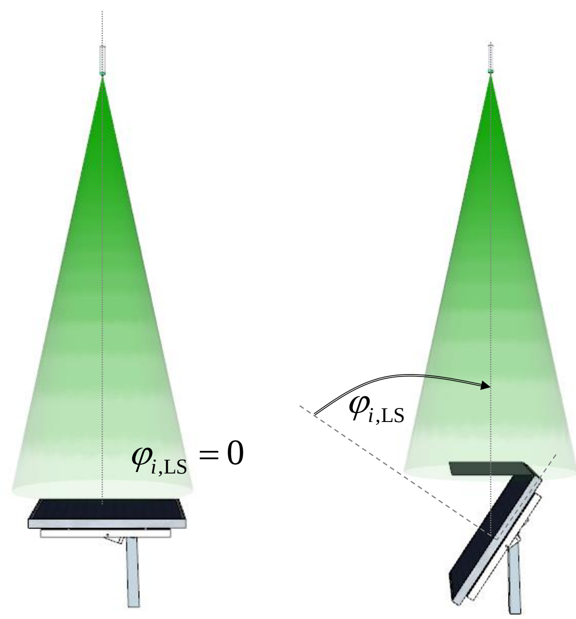

Figure 34: System model based on different tilt angles (a) $\varphi_{i,\text{LS}} = 0$ and (b) $\varphi_{i,\text{LS}} \neq 0$.

The received electrical power assuming the incident angle is zero can be written as [20]

$$\begin{aligned} P_R &= P_T \left[\underbrace{\left(\frac{D}{\theta \, d_c} \right)^2 \exp\left(-c\left(\lambda\right)\, d_c\right)}_{h} \right]^2 \\ &= P_T \left(\frac{16 A_s^2}{\pi^2 \theta^4 d_c^4} \right) \exp\left(-2c\left(\lambda\right)\, d_c\right), \end{aligned} \tag{5.2}$$

where h is the underwater path loss channel coefficients, P_T is the transmit electrical power, θ is the beam divergence angle, c is the extinction coefficient, and λ is the wavelength. Under the presence of an incident angle of $\varphi_{i,\mathrm{LS}}$, the effective area for the communication link can be written as (See Figure 34 on the preceding page)

$$A_{eff,LS} = A_s \cos\left(\varphi_{i,\mathrm{LS}}\right) \cdot \tag{5.3}$$

Utilizing Equation (5.2) and let η_g denote the general efficiency of the PD solar panel, the received electrical power in Equation (5.1) on the preceding page can be written as

$$\begin{aligned} P_R =& \frac{16 P_T \eta_g A_s^2 \cos^2\left(\varphi_{i,\mathrm{LS}}\right)}{\pi^2 \theta^4 d_c^4} \exp\left(-2c\left(\lambda\right)\, d_c\right) \\ =& \frac{16 P_T \eta_g A_s^2 \left(1 - \cos\left(2\varphi_{i,\mathrm{LS}}\right)\right)}{\pi^2 \theta^4 d_c^4} \exp\left(-2c\left(\lambda\right)\, d_c\right) \cdot \end{aligned} \tag{5.4}$$

5.2.2 Extinction Coefficient based on the depth

The extinction coefficient, c, is calculated based on Gordon's model (Chapter 3 in [98]). In c, absorption coefficient, a, (Equation 3.27 in [98]) given by

$$\begin{aligned} a =& \left(a_w + 0.06 \, a_c^* C^{0.65} \right) \\ & \times \left(1 + 0.2 \exp\left(-0.014\left(\lambda - 440\right)\right)\right), \end{aligned} \tag{5.5}$$

and scattering coefficient, b, (Equation 3.40 in [98]) written by

$$b = \left(550/\lambda\ \right) 0.3 \, C^{0.62} \cdot \tag{5.6}$$

C in both Equation (5.5) and Equation (5.6) represents the water concentration value, which changes based on the type of water. In Equation (5.5), a_w is the absorption coefficient of pure water, and a_c^* is a non-dimensional, statistically derived chlorophyll-specific absorption coefficient. Both a_w and a_c^* are given in (Table 3.7 in [98]). According to the discussion in [98], we used concentrations of pure seawater, clear ocean water, and coastal water as the most commonly selected values for the discussed model. With the use of the equation of $c = a + b$, where a is the absorption coefficient, and b is the scattering coefficient, curve fitting parameters can be applied to the reported measurement values for different types of water whose concentration values are different when the reported measurement values are based on $c = a + b$. Therefore, c can be written as

$$
\begin{aligned}
c = &\left(a_w + 0.06 a_c^* C^{0.65}\right)\left(1 + 0.2\exp\left(-0.014\left(\lambda - 440\right)\right)\right) \\
&+ \left(550/\lambda\right) 0.3 C^{0.62}.
\end{aligned} \tag{5.7}
$$

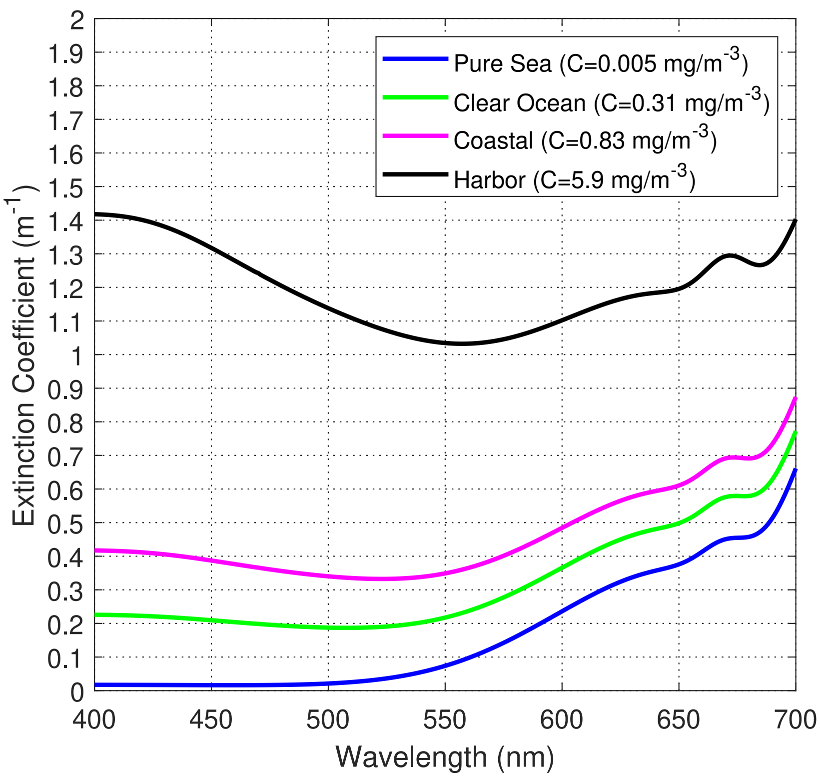

Figure 35: Extinction coefficient under different concentrations of water.

In our evaluations, we used the Matlab Curve Fitting Toolbox to calculate extinction coefficients concerning a set of variables (e.g., λ) using one variable as a reference. The variables a_w and a_c^* are estimated by the curve fitting tool models as given by Equation (5.8) and Equation (5.9)

$$\begin{aligned} a_w =& 0.8034\exp\left(-\left(\frac{\lambda-725.1}{30.69}\right)^2\right) \\ &+0.07392\exp\left(-\left(\frac{\lambda-670.1}{14.3}\right)^2\right) \\ &+0.3498\exp\left(-\left(\frac{\lambda-652}{76.57}\right)^2\right), \end{aligned} \tag{5.8}$$

$$\begin{aligned} a_c^* =& 0.6195\exp\left(-\left(\frac{\lambda-487.2}{75.43}\right)^2\right) \\ &+0.01381\exp\left(-\left(\frac{\lambda-470.1}{0.108}\right)^2\right) \\ &+0.6376\exp\left(-\left(\frac{\lambda-422.2}{51.64}\right)^2\right) \\ &+0.3221\exp\left(-\left(\frac{\lambda-653.1}{74.01}\right)^2\right) \\ &+0.2919\exp\left(-\left(\frac{\lambda-672.9}{14.13}\right)^2\right). \end{aligned} \tag{5.9}$$

In Figure 35 on the preceding page, the extinction coefficient based on different water types and wavelengths can be given.

5.3 Sun Power

It can be readily confirmed from Figure 33 on page 66 that the incident angle of the considered laser source ($\varphi_{i,\mathrm{LS}}$) and the tilt angle of the photodetector (φ_t) are the same (i.e., $\varphi_t = \varphi_{i,\mathrm{LS}}$). We can write the sun power received by the photodetector (i.e., sun noise) as

$$\sigma_S^2 = A_s \eta_g G_{\mathrm{water}} \exp\left(-zc\left(\lambda\right)\right), \tag{5.10}$$

where η_g represents the responsivity of the photodetector, and A_s is the surface area of the photodetector.

5.3.1 Underwater Light Intensity Calculation

In Equation (5.11), G_{water} is the light intensity right after passing through the water and is given by

$$G_{\text{water}} = (1 - \Upsilon_{\text{tot}})\, G_{\text{air}}, \tag{5.11}$$

where Υ_{tot} is the overall reflection of the direct solar irradiance from the ocean surface [99]. The distance between the water surface and the photodetector shall be considered z, which is used to calculate the solar noise. Assuming that the light is unpolarized and the water surface is flat, it can be calculated as the average of the reflectivity of the s-polarized and p-polarized light

$$\Upsilon_{\text{tot}} = 0.5 \left(\Upsilon_{\text{s}} + \Upsilon_{\text{p}}\right), \tag{5.12}$$

where Υ_{s} and Υ_{p} are respectively, given by

$$\Upsilon_s = \left[\frac{n_1 \sin(\varphi_e) - n_2\, g}{n_1 \sin(\varphi_e) + n_2\, g}\right]^2, \tag{5.13}$$

$$\Upsilon_p = \left[\frac{n_1\, g - n_2 \sin(\varphi_e)}{n_1\, g + n_2 \sin(\varphi_e)}\right]^2. \tag{5.14}$$

In the Equation (5.14), g can be written as

$$g = \sqrt{1 - [(n_1/n_2)\cos(\varphi_e)]^2}, \tag{5.15}$$

where n_1 and n_2 are the indexes of refraction for air and water, respectively. φ_e is the elevation angle of the sun, and it is dependent on the latitude of the location of interest, day of the year, and hour of the day. In Equation (5.11), G_{air} is the intensity of the sun right before entering the water and is given by

$$G_{\text{air}} = G_{\text{mi}}\, \rho\, \cos(\varphi_e)\,. \tag{5.16}$$

In Equation (5.16), G_{mi} is the maximum instantaneous radiation intensity at the time when the solar elevation angle is maximum (i.e., at $t_{\max}$) and is given by

$$G_{\mathrm{mi}} = G_{\mathrm{sc}}\rho\left(1+0.033\cos\left(\frac{360d}{365}\right)\right) \times \left(\sin\left(\varphi_{e_{\max}}+\delta\right)\cos\left(\delta\right)-\cos\left(\varphi_{e_{\max}}+\delta\right)\sin\left(\delta\right)\right), \tag{5.17}$$

where d is the specific day of the year and ρ is the atmospheric transmittance. In Equation (5.17), δ is the solar declination angle and is given by

$$\delta = 23.45\,\sin\left(\frac{360}{365}\left(248+d\right)\right)\cdot \tag{5.18}$$

5.3.2 Elevation Angle Calculation

In general, the elevation angle is related to time of the day. Let τ denote the daylight duration in hours which is given as [99]

$$\tau = 24\left(1-\frac{1}{\pi}\cos^{-1}\left(\tan\left(L\right)\right)\times\left(\frac{\sin\left(\varepsilon\right)\sin\left(\varpi\right)}{\sqrt{1-\sin^{2}\left(\varepsilon\right)\sin^{2}\left(\varpi\right)}}\right)\right), \tag{5.19}$$

where ϖ is the azimuthal angle of the sun and is calculated as

$$\varpi = -1.3411+M+0.0334\sin\left(M\right)+0.0003\sin\left(2M\right)\cdot \tag{5.20}$$

M in Equation (5.20) is the mean anomaly and is calculated as a function of day

$$M = -0.041+0.017202\,d\cdot \tag{5.21}$$

In Equation (5.19), ε is known as axial tilt [100] and is equal to $\varepsilon = 23.44°$. Based on the daylight duration provided in Equation (5.19), we can calculate the sunrise time (h_{sunrise}), and sunset time (h_{sunset}) as followed by

$$h_{\mathrm{sunrise}} = 12-\frac{\tau}{2}, \tag{5.22}$$

$$h_{\mathrm{sunset}} = 12+\frac{\tau}{2}\cdot \tag{5.23}$$

The time when the maximum elevation angle is achieved depends on the detector's tilt angle φ_t. For example, maximum elevation angle is achieved when $t = h_{\max}$ and is equal to $t = 12$.

As depicted in Figure 36, the elevation angle at sunrise is zero, $\varphi_e(t) = 0$ at $t = 0$. It consistently increases until it reaches to $h_{\max}$ at which the maximum elevation angle is achieved as

$$\varphi_e(h_{\max}) = \varphi_{e_{\max}}. \tag{5.24}$$

After this point, the elevation angle decreases until it reaches zero at sunset. This behavior can be approximated as a triangular function in the form of [100]

$$\varphi_e(t) \approx \begin{cases} \frac{\varphi_{e\max}}{h_{\max}} t, & 0 < t < h_{\max} \\ \varphi_{e_{\max}} - \frac{\varphi_{e\max}}{(h_{\max} - \tau)} (h_{\max} - t), & h_{\max} \leq t < \tau \end{cases}. \tag{5.25}$$

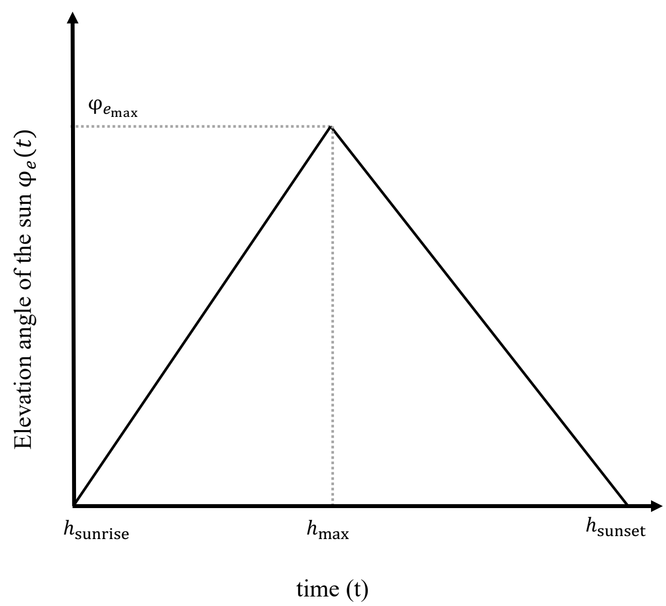

Figure 36: The elevation of the solar panel in time series.

In Equation (5.25), $\varphi_{e_{\max}}$ is the maximum elevation angle of the sun.

$$\varphi_{e_{\max}} = 90^{\circ} + L - \delta. \tag{5.26}$$

It depends on the latitude of the location of interest L and varies with the day of the year, which is given by [100].

5.3.3 Underwater Solar Power based on Different Tilt Angles

In Figure 37, the sun's power is shown as a function of the different types of water (coastal and clear ocean) and the different days of the year associated with the different types of water (January 1st and June 29th) as determined by equation Equation (5.10) on page 70.

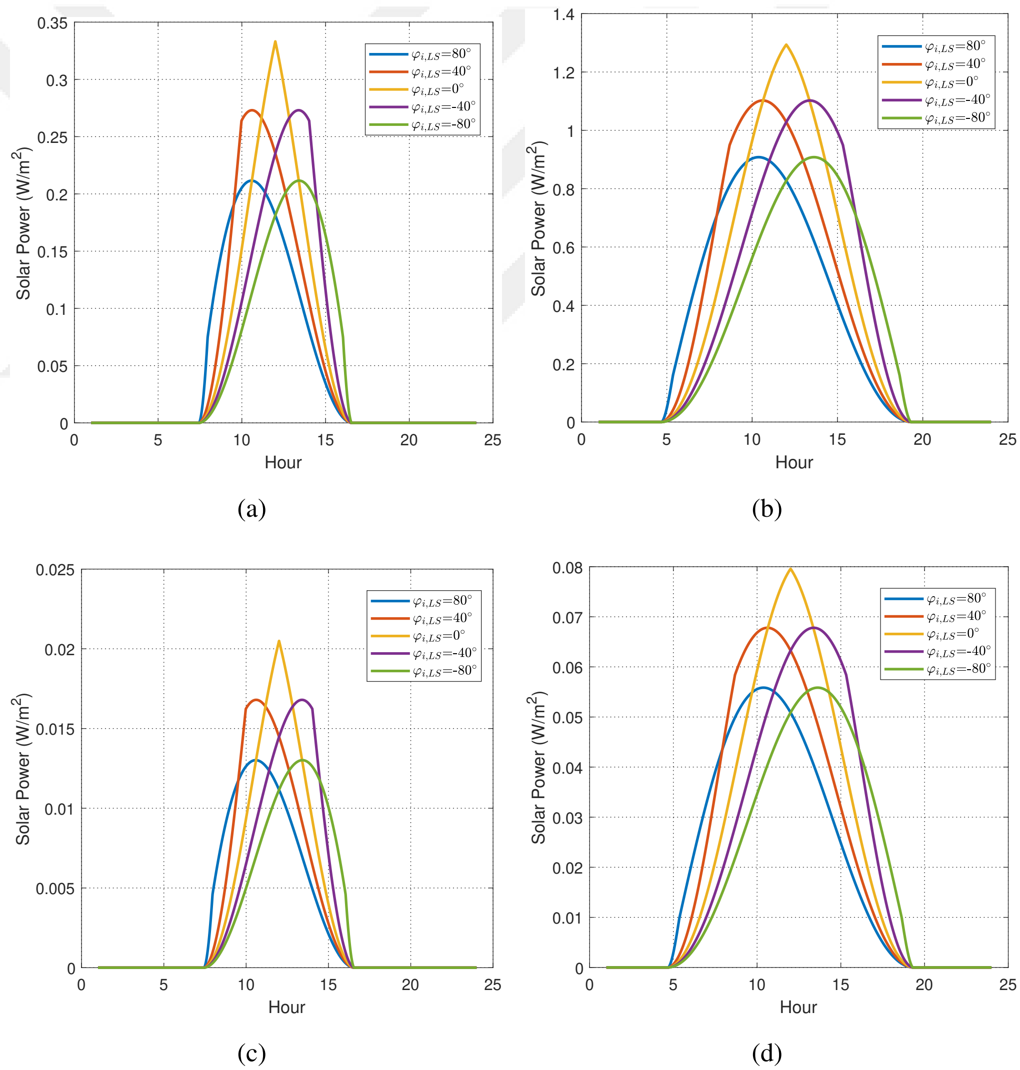

Figure 37: Solar power with respect to $\varphi_{i,\mathrm{LS}}$ (a) January 1st - clear ocean, (b) June 29th - clear ocean, (c) January 1st - coastal water, (d) June 29th - coastal water.

It can be readily demonstrated that sun power changes at maximum for the photodetector's tilt angle φ_t as the angle φ_t changes. In the same way, on June 29$^{\text{th}}$, compared to January 1$^{\text{st}}$, the maximum solar power will be almost four times greater than on June 29$^{\text{th}}$. It is also important to note that coastal water types are characterized by higher extinction coefficients underwater because of their visible light spectrum. As seen in the figure, this prevents the sun's energy from being detected more effectively by the photodetector since it prevents the solar energy from being detected more effectively.

5.4 SNR Calculation

Under the presence of an incident angle of $\varphi_{i,\text{sun}}$, the effective area for noise from the sun can be written as

$$\gamma = \frac{P_R}{\sigma_n^2 + \sigma_S^2}. \tag{5.27}$$

If we replace P_R from Equation (5.4) on page 68, and σ_S^2 from Equation (5.7) on page 69, the γ can be further written by

$$\begin{aligned}\gamma &= \frac{\frac{16 P_T \eta_g A_s^2 \left(1-\cos\left(2\varphi_{i,\text{LS}}\right)\right)}{\pi^2 \theta^4 d_c^4} \exp\left(-2c\left(\lambda\right)\, d_c\right)}{\sigma_n^2 + A_s G_{\text{water}}\, \eta_g \exp\left(-zc\left(\lambda\right)\right)} \\ &= \frac{16 P_T \eta_g A_s^2 \left(1-\cos\left(2\varphi_{i,\text{LS}}\right)\right) \exp\left(-2c\left(\lambda\right)\, d_c\right)}{\sigma_n^2 \pi^2 \theta^4 d_c^4 + \pi^2 \theta^4 d_c^4 A_s G_{\text{water}}\, \eta_g \exp\left(-zc\left(\lambda\right)\right)},\end{aligned} \tag{5.28}$$

where σ_n^2 the Additive White Gaussian Noise (AWGN) and is modeled as $w \sim \mathcal{N}\left(0, \sigma_n^2\right)$.

The AWGN noise can be written as

$$\sigma_n^2 = N_\circ W, \tag{5.29}$$

where W is the system bandwidth ($W = 5\,\text{MHz}$). $N_\circ$ can be further expanded as

$$N_\circ = \sigma_{thermal}^2 + \sigma_{current}^2 + \sigma_{shot}^2. \tag{5.30}$$

In Equation (5.30), we ignore the shot noise (σ_{shot}) and current noise ($\sigma_{current}$) terms and keep the AWGN source is only caused by the thermal noise. Further equality for the thermal noise can be written as

$$\sigma_{thermal} = \sqrt{4kTR}, \tag{5.31}$$

where the k as the Boltzman constant, T is the temperature in Kelvin (T = 300°K), and R is the feedback resistor ($R = 1000\,\Omega$). The link distance is $d_c = 10\,\text{m}$.

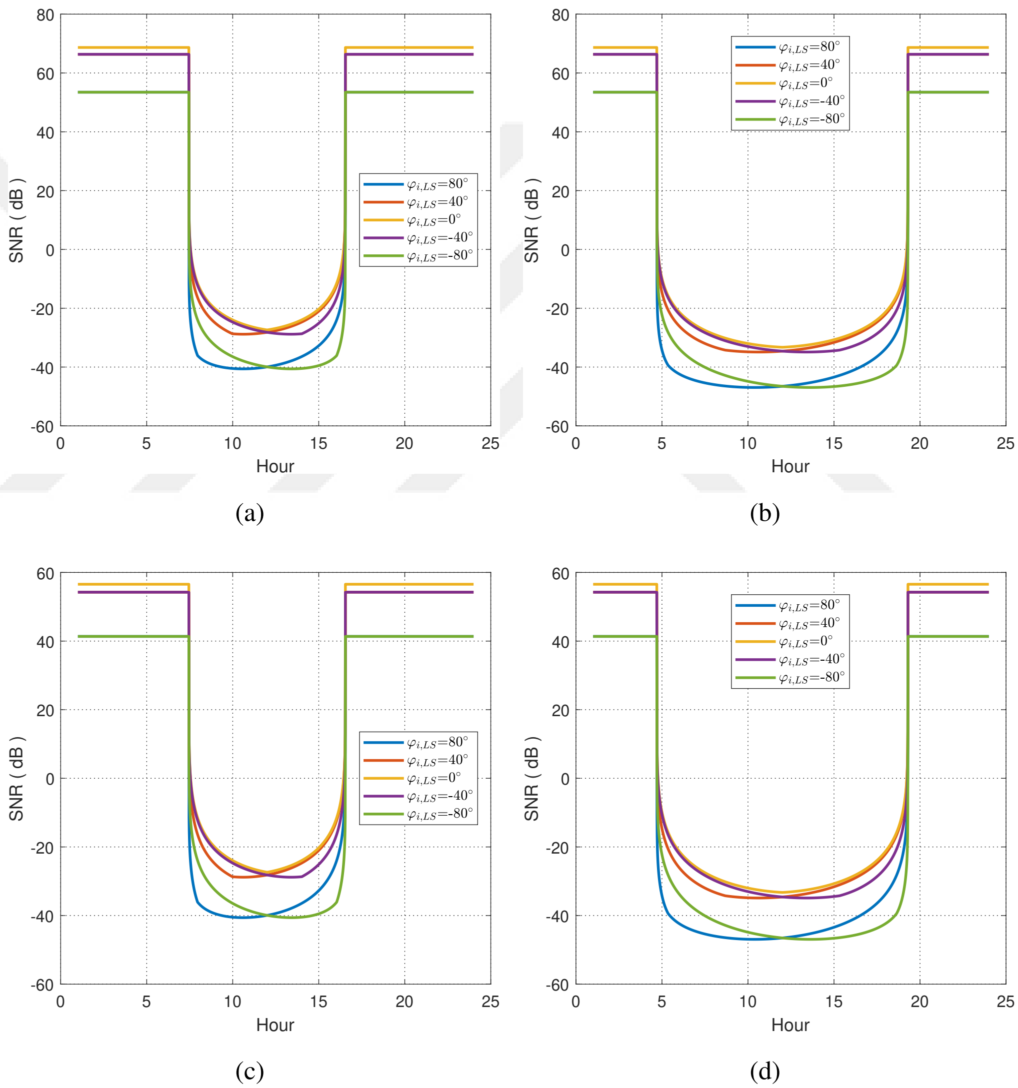

Figure 38: SNR with respect to $\varphi_{i,\text{LS}}$ in Istanbul (a) January 1$^{\text{st}}$ - clear ocean, (b) June 29$^{\text{th}}$ - clear ocean, (c) January 1$^{\text{st}}$ - coastal water, (d) June 29$^{\text{th}}$ - coastal water.

A green color LD is assumed to be used as the optical signal (λ =530 nm). For the water turbidity condition, clear-ocean and coastal water types are utilized. 1 mW of electrical power is transmitted. The A_s is assumed as a 0.5×0.5 m of a photodetector panel. $\theta = 6^\circ$ is the semi-collimated beam divergence angle. The depth is assumed at $z = 20$ m. For the selected system parameters, the SNR values can be represented as given in Figure 38 on the previous page for different panel tilt angles. Tilt angles of more than zero degrees enable the system to provide better SNR within a limited range of angles. Conversely, systems with tilt angle greater than zero degrees can provide better SNR.

5.5 SNR Optimization

Here in this section, we aim to optimize the SNR of the proposed system by changing the tilt angle and then the wavelength depending on the hour of the day concerning latitude and different days of the year.

5.5.1 SNR Optimization by Tilt Angle

Based on the UVLC system proposed in the Figure 33 on page 66 as a vertical UVLC communication link, we can build a system for optimizing the tilt angle based on SNR calculations. In the presence of the sun, we should expect the system to provide lower SNR values. Different tilt angles (φ_t) can shift the solar noise with different peak power values, as shown in Figure 37 on page 74. So, to maximize the SNR of the UVLC communication system given in Equation (5.28) on page 75, one can either increase the nominator (P_R) or decrease the denominator ($\sigma_n^2 + \sigma_S^2$) terms.

Due to the assumption that the AWGN noise is constant, we need only to decrease the noise caused by the sun, which can be found Equation (5.10) on page 70. The system parameters are chosen the same as those given in Section 5.4. Based on the optimization algorithm provided below, we can adjust the panel tilt angle based on the solar noise based on latitude, day of the year, and hour of the day. This approach prioritizes reducing solar noise while maximizing SNR. Based on the given system parameters A_S, λ, d_c, θ, P_T, η_g, z, d, L, we set the time instant in the day equals t and the maximum SNR ($\gamma_{\max} = 0$). Then, we set the interval of as tilt angle is $[\varphi_{t_{\max}}, -\varphi_{t_{\max}}]$. The SNR with respect to φ_t is given as $\gamma(\varphi_t)$. Optimum tilt angle gives the maximum SNR at the time instant t is $\varphi_{t,\text{opt}}$. t_{start} is the start time, t_{end} is the end time, and t_{inc} is the time interval increment as an hour in the day.

Based on this information and the parameters assumed in Section 5.4 on page 75, we have plotted the optimal tilt angles according to selected hours of the day, four different days in the year, at three other locations in the world for Istanbul, Sydney, and Singapore, as shown in Figure 39 on the next page, Figure 40 on page 80, and Figure 41 on page 81. The water type is considered the coastal water, and the relevant extinction coefficient is selected based on Figure 35 on page 69. This search algorithm gives two critical outcomes for tilt angles that can be obtained from Algorithm 1. First, the maximum recorded SNR value is to be recorded. Second, the tilt angle is recorded when the maximum SNR is achieved.

Algorithm 1 UVLC optimization system based on the tilt angle algorithm.

Initialization for initial SNR value: $\gamma_{t_{\max}} = 0$, $\varphi_{t,\text{opt}} = \varphi_{\min}$
for $t = t_{\text{start}}$ to t_{end} **do**
    Calculate SNR by using Equation (5.28) on page 75
    for $\varphi_t = \varphi_{\min}$ to $\varphi_{\max}$ **do**
        if $\gamma(\varphi_t) \geq \gamma_{t_{\max}}$ **then**
            $\gamma_{t_{\max}} = \gamma(\varphi_t)$
            $\varphi_{t,\text{opt}} = \varphi_t$
        end if
    end for
    Record $\varphi_{t,\text{opt}}$ as the optimum tilt angle at time instant t.
end for

A critical component of Algorithm 1 is the maximization of the SNR value. SNR is increased by increasing the signal link strength in the numerator. Therefore, when we change the angle of the receiving panel in a vertically positioned communication link, we reduce the effective area and strength of the received signal. Thus, the tilt angle of 0° is an optimal selection when no other noise source exists. However, the denominator of SNR has both AWGN noise and solar noise components, degrading items for the total SNR. In other words, any increase in the noise components will lessen the SNR. For example, solar noise, a noise component caused by solar energy, will decrease SNR if we consider AWGN constant, while its decrease will increase SNR if we consider AWGN constant. Using the parameters that can be changed in our proposed Algorithm, the optimum SNR value can be calculated by considering both the numerator and denominator parts.

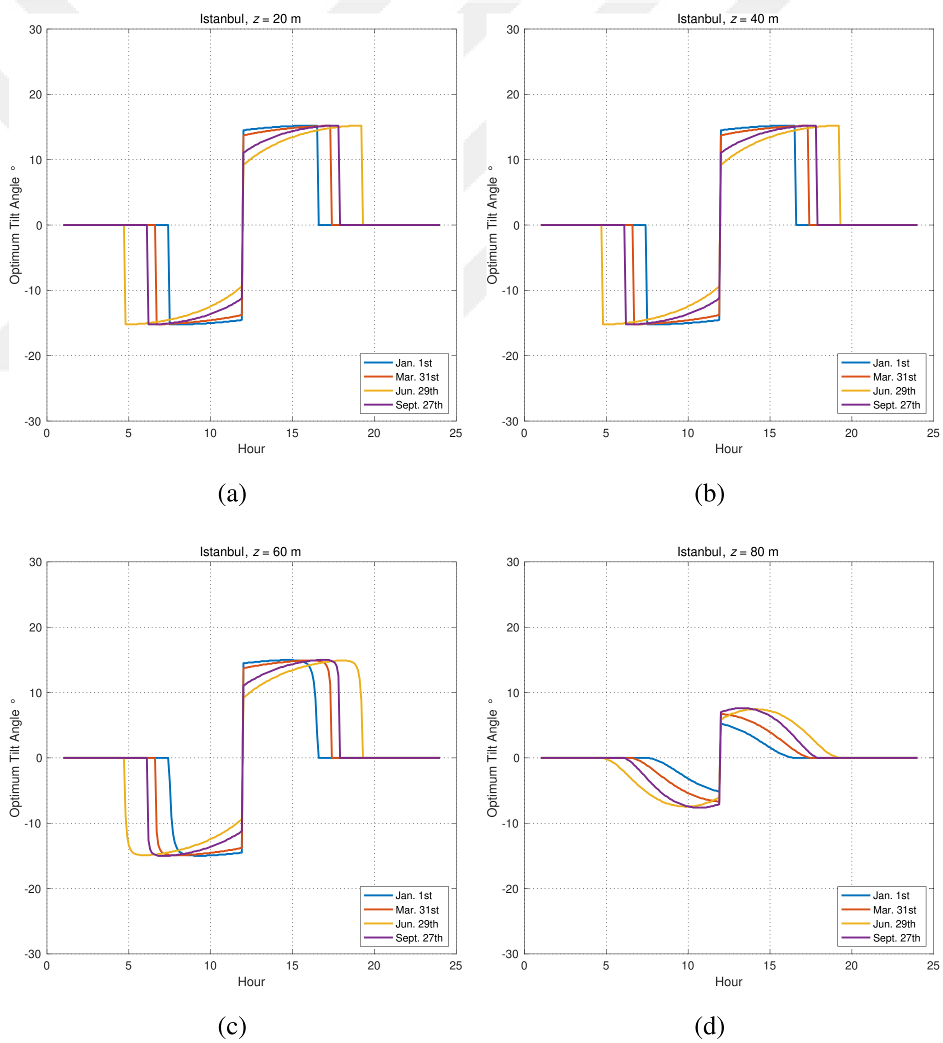

Figure 39: Optimum tilt angles in Istanbul (a) $z = 20\,\text{m}$, (b) $z = 40\,\text{m}$, (c) $z = 60\,\text{m}$, and (d) $z = 80\,\text{m}$.

In the UVLC system we constructed, let us assume the wavelength is a constant and the tilt angle is the only changing system parameter. As per the optimization of the tilt angle, it varies between -15° to 15° depending on the year and the underwater depth. SNR maximization tends to occur earlier during summer, especially for Istanbul (Northern hemisphere) and Sydney (Southern hemisphere). As shown in Figure 39 on the preceding page, the tilt angle behavior at the world's epicenter is almost similar throughout the year. In addition, as the depth increases, solar power becomes obsolete after a certain point.

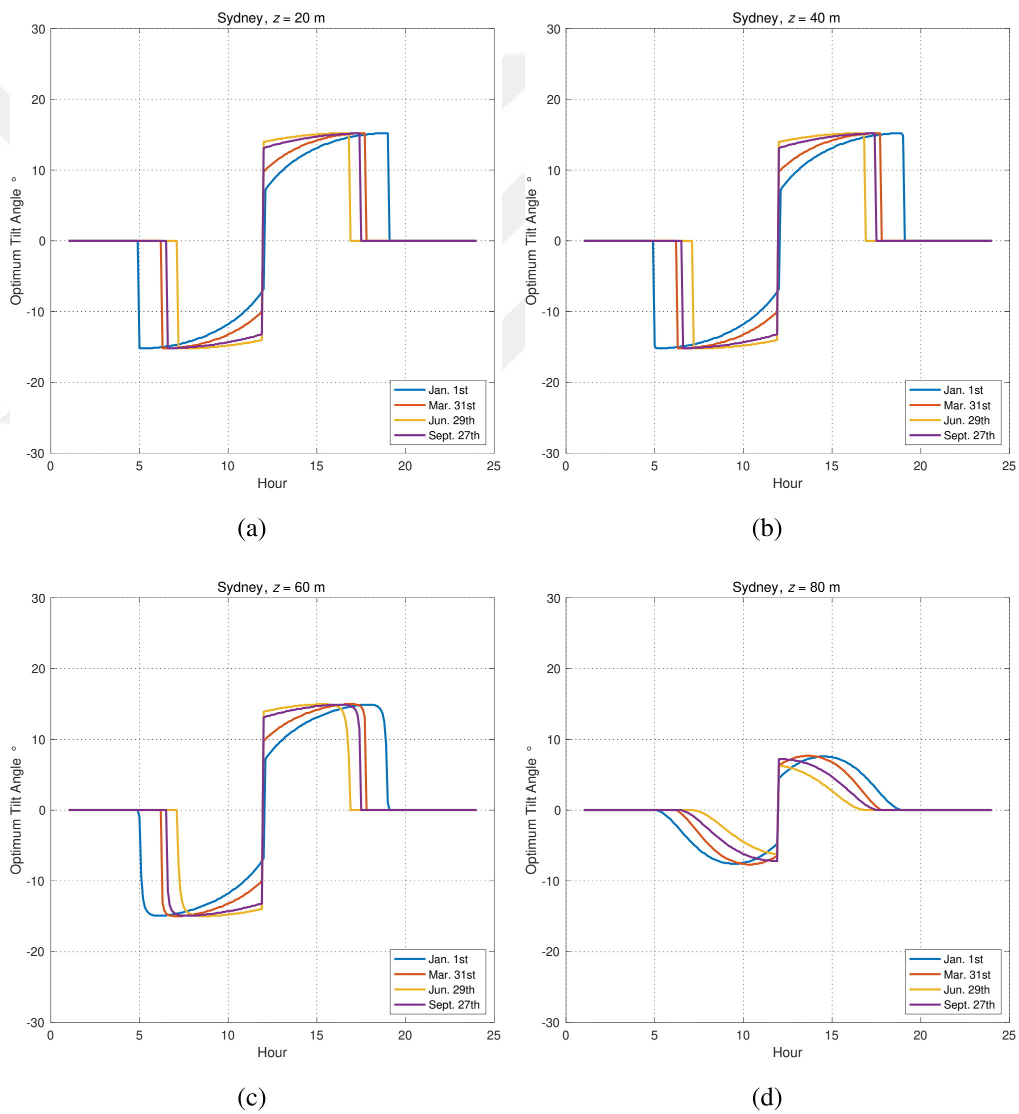

Figure 40: Optimum tilt angles in Sydney (a) $z = 20\,\text{m}$, (b) $z = 40\,\text{m}$, (c) $z = 60\,\text{m}$, and (d) $z = 80\,\text{m}$.

In particular, starting at 60 m, the tilt angle tends to change for SNR optimization. Since solar power does not exist at this depth, the system always provides the maximum SNR at a tilt angle of 0°. Since Istanbul is located in the northern hemisphere, the tilt angle change in January is shorter than in other months. However, as expected, the tilt angle change in June shows the most prolonged period of the day.

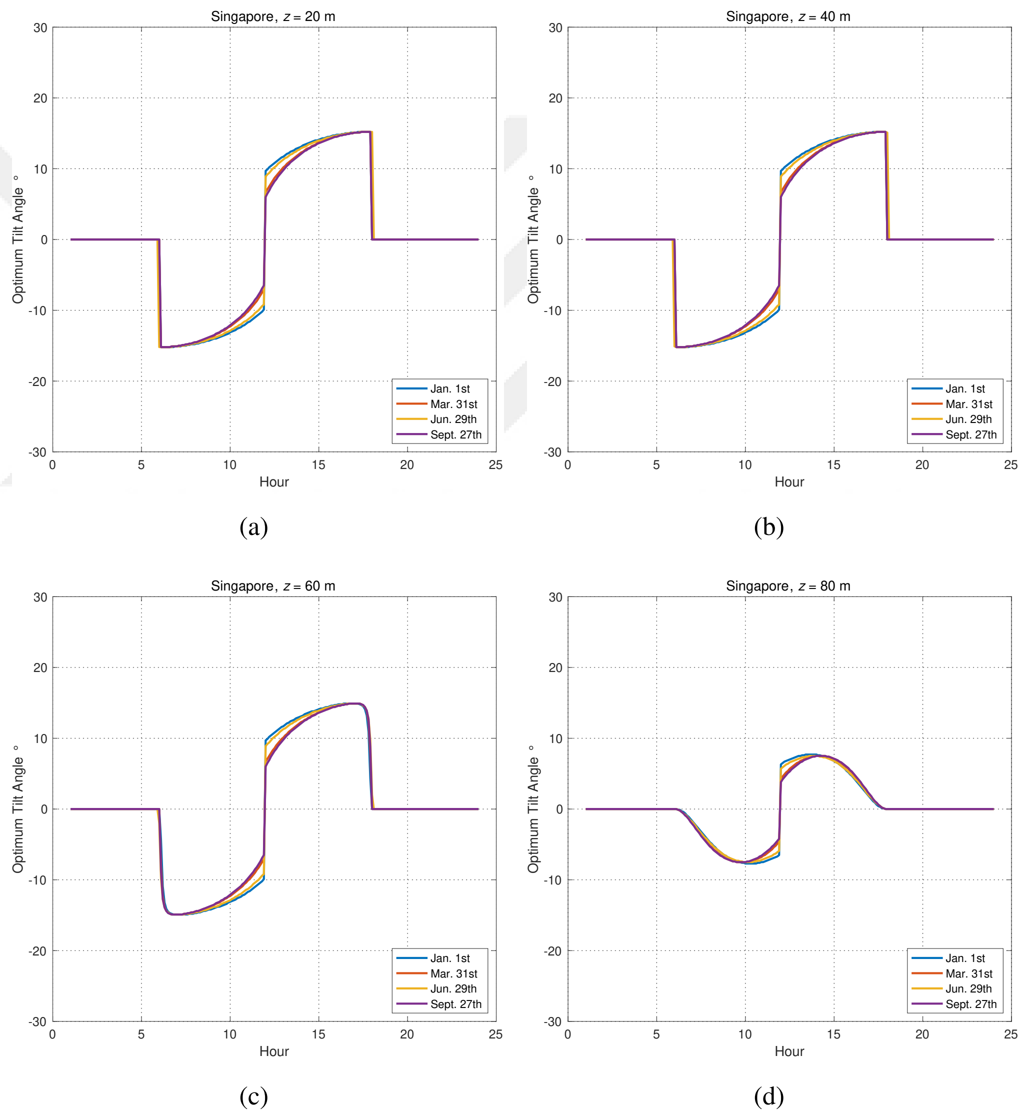

Figure 41: Optimum tilt angles in Singapore (a) $z = 20\,\text{m}$, (b) $z = 40\,\text{m}$, (c) $z = 60\,\text{m}$, and (d) $z = 80\,\text{m}$.

When we move the same UVLC system to Sydney in the southern hemisphere, the solar energy obtained according to the season will be exactly the opposite concerning the latitudes in the northern hemisphere. As seen in Figure 40 on page 80, the optimum tilt angle change interval on January 1st gives the widest time since it is summer in Sydney. However, as it is winter on June 29th, the destructive effect of solar energy on link quality will be minimal. When a depth of 80 m is reached, the destructive effect of solar energy on the received optical signals will become smaller, just as in the case of Istanbul. Therefore, the range of tilt angle changes will not have to be altered too much. While it is sufficient to change the tilt angle in a range of approximately ± 15 degrees at locations less than 80 m depth, this difference decreases to approximately ± 8 degrees when 80 m depth is reached. We observed the behavior of the proposed optimization system in both the northern hemisphere (Istanbul) and the southern hemisphere (Sydney). When we test the same optimization system at a location around the equator, we get the results in Figure 41 on the preceding page for Singapore. The optimum tilt angle varies very little during the year's four seasons. The biggest reason for this is that there is not much difference between day and night around the equator. As the depth increases, the angles of change of the tilt angle decrease for Singapore, similar to Istanbul and Sydney.

5.5.2 SNR Optimization by Wavelength

Based on the UVLC system proposed in the Figure 33 on page 66 as a vertical UVLC communication link with fixed transmitter and optical receiver positions, we can build a system for changing the operating wavelength based on SNR calculations by considering no change in the other system parameters. In the presence of the sun, we should expect the system to provide lower SNR values. Different operating wavelengths (λ_t) can change the extinction coefficient in the water as given in Section 5.2.2 on page 68 so that the different water concentrations will differ depending on the depth. The similar optimization given in Algorithm 1 on page 78, we can provide the SNR optimization Algorithm by changing the wavelength. So, we consider a fixed system with no moving receivers or transmitters.

Algorithm 2 UVLC optimization system based on the wavelength algorithm.

Initialization for initial SNR value: $\gamma_{t_{\max}} = 0$, $\lambda_{t,\text{opt}} = \lambda_{\min}$
for $t = t_{\text{start}}$ to t_{end} **do**
    Calculate SNR by using Equation (5.28) on page 75
    for $\lambda_t = \lambda_{\min}$ to $\lambda_{\max}$ **do**
        if $\gamma(\lambda_t) \geq \gamma_{t_{\max}}$ **then**
            $\gamma_{t_{\max}} = \gamma(\lambda_t)$
            $\lambda_{t,\text{opt}} = \lambda_t$
        end if
    end for
    Record $\lambda_{t,\text{opt}}$ as the optimum wavelength at time instant t.
end for

Instead, we assume the wavelength can be changed or modified with a 1 nm resolution. To build this optimization method, we build an optimization algorithm as given in Algorithm 2. To measure the performance of this Algorithm, we used the system parameters in the SNR calculation section given in Section 5.4. We tested the performance of the proposed Algorithm in three different parts of the world, namely the northern hemisphere (Istanbul in Figure 42), the southern hemisphere (Sydney in Figure 43 on the next page), and the equator (Singapore in Figure 44 on page 85). The Algorithm 1 on page 78 was only tested in coastal waters for four depths.

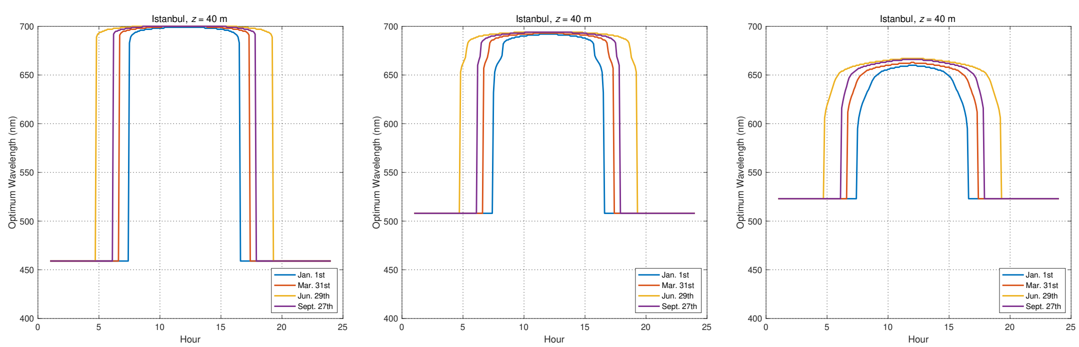

(a) (b) (c)

Figure 42: Optimum wavelengths in Istanbul (a) pure sea, (b) clear ocean, and (c) coastal water type.

Based on the pure sea, clear ocean, and coastal water types for the four different seasons, we evaluated the performance using a 40 m depth and a constant photodetector angle of 0°. As given in Figure 42 on the preceding page, we started by calculating the SNR for Istanbul, located in the northern hemisphere, in the Algorithm we use to maximize SNR. The lower and upper bounds chosen for this algorithm's wavelength are considered as 400 nm and 700 nm, respectively. During this study, the optimum wavelength at which the system will operate was determined as 460 nm for pure water, 505 nm for clear ocean water, and 525 nm for coastal water when there is no solar noise. As a result of increasing the operating wavelength with solar power included in the system, the extinction coefficient in water is expected to increase, resulting in a reduction in the strength of the signal. However, since solar energy reduces photodetector reception due to solar energy penetration, the optimum operating wavelength will converge up to 700 nm when the sun is at its peak. For Istanbul, similar to the tilt optimization algorithm, the effect time of solar energy on the system on June 29th will be longer than the days of the other three seasons. Therefore, the operating wavelength will more quickly converge to the upper wavelength limit of 700 nm to maximize SNR. As given in Figure 43, contrary to the results we obtained in Istanbul, for Sydney, located in the southern hemisphere, the day with the sun's highest is January 1st.

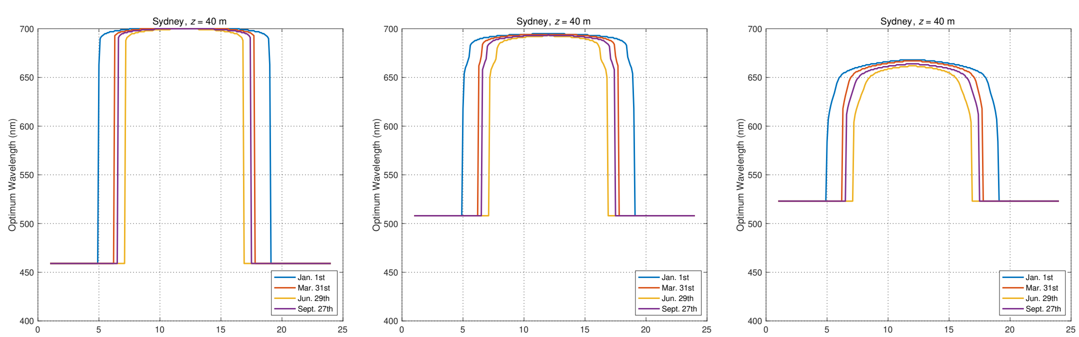

(a) (b) (c)

Figure 43: Optimum wavelengths in Sydney (a) pure sea, (b) clear ocean, and (c) coastal water type.

When there is no solar noise, the optimum wavelength for the system is 460 nm for pure water, 505 nm for clear ocean water, and 525 nm for coastal water. The extinction coefficient in water is expected to increase with increasing operating wavelengths with solar power included in the system, resulting in a reduction in signal strength. Since solar energy reduces photodetector reception when the sun is at its peak, the optimal operating wavelength converges to 700 nm.

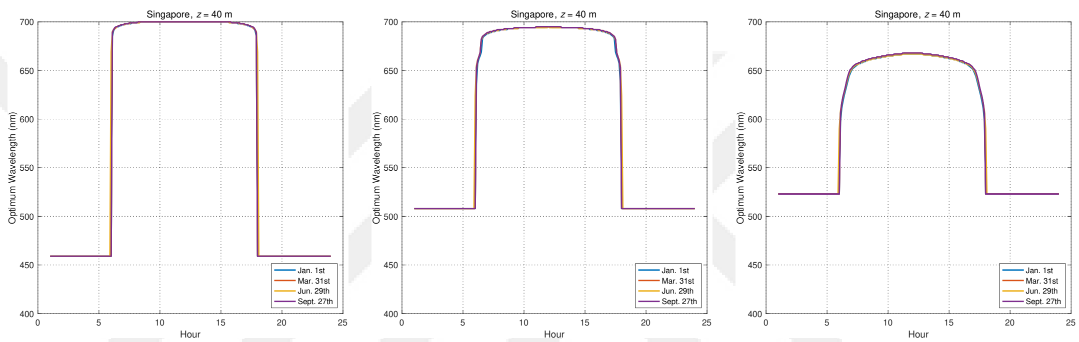

(a) (b) (c)

Figure 44: Optimum wavelengths in Singapore (a) pure sea, (b) clear ocean, and (c) coastal water type.

Finally, we tested the same optimization algorithm for Singapore, located around the equator. According to our results, as shown in Figure 44, the optimum operating wavelength starts to change when solar energy is included in the system. When the sun is at its peak, it converges up to 700 nm. After that, it returns to the old optimum steady-state fixed operating wavelength at night. Unlike the previous performance results given in Istanbul and Sydney, since this system is around the equator, the inclusion of solar energy is approximately the same between the selected days for all four seasons. Therefore, no significant difference is observed between days.

CHAPTER VI

CONCLUSIONS AND FUTURE WORK

This chapter presents a comprehensive review of the dissertation's objectives and results. In addition, it was our objective to highlight the contributions made by this research. Finally, we conclude by suggesting some areas for future work.

6.1 Conclusions

As part of this dissertation, we first developed an experimental testbed that enabled semi-collimated UVLC channel measurements. We proposed closed-form expressions for the system parameters based on the experimentally validated channel model, and then we presented the performance constraints associated with semi-collimated UVLC systems. Next, the reflector-aided UVLC channel model was developed based on a hypothetical photodetector concept for detecting optical signals in NLOS channels. This model was called reflector-aided underwater optical channel modeling, and we demonstrated its contribution theoretically and experimentally. Furthermore, this channel model describes how any number of underwater reflectors can enhance a semi-collimated optical signal through reflection so that even a single reflector can enhance a semi-collimated optical signal propagation under the water. In the last part of this dissertation, we analyzed a real-life deployment of a semi-collimated UVLC system, including the mathematical modeling of solar noise. Based on this model, we derived the SNR from being measured in the overall system. Finally, we proposed an optimization algorithm based on the SNR value to maximize SNR while minimizing solar noise. Below is a summary of the contributions made in this dissertation.

In Chapter 2, we first built the necessary test system for the experimental measurement of semi-collimated UVLC systems. To accurately measure semi-collimated optical signals underwater, we first had to determine the extinction coefficient of water. Therefore, our first study in Chapter 2 was the underwater propagation of a collimated optical signal. First, we used an experimental system to measure the extinction coefficient and verified the path loss of a collimated signal. Following these measurements, we calculated the effective beam divergence angle of the Gaussian semi-collimated optical signal using the optical power value corresponding to the maximum peak value. After that, we constructed the necessary transmitter and receiver circuitry to be placed at separate cuvettes, and we put these cuvettes in an aquarium with $(1\,\mathrm{m} \times 1\,\mathrm{m} \times 8\,\mathrm{m})$ dimensions at Okatem Research Center. After measuring the extinction coefficients of two water types and validating them within the collimated measurements in our test bed, we measured the semi-collimated UVLC signal at specific distances using separate cuvettes and their optical power. Comparing our results to the theoretical model in [20], we achieved good accuracy with the experimental measurements in two different water types.

In Chapter 3, we demonstrated maximum acceptable performance limits of UVLC semi-collimated systems that we have experimentally validated in Chapter 2. We computed the maximum achievable link distance, the maximum acceptable beam divergence angle, the minimum acceptable receiver aperture diameter, and the maximum acceptable water turbidity limit as closed-form expressions in the semi-collimated M-UPAM UVLC system parameters. According to these closed-form expressions, we showed the performance variation of each system parameter in the desired BER and SNR values in the pure sea, clear ocean, and coastal water types.

In Chapter 4, we created a reflector-aided optical channel model to support the underwater propagation of semi-collimated optical signals. For this, we built a model based on the pointing error concept, in which we can receive NLOS signals using the hypothetical photodetector concept. When the LOS Gaussian semi-collimated optical signal was positioned at the center of the photodetector beam, the channel coefficient value was obtained by the model in [20]. When we added one or more reflecting surfaces to this system, we assumed that the reflector surface forms an imaginary hypothetical photodetector relative to the photodetector. Almost as much as the signal itself, the channel coefficient increases as the reflector surface approaches the center of the Gaussian beam. Therefore, we first proposed reflector-aided UVLC channel modeling mathematically. We then used our measurement system to experimentally measure the highest possible channel coefficient gain value, especially at 2 m and beyond. We used a stationary water surface and a mirror submerged in water to measure channel gain. In addition, we presented the experimental aspects we encountered in our practical systems after demonstrating how we obtained the channel model from the theoretical model and the results of the experiments that confirmed the model.

To this end, we conducted all our examinations, assuming the noise source was constant. In Chapter 5, we examined the degrading effect of solar energy as a noise source and the performance of a vertical communication link underwater (submarine to submarine or submarine to a fixed destination). First, we made an SNR calculation considering the semi-collimated UVLC optical signal propagation. Then, we calculated the extinction coefficient approximation of water based on the model introduced [98] according to distinct water concentrations. Then, on a particular day of the year, at any time, we calculated how much solar energy could reach an energy harvesting panel located underwater, according to the desired latitude. According to our model, when a specific tilt angle was applied to the receiver panel, while the solar energy received decreases, different tilt angles will result in different amounts of solar energy reaching the receiver panel. Then, merging all these, we proposed a combined SNR. As a result of this model, high solar energy decreased SNR, as did the change in the angle of the receiver panel. So, the SNR was diminished because the solar noise strengthened the noise component of the primary signal. For this reason, we have revealed how the optimum tilt angle alters on different days of the year in various locations worldwide. We delivered optimization algorithms to maximize the SNR by changing the panel tilt angle and the operating wavelength.

6.2 Future Work

In Chapter 2, we were able to measure up to 5 m in our test bed. Therefore, we could verify in 2 different water types up to 5 m. Furthermore, one can improve the theoretical model by checking whether changing the turbidity of the water by adding a scattering agent to the water in a controlled manner provides similar accuracy. In addition, developing the semi-collimated UVLC channel coefficient model by incorporating the effect of water temperature on the channel coefficient in the channel measurements may be the subject of future topics. Besides experimenting with semi-collimated UVLC systems on a short communication range (i.e., less than 5 m), this study can be further developed to acquire the UVLC channel models with the use of higher power optical signals in a larger aquarium. With these improvements, one can build an end-to-end transceiver system to perform UVLC communication performance for the applications such as single and multi-carrier systems and Multiple-Input Multiple-Output (MIMO) UVLC communication.

In Chapter 3, we examined the system's performance constraints by calculating the system parameters used in the conventional semi-collimated UVLC test system in closed form. A transceiver system can be designed to verify the system limits. Future work can also focus on confirming the accuracy of these closed-form expressions in a targeted BER value and executing this study for multi-carrier systems.

In Chapter 4, we theoretically proposed and experimentally validated the reflector-aided underwater optical channel model. The signal gain we proved experimentally in this study was to show the maximum channel gain. To improve the proposed NLOS UVLC channel model, generalizing the model to include the case in which the transmitter and the receiver were not facing each other shall be a good topic from a theoretical point of view. By controlling the reflecting surface(s) on a motorized system, any direction and alignment between the transmitter and the receiver to be verified experimentally can be the future research direction of this study. To further improve the concept, the mathematical and experimental validation of a parabolic reflector design on NLOS UVLC systems can be provided so that the semi-collimated optical signals can be directed towards the receiver lens.

In Chapter 5, we considered the vertical communication link where the receiving lens looks towards the water surface while receiving the optical signal. This model can be further improved by changing both receiving panel tilt angle and the panel azimuth to achieve the maximum SNR. Additionally, the same principle can be applied to horizontal links where the receiving panel is orthogonal to the sea surface. In the same way, moving underwater objects can be designed using the same concepts that apply to horizontal and vertical underwater objects.

PUBLICATIONS

Some of the research leading to this dissertation has appeared previously in the following publications.

Journal Articles

[1] **Yıldız, Samet**, Bağlıca İ, Kebapçı B, Elamassie M, Uysal M, ”Reflector-aided underwater optical channel modeling,” *Optics Letters*, 47, 5321-5324 (2022).

Conference Papers

[1] **Yıldız, Samet**, Bağlıca, İ., Kebapçı, B., Elamassie, M., and Uysal, M, ”An Experimental Study of Underwater Visible Light Communication,” *in IEEE 2022 30th Signal Processing and Communications Applications Conference (SIU) (pp. 1-4)*, Safranbolu, Turkey, May 2022.

REFERENCES

[1] M. F. Ali, D. N. K. Jayakody, and Y. Li, "Recent trends in underwater visible light communication (UVLC) systems," *IEEE Access*, vol. 10, pp. 22169–22225, 2022.

[2] G. Schirripa Spagnolo, L. Cozzella, and F. Leccese, "Underwater optical wireless communications: Overview," *Sensors*, vol. 20, no. 8, p. 2261, 2020.

[3] D. Menaka, S. Gauni, C. T. Manimegalai, and K. Kalimuthu, "Challenges and vision of wireless optical and acoustic communication in underwater environment," *International Journal of Communication Systems*, vol. 35, no. 12, p. e5227, 2022.

[4] Z. Chen, X. Tang, C. Sun, Z. Li, W. Shi, H. Wang, L. Zhang, and A. Zhang, "Experimental demonstration of over 14 AL underwater wireless optical communication," *IEEE Photonics Technology Letters*, vol. 33, no. 4, pp. 173–176, 2021.

[5] L. J. Johnson, F. Jasman, R. J. Green, and M. S. Leeson, "Recent advances in underwater optical wireless communications," *Underwater Technology*, vol. 32, no. 3, pp. 167–175, 2014.

[6] B. Nababan, D. Ulfah, and J. Panjaitan, "Light propagation, coefficient attenuation, and the depth of one optical depth in different water types," in *IOP Conference Series: Earth and Environmental Science*, vol. 944, p. 012047, IOP Publishing, 2021.

[7] C. Zhang, Z. Wei, X. Li, Y. Li, L. Wang, L. Wang, H. Y. Fu, and Y. Yang, "3.8 Gb/s PAM-4 UOWC system over a 2-m underwater channel enabled by a single-pixel 175-μm GaN-based mini-LED," *IEEE Photonics Journal*, vol. 14, no. 3, pp. 1–7, 2022.

[8] T. Kodama, M. A. B. A. Sanusi, F. Kobori, T. Kimura, Y. Inoue, and M. Jinno, "Comprehensive analysis of time-domain hybrid PAM for data-rate and distance adaptive UWOC system," *IEEE Access*, vol. 9, pp. 57064–57074, 2021.

[9] W.-S. Tsai, H.-H. Lu, H.-W. Wu, S.-C. Tu, Y.-C. Huang, J.-Y. Xie, Q.-P. Huang, and S.-E. Tsai, "500 Gb/s PAM4 FSO-UWOC convergent system with a R/G/B five-wavelength polarization-multiplexing scheme," *IEEE Access*, vol. 8, pp. 16913–16921, 2020.

[10] R. Boluda-Ruiz, P. Rico-Pinazo, B. Castillo-Vázquez, A. García-Zambrana, and K. Qaraqe, "Impulse response modeling of underwater optical scattering channels for wireless communication," *IEEE Photonics Journal*, vol. 12, no. 4, pp. 1–14, 2020.

[11] L. Bariah, M. Elamassie, S. Muhaidat, P. C. Sofotasios, and M. Uysal, "Non-orthogonal multiple access-based underwater VLC systems in the presence of turbulence," *IEEE Photonics Journal*, vol. 14, no. 1, pp. 1–7, 2021.

[12] P. Pandey, G. Matta, and M. Agrawal, “Effect of transmitter divergence-angle on the performance of underwater visible light communication system,” *Optical and Quantum Electronics*, vol. 54, no. 12, pp. 1–14, 2022.

[13] H. Abdavinejad, E. Mostafapour, C. Ghobadi, J. Nourinia, and A. Lotfzad Pak, “Vlc turbulence effects on the performance of the fish school behavior modeling mobile diffusion adaptive networks in underwater environments,” *Wireless Personal Communications*, vol. 124, no. 2, pp. 1661–1676, 2022.

[14] F. Miramirkhani, M. Karbalayghareh, and M. Uysal, “Effect of scattering phase function on underwater visible light communication channel models,” *Physical Communication*, vol. 48, p. 101410, 2021.

[15] H. Abdavinejad, H. Baghali, J. Ostadieh, E. Mostafapour, C. Ghobadi, and J. Nourinia, “Complete performance analysis of underwater VLC diffusion adaptive networks,” *arXiv preprint arXiv:2206.02554*, 2022.

[16] C. Kandouci, “Performances enhancement of underwater wireless optical communications (UWOC) using pulse position modulation,” *Journal of Optical Communications*, vol. 43, no. 2, pp. 289–294, 2022.

[17] D. Chen, Y. Wang, J. Jin, H. Lu, and J. Wang, “An experimental study of noma in underwater visible light communication system,” *Optics Communications*, vol. 475, p. 126199, 2020.

[18] D. Kong, Y. Zhou, J. Chai, S. Chen, L. Chen, L. Li, T. Lin, W. Wang, and G. Li, “Recent progress in InGaN-based photodetectors for visible light communication,” *Journal of Materials Chemistry C*, 2022.

[19] T. Lin, C. Fu, T. Wei, N. Huang, X. Liu, L. Tang, L. Su, J. Luo, and C. Gong, “Waving effect characterization for water-to-air optical wireless communication,” *Journal of Lightwave Technology*, 2022.

[20] M. Elamassie, F. Miramirkhani, and M. Uysal, “Channel modeling and performance characterization of underwater visible light communications,” in *IEEE International Conference on Communications Workshops (ICC Workshops)*, pp. 1–5, IEEE, 2018.

[21] M. Mahmoud, A. I. Boghdady, A. E.-R. A. El-Fikky, and M. H. Aly, “Statistical studies using goodness-of-fit techniques with dynamic underwater visible light communication channel modeling,” *IEEE Access*, vol. 9, pp. 57716–57725, 2021.

[22] M. Elamassie and M. Uysal, “Vertical underwater visible light communication links: Channel modeling and performance analysis,” *IEEE Transactions on Wireless Communications*, vol. 19, no. 10, pp. 6948–6959, 2020.

[23] S. Yahia, Y. Meraihi, A. Ramdane-Cherif, A. B. Gabis, D. Acheli, and H. Guan, “A survey of channel modeling techniques for visible light communications,” *Journal of Network and Computer Applications*, vol. 194, p. 103206, 2021.

[24] M. Elamassie, S. M. Sait, and M. Uysal, “Effect of sea waves on vertical underwater visible light communication links,” *IEEE Journal of Oceanic Engineering*, pp. 1–11, 2022.

[25] B. Li, J. Huang, S. Zhou, K. Ball, M. Stojanovic, L. Freitag, and P. Willett, “MIMO-OFDM for high-rate underwater acoustic communications,” *IEEE Journal of Oceanic Engineering*, vol. 34, no. 4, pp. 634–644, 2009.

[26] A. ElMoslimany, M. Zhou, T. M. Duman, and A. Papandreou-Suppappola, “An underwater acoustic communication scheme exploiting biological sounds,” *Wireless Communications and Mobile Computing*, vol. 16, no. 15, pp. 2194–2211, 2016.

[27] G. Qiao, Z. Babar, L. Ma, S. Liu, and J. Wu, “MIMO-OFDM underwater acoustic communication systems—a review,” *Physical Communication*, vol. 23, pp. 56–64, 2017.

[28] M. Stojanovic and J. Preisig, “Underwater acoustic communication channels: Propagation models and statistical characterization,” *IEEE Communications Magazine*, vol. 47, no. 1, pp. 84–89, 2009.

[29] M. Chitre, S. Shahabudeen, L. Freitag, and M. Stojanovic, “Recent advances in underwater acoustic communications & networking,” *OCEANS 2008*, pp. 1–10, 2008.

[30] R. Santos, J. Orozco, M. Micheletto, S. F. Ochoa, R. Meseguer, P. Millan, and C. Molina, “Real-time communication support for underwater acoustic sensor networks,” *Sensors*, vol. 17, no. 7, p. 1629, 2017.

[31] M. Doniec, A. Xu, and D. Rus, “Robust real-time underwater digital video streaming using optical communication,” in *IEEE International Conference on Robotics and Automation*, pp. 5117–5124, IEEE, 2013.

[32] A. Al-Halafi, H. M. Oubei, B. S. Ooi, and B. Shihada, “Real-time video transmission over different underwater wireless optical channels using a directly modulated 520 nm laser diode,” *Journal of Optical Communications and Networking*, vol. 9, no. 10, pp. 826–832, 2017.

[33] J. Ribas, D. Sura, and M. Stojanovic, *Underwater wireless video transmission for supervisory control and inspection using acoustic OFDM*. IEEE, 2010.

[34] X. Che, I. Wells, G. Dickers, P. Kear, and X. Gong, “Re-evaluation of RF electromagnetic communication in underwater sensor networks,” *IEEE Communications Magazine*, vol. 48, no. 12, pp. 143–151, 2010.

[35] S. Al-Zhrani, N. M. Bedaiwi, I. F. El-Ramli, A. Z. Barasheed, A. Abduldaiem, Y. Al-Hadeethi, and A. Umar, “Underwater optical communications: a brief overview and recent developments,” *Engineered Science*, vol. 16, pp. 146–186, 2021.

[36] H. Kaushal and G. Kaddoum, “Underwater optical wireless communication,” *IEEE Access*, vol. 4, pp. 1518–1547, 2016.

[37] M. Stojanovic, L. Freitag, and M. Johnson, "Channel-estimation-based adaptive equalization of underwater acoustic signals," in *Oceans MTS/IEEE. Riding the Crest into the 21st Century. Conference and Exhibition. Conference Proceedings (IEEE Cat. No. 99CH37008)*, vol. 2, pp. 985–990, IEEE, 1999.

[38] A. Vlasenko, P. Korn, J. Riehme, and U. Naumann, "Estimation of data assimilation error: A shallow-water model study," *Monthly Weather Review*, vol. 142, no. 7, pp. 2502–2520, 2014.

[39] Y. R. Zheng, "Channel estimation and phase-correction for robust underwater acoustic communications," in *MILCOM IEEE Military Communications Conference*, pp. 1–6, IEEE, 2007.

[40] M. Stojanovic, "OFDM for underwater acoustic communications: Adaptive synchronization and sparse channel estimation," in *IEEE International Conference on Acoustics, Speech and Signal Processing*, pp. 5288–5291, IEEE, 2008.

[41] B. Li, S. Zhou, M. Stojanovic, L. Freitag, and P. Willett, "Multicarrier communication over underwater acoustic channels with nonuniform doppler shifts," *IEEE Journal of Oceanic Engineering*, vol. 33, no. 2, pp. 198–209, 2008.

[42] Y. V. Zakharov and V. Kodanev, "Multipath-doppler diversity of OFDM signals in an underwater acoustic channel," in *IEEE International Conference on Acoustics, Speech, and Signal Processing. Proceedings (Cat. No. 00CH37100)*, vol. 5, pp. 2941–2944, IEEE, 2000.

[43] F. Frassati, C. Lafon, P.-A. Laurent, and J.-M. Passerieux, "Experimental assessment of OFDM and DSSS modulations for use in littoral waters underwater acoustic communications," in *Europe Oceans 2005*, vol. 2, pp. 826–831, IEEE, 2005.

[44] F. Lu, S. Lee, J. Mounzer, and C. Schurgers, "Low-cost medium-range optical underwater modem: Short paper," in *Proceedings of the Fourth ACM International Workshop on UnderWater Networks*, pp. 1–4, 2009.

[45] B. Tu, L. Liu, Y. Liu, Y. Jin, and J. Tang, "Acquisition probability analysis of ultra-wide fov acquisition scheme in optical links under impact of atmospheric turbulence," *Applied Optics*, vol. 52, no. 14, pp. 3147–3155, 2013.

[46] X. Yi, Z. Li, and Z. Liu, "Underwater optical communication performance for laser beam propagation through weak oceanic turbulence," *Applied Optics*, vol. 54, no. 6, pp. 1273–1278, 2015.

[47] M. Chen, P. Zou, L. Zhang, and N. Chi, "Demonstration of a 2.34 Gbit/s real-time single silicon-substrate blue led-based underwater VLC system," *IEEE Photonics Journal*, vol. 12, no. 1, pp. 1–11, 2019.

[48] J. Du, Y. Wang, C. Fei, R. Chen, G. Zhang, X. Hong, and S. He, "Experimental demonstration of 50-m/5-Gbps underwater optical wireless communication with

low-complexity chaotic encryption," *Optics Express*, vol. 29, no. 2, pp. 783–796, 2021.

[49] Y. Zhou *et al.*, "Common-anode LED on a si substrate for beyond 15 Gbit/s underwater visible light communication," *Photonics Research*, vol. 7, no. 9, pp. 1019–1029, 2019.

[50] C. Lu, J. Wang, S. Li, and Z. Xu, "60m/2.5 Gbps underwater optical wireless communication with NRZ-OOK modulation and digital nonlinear equalization," in *Conference on Lasers and Electro-Optics (CLEO)*, pp. 1–2, IEEE, 2019.

[51] W. Niu, H. Chen, J. Zhang, Y. Ha, P. Zou, and N. Chi, "Nonlinearity mitigation based on modulus pruned look-up table for multi-bit delta-sigma 32-CAP modulation in underwater visible light communication system," *IEEE Photonics Journal*, vol. 13, no. 1, pp. 1–12, 2021.

[52] J. Du, X. Hong, Y. Wang, Z. Xu, W. Zhao, N. Lv, C. Fei, and S. He, "A comprehensive performance comparison of DFT-S DMT and QAM-DMT in UOWC system in different water environments," *IEEE Photonics Journal*, vol. 13, no. 1, pp. 1–11, 2021.

[53] X. Tang, C. Sun, Z. Chen, and A. Zhang, "Experimental demonstration of a 200Mbps DPSK UWOC system," in *IEEE Photonics Conference (IPC)*, pp. 1–2, 2020.

[54] Z. Wang, J. Chen, and N. Chi, "A novel algorithm for improving the spectrum efficiency of non-orthogonal multiband CAP UVLC systems," *Journal of Lightwave Technology*, vol. 38, no. 22, pp. 6187–6201, 2020.

[55] J. Jia and N. Chi, "Laplacian of gaussian regularizing post-equalization for underwater visual light communication," in *Asia Communications and Photonics Conference (ACP)*, pp. 1–3, 2019.

[56] Z. Zhou, H. Yin, and Y. Yao, "Wireless optical communication performance simulation and full-duplex communication experimental system with different seawater environment," in *IEEE International Conference on Signal Processing, Communications and Computing (ICSPCC)*, pp. 1–4, 2019.

[57] Y. Ha, W. Niu, and N. Chi, "Post equalization scheme based on deep neural network for a probabilistic shaping 128 QAM DFT-S OFDM signal in underwater visible light communication system," in *18th International Conference on Optical Communications and Networks (ICOCN)*, pp. 1–3, 2019.

[58] S. C. Tokgoz, R. Boluda-Ruiz, S. Yarkan, and K. A. Qaraqe, "ACO-OFDM transmission over underwater pipeline for VLC-based systems," in *IEEE 30th Annual International Symposium on Personal, Indoor and Mobile Radio Communications (PIMRC)*, pp. 1–7, 2019.

[59] M. Shi, Y. Zhao, W. Yu, Y. Chen, and N. Chi, "Enhanced performance of PAM7 MISO underwater VLC system utilizing machine learning algorithm based on DBSCAN," *IEEE Photonics Journal*, vol. 11, no. 4, pp. 1–13, 2019.

[60] T. Liu, H. Zhang, Y. Zhang, and J. Song, "Experimental demonstration of LED based underwater wireless optical communication," in *4th International Conference on Information Science and Control Engineering (ICISCE)*, pp. 1501–1504, 2017.

[61] P. Wang, C. Li, B. Wang, and Z. Xu, "Real-time 25Mb/s data transmission for underwater optical wireless communication using a commercial blue LED and APD detection," in *Asia Communications and Photonics Conference (ACP)*, pp. 1–3, 2016.

[62] H. M. Oubei *et al.*, "4.8 Gbit/s 16-QAM-OFDM transmission based on compact 450-nm laser for underwater wireless optical communication," *Opt. Express*, vol. 23, pp. 23302–23309, Sep 2015.

[63] T.-C. Wu, Y.-C. Chi, H.-Y. Wang, C.-T. Tsai, and G.-R. Lin, "Blue laser diode enables underwater communication at 12.4 Gbps," *Scientific Reports*, vol. 7, no. 1, pp. 1–10, 2017.

[64] C.-Y. Li, H.-H. Lu, W.-S. Tsai, M.-T. Cheng, C.-M. Ho, Y.-C. Wang, Z.-Y. Yang, and D.-Y. Chen, "16 Gb/s PAM4 UWOC system based on 488-nm LD with light injection and optoelectronic feedback techniques," *Optics Express*, vol. 25, no. 10, pp. 11598–11605, 2017.

[65] C. Fei, X. Hong, G. Zhang, J. Du, Y. Gong, J. Evans, and S. He, "16.6 Gbps data rate for underwater wireless optical transmission with single laser diode achieved with discrete multi-tone and post nonlinear equalization," *Optics Express*, vol. 26, no. 26, pp. 34060–34069, 2018.

[66] C.-Y. Li, H.-H. Lu, W.-S. Tsai, Z.-H. Wang, C.-W. Hung, C.-W. Su, and Y.-F. Lu, "A 5 m/25 Gbps underwater wireless optical communication system," *IEEE Photonics Journal*, vol. 10, no. 3, pp. 1–9, 2018.

[67] C. Shen, Y. Guo, H. M. Oubei, T. K. Ng, G. Liu, K.-H. Park, K.-T. Ho, M.-S. Alouini, and B. S. Ooi, "20-meter underwater wireless optical communication link with 1.5 Gbps data rate," *Optics Express*, vol. 24, no. 22, pp. 25502–25509, 2016.

[68] H. Chen, X. Chen, J. Lu, X. Liu, J. Shi, L. Zheng, R. Liu, X. Zhou, and P. Tian, "Toward long-distance underwater wireless optical communication based on a high-sensitivity single photon avalanche diode," *IEEE Photonics Journal*, vol. 12, no. 3, pp. 1–10, 2020.

[69] X.-H. Huang, C.-Y. Li, H.-H. Lu, C.-W. Su, Y.-R. Wu, Z.-H. Wang, and Y.-N. Chen, "6-m/10-Gbps underwater wireless red-light laser transmission system," *Optical Engineering*, vol. 57, no. 6, p. 066110, 2018.

[70] F. Wang, Y. Liu, M. Shi, H. Chen, and N. Chi, “3.075 Gb/s underwater visible light communication utilizing hardware pre-equalizer with multiple feature points,” *Optical Engineering*, vol. 58, no. 5, p. 056117, 2019.

[71] H. M. Oubei *et al.*, “Simple statistical channel model for weak temperature-induced turbulence in underwater wireless optical communication systems,” *Optics Letters*, vol. 42, no. 13, pp. 2455–2458, 2017.

[72] Z. Vali, A. Gholami, Z. Ghassemlooy, M. Omoomi, and D. G. Michelson, “Experimental study of the turbulence effect on underwater optical wireless communications,” *Applied Optics*, vol. 57, no. 28, pp. 8314–8319, 2018.

[73] Y. Weng, Y. Guo, O. Alkhazragi, T. K. Ng, J.-H. Guo, and B. S. Ooi, “Impact of turbulent-flow-induced scintillation on deep-ocean wireless optical communication,” *Journal of Lightwave Technology*, vol. 37, no. 19, pp. 5083–5090, 2019.

[74] M. Sait, X. Sun, O. Alkhazragi, N. Alfaraj, M. Kong, T. K. Ng, and B. S. Ooi, “The effect of turbulence on NLOS underwater wireless optical communication channels,” *Chinese Optics Letters*, vol. 17, no. 10, p. 100013, 2019.

[75] H. M. Oubei, C. Shen, K.-H. Park, A. Kammoun, T. K. Ng, M.-S. Alouini, and B. S. Ooi, “Underwater wireless optical communications: from system-level demonstrations to channel modelling,” in *22nd Microoptics Conference (MOC)*, pp. 34–35, IEEE, 2017.

[76] E. Zedini, H. M. Oubei, A. Kammoun, M. Hamdi, B. S. Ooi, and M.-S. Alouini, “A new simple model for underwater wireless optical channels in the presence of air bubbles,” in *GLOBECOM IEEE Global Communications Conference*, pp. 1–6, IEEE, 2017.

[77] M. V. Jamali *et al.*, “Statistical studies of fading in underwater wireless optical channels in the presence of air bubble, temperature, and salinity random variations,” *IEEE Transactions on Communications*, vol. 66, no. 10, pp. 4706–4723, 2018.

[78] E. Zedini, H. M. Oubei, A. Kammoun, M. Hamdi, B. S. Ooi, and M.-S. Alouini, “Unified statistical channel model for turbulence-induced fading in underwater wireless optical communication systems,” *IEEE Transactions on Communications*, vol. 67, no. 4, pp. 2893–2907, 2019.

[79] X. Wang, M. Zhang, H. Zhou, and X. Ren, “Performance analysis and design considerations of the shallow underwater optical wireless communication system with solar noises utilizing a photon tracing-based simulation platform,” *Electronics*, vol. 10, no. 5, p. 632, 2021.

[80] I. C. Ijeh, M. A. Khalighi, M. Elamassie, S. Hranilovic, and M. Uysal, “Outage probability analysis of a vertical underwater wireless optical link subject to oceanic turbulence and pointing errors,” *Journal of Optical Communications and Networking*, vol. 14, no. 6, pp. 439–453, 2022.

[81] W. Wei, C. Zhang, W. Zhang, W. Jiang, C. Shu, and Q. Xiaorui, "Led-based underwater wireless optical communication for small mobile platforms: experimental channel study in highly-turbid lake water," *IEEE Access*, vol. 8, pp. 169304–169313, 2020.

[82] C. T. Geldard, J. Thompson, and W. O. Popoola, "Empirical study of the underwater turbulence effect on non-coherent light," *IEEE Photonics Technology Letters*, vol. 32, no. 20, pp. 1307–1310, 2020.

[83] V. Guerra, J. Rufo, J. Rabadan, and R. Perez-Jimenez, "Effect of moving microalgae on underwater wireless optical links," *Applied Optics*, vol. 59, no. 2, pp. 515–520, 2020.

[84] Y. Yang, F. He, Q. Guo, M. Wang, J. Zhang, and Z. Duan, "Analysis of underwater wireless optical communication system performance," *Applied Optics*, vol. 58, no. 36, pp. 9808–9814, 2019.

[85] S. A. Self, "Focusing of spherical gaussian beams," *Applied Optics*, vol. 22, no. 5, pp. 658–661, 1983.

[86] Thorlabs Inc., "Lb1309-b - n-bk7 bi-convex lens." https://www.thorlabs.com/thorproduct.cfm?partnumber=LB1309-B. [Accessed: December 29, 2022].

[87] W. Cox and J. Muth, "Simulating channel losses in an underwater optical communication system," *J. Opt. Soc. Am. A*, vol. 31, pp. 920–934, May 2014.

[88] C. Gabriel, M.-A. Khalighi, S. Bourennane, P. Leon, and V. Rigaud, "Channel modeling for underwater optical communication," in *IEEE GLOBECOM Workshops (GC Wkshps)*, pp. 833–837, IEEE, 2011.

[89] Z. Wang, Q. Wang, W. Huang, and Z. Xu, *Visible light communications: modulation and signal processing*. John Wiley & Sons, 2017.

[90] W. Baylis, *Theoretical methods in the physical sciences*. Springer, 1994.

[91] J. J. Shynk, *Mathematical foundations for linear circuits and systems in engineering*. John Wiley & Sons, 2016.

[92] F. Miramirkhani and M. Uysal, "Visible light communication channel modeling for underwater environments with blocking and shadowing," *IEEE Access*, vol. 6, pp. 1082–1090, 2017.

[93] X. Sun *et al.*, "375-nm ultraviolet-laser based non-line-of-sight underwater optical communication," *Optics Express*, vol. 26, no. 10, pp. 12870–12877, 2018.

[94] X. Sun, M. Kong, O. Alkhazragi, C. Shen, E.-N. Ooi, X. Zhang, U. Buttner, T. K. Ng, and B. S. Ooi, "Non-line-of-sight methodology for high-speed wireless optical communication in highly turbid water," *Optics Communications*, vol. 461, p. 125264, 2020.

[95] S. Tang, Y. Dong, and X. Zhang, "On path loss of NLOS underwater wireless optical communication links," in *MTS/IEEE OCEANS-Bergen*, pp. 1–3, IEEE, 2013.

[96] A. E.-R. A. El-Fikky, M. E. Eldin, H. A. Fayed, A. Abd El Aziz, H. M. Shalaby, and M. H. Aly, "NLoS underwater VLC system performance: static and dynamic channel modeling," *Applied Optics*, vol. 58, no. 30, pp. 8272–8281, 2019.

[97] C. Dym, *Principles of Mathematical Modeling*. Elsevier Science Limited, 2004.

[98] C. Mobley, "Light and water: radiative transfer," *Natural Waters. Academic Press, San Diego*, 1994.

[99] G. G. Hahn, L. A. Adoram-Kershner, H. P. Cantin, and M. W. Shafer, "Assessing solar power for globally migrating marine and submarine systems," *IEEE Journal of Oceanic Engineering*, vol. 44, no. 3, pp. 693–706, 2018.

[100] S. C. Arum, D. Grace, P. D. Mitchell, M. D. Zakaria, and N. Morozs, "Energy management of solar-powered aircraft-based high altitude platform for wireless communications," *Electronics*, vol. 9, no. 1, p. 179, 2020.

VITA

Samet Yıldız is an Electrical and Electronics Engineer currently working as the RF Systems Engineering team leader at Airties Wireless Networks. He received a B.Sc. in Electrical and Electronics Engineering from Yeditepe University (January 2012, Istanbul - Turkey) and M.Sc in Electrical Engineering from California State University, Long Beach (May 2015, California - USA). In 2015, he started to work in Airties Wireless Networks as his full-time position while starting part-time doctorate studies under the supervision of Prof. Murat Uysal at Özyeğin University, Istanbul, Turkey. His current research interests include RF and Wireless Communication Systems, Wi-Fi Systems, and experimental communication system design in optical and RF fields.